Vimentin Intermediate Filament Softening

—

Recovery Behavior and Post-Translational Modifications

Dissertation

for the award of the degree

"Doctor rerum naturalium"

of the Georg-August-Universität Göttingen

within the doctoral program

Göttingen Graduate School of Neuroscience, Biophysics and Molecular Bioscience (GGNB)

of the Georg-August-University School of Science (GAUSS)

submitted by

Julia Kraxner

from Fürth

Göttingen, 2021

Thesis Committee

Prof. Dr. Sarah Köster
>Institute for X-Ray Physics
>Georg-August-Universität, Göttingen

Prof. Dr. Andreas Janshoff
>Institute of Physical Chemistry
>Georg-August-Universität, Göttingen

Prof. Dr. Blanche Schwappach
>Department of Molecular Biology
>University Medical Center, Göttingen

Members of the Examination Board

Referee: **Prof. Dr. Sarah Köster**
 Institute for X-Ray Physics
 Georg-August-Universität, Göttingen

2$^{\text{nd}}$ Referee: **Prof. Dr. Andreas Janshoff**
 Institute of Physical Chemistry
 Georg-August-Universität, Göttingen

Further members of the Examination Board

Prof. Dr. Blanche Schwappach
 Department of Molecular Biology
 University Medical Center, Göttingen

Prof. Dr. Henning Urlaub
 Bioanalytical Mass Spectrometry
 Max Planck Institute for Biophysical Chemistry, Göttingen

Prof. Dr. Timo Betz
 Third Institute of Physics - Biophysics
 Georg-August-Universität, Göttingen

Prof. Dr. Ralf Ficner
 Institute for Microbiology and Genetics
 Georg-August-Universität, Göttingen

Date of Oral Examination:

14 May 2021

Contents

Abbreviations

IFs	Intermediate filaments
SHC	Sequence homology class
NF	Neurofilament
ULF	Unit-length filament
PTMs	Post-translational modifications
AFM	Atomic force microscopy
Tris	Tris-(hydroxymethyl)-aminomethane
EDTA	Ethylenediaminetetraacetic acid
EGTA	Ethyleneglycol-bis(β-aminoethylether)-N,N,N',N'-tetra-acetic acid
HCl	Hydrochloride acid
DMSO	Dimethyl sulfoxid
PB	Phosphate buffer
TB	Tris buffer
NaCl	Sodium chloride
MES	2-(N-Morpholino)-ethanesulfonic acid sodium salt
EDC	1-Ethyl-3-(3-dimethyl aminopropyl)carboxiimide)
PBS	Phosphate buffered saline
BSA	Bovine serum albumin
MgCl$_2$	Magnesium dichloride
ATP	Adenosine triphosphate
PKA	Protein kinase A
SDS	Sodium dodecyl sulphate
DTT	Dithiothreitol
PFA	Paraformaldehyde
GA	Glutaraldehyde
SAXS	Small angle X-ray scattering
PLL-PEG	Poly(ethyleneglycol and poly-L-Lysine)-PEG
DST	Disulfosuccin-imidyl tartrate

1

Introduction

The capability of eukaryotic cells to resist large deformations, to transport intracellular cargo and to adapt the cell shape, for example during migration or embryonic development, depends on the cytoskeleton, a composite network of three types of filamentous proteins: actin filaments, microtubules and intermediate filaments (IFs) [1]. The physical properties of cells are controlled by the architecture of these cytsokeletal filaments and networks [1] and different expression levels of various proteins or protein modifications lead to variation of the mechanical properties of cells. The individual components of the cytoskeleton differ in their diameter, their assembly process, their mechanical properties and interaction partners as well as their function. Whereas actin and tubulin are expressed throughout all cell types, different types of IF proteins are expressed in a cell-type specific manner. In general, IFs are believed to function as supporters for the mechanical resistance of cells. Over the past few years, particularly the role of the IF protein vimentin gained importance for its role in cell mechanics. It was shown, for example, that vimentin builds a cage-like network surrounding the nucleus [2] which might help to protect the nucleus. Furthermore, different IF proteins seem to be highly involved in diseases such as cancer: the IF protein vimentin, for instance, is linked to tumorigenesis, epithelial-to-mesenchymal transition and the metastatic spread of cancer [3].

In this thesis the mechanics of individual vimentin filaments are probed by using an optical trapping setup which is combined with microfluidics and confocal imaging. Optical traps allow for contact-free measurements of individual proteins in pure buffer and by combining them with microfluidics, the protein environment can be varied easily while simultaneously observing changes in the mechanics. To be able to compare the results of single filament mechanics to network mechanics, we measure vimentin networks at different conditions with passive microrheology. This method allows us to obtain mechanical properties of networks in small volumes in the micro liter range by tracking micrometer-sized particles embedded in the network [4]. From these particle tracks the mean-squared displacement can be calculated and thereby the viscoelastic response of the network can be derived [4].

In Chapter 2 an overview of the theoretical fundamentals of the used methods and a corresponding state of the art is provided. It covers an overview of IFs, including their biological as well as their mechanical properties. In order to model their mechanical responses, different theoretical models for biopolymers are described and the last sections cover the measuring methods: optical traps and mircrorheology. Chapter 3 provides an overview of the sample preparation, the measuring process and the data analysis. To characterize the mechanical properties of the intermediate filament vimentin, different approaches are used. First, the stretching behavior of vimentin filaments during cyclic loading are analyzed in Chapter 4. These results unveil the recovery behavior of vimentin upon stretching which plays an important role in the protection of cellular integrity against large deformations. Second, the influence of post-translational modification of vimentin on the mechanical properties is investigated in Chapter 5. This approach provides further insights into the molecular and hierarchical structure of vimentin showing how this post-translational modification may allow for a rapid, local adaption of the mechanical properties within the cell. In the last results part in Chapter 6, we investigate whether our findings for the influence of modifications on single vimentin filaments apply to larger scales as well. Therefore, we study the mechanics of vimentin networks with the same modifications as in Chapter 5 with passive microrheology. This study of the mechanics of whole networks is important as it models the condition of vimentin filaments within cells. Finally, in Chapter 7 all the results of the different experiments are summarized, the conclusion of this thesis is formulated and possible further experiments and open questions are discussed.

2

Theoretical Background and State of the Art

2.1 Biological Background of Intermediate Filaments

The cytoskeleton of metazoan cells consists of three types of filamentous proteins: actin, microtubules and IFs (shown in Fig. 2.1). Actin and tubulin are expressed ubiquitous all cell types, whereas IFs are expressed in a cell-type specific manner. In humans about 70 genes encode for different types of IFs [5]. For example the protein
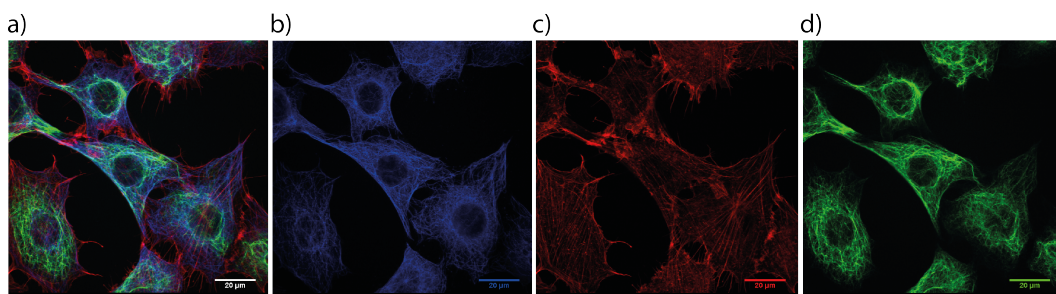

Figure 2.1: *Different components of the cytoskeleton in NIH 3T3 cells. a) Fluorescence image of the three components of the cytoskeleton. b) Staining of the microtubules. c) Staining of the actin filaments. d) Staining of vimentin filaments. Scale bar corresponds to 20 μm. Image courtesy of Ulrike Rölleke.*

vimentin is the most abundant IF protein and is expressed in cells of mesenchymal origin, while epithelial cells express keratins [6]. IFs vary in different ways from the other two components of the cytoskeleton: in their structure and their expression in cells as well as in their mechanical properties.

2.1.1   Structure of Intermediate Filaments

To understand the properties of IFs in more detail, we need to consider their common structure. Even though there is a large number of different IF proteins, they all share the same secondary structure [7–9]. The secondary structure of IF monomers consists of an α-helical rod domain flanked by intrinsically disordered head and tail domains [10–13], as shown in Fig. 2.2. The rod domain consists of three coils, namely 1A, 1B and 2, which are connected by linkers L1 and L12, see Fig. 2.3. The amino acid sequence of the rod contains heptad repeats (a-b-c-d-e-f-g)$_n$ where a and d are usually apolar amino acids which is common for a left-handed coiled-coil structure [9, 11, 14]. However, this pattern is disrupted in coil 2 at the so-called stutter region, a short part where the sequence follows a hendecad repeat [15]. X-ray diffraction analysis of a fragment of a vimentin dimer revealed that this hendecad pattern is located towards the end of coil 2 but it does not destroy the coiled-coil geometry [15, 16]. In this segment of the vimentin dimer with the stutter, the two supercoiled α helices run almost parallel to each other while following the coiled-coil geometry [15, 16]. It is hypothesised that all other IF proteins also have this heptad discontinuity, for example dimers of lamin A show a very similar structure compared to vimentin and around the stutter it is even identical [17].
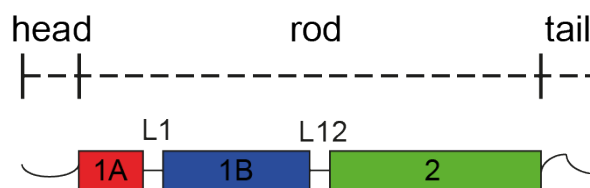
Figure 2.2: *Sketch of the structure of an IF monomer.*

2.1.2 Comparison of Different Intermediate Filament Proteins

As mentioned before, there are about 70 different genes encoding for IFs and they can be divided into five groups according to sequence homology classes SHC 1-SHC 5 [18]. This grouping reflects their biological function as well as their tissue origin.

Table 2.1: *Groups of IFs according to their sequence homology classes. Table adapted from Ref. [18].*

class	examples for proteins	occurrence
SHC 1	acidic keratins	epithelial cells
SHC 2	basic keratins	epithelial cells
SHC 3	vimentin, desmin, glial fibrillary acidic protein	mesenchymal cells, muscle cells, glia cells, astrocytes
SHC 4	neurofilaments (NF-L, NF-M, NF-H)	neurons
SHC 5	lamins (lamin A/C, lamin B)	nucleus

Keratins are grouped into SHC 1 and SHC2, where acidic keratins belong to SHC 1 and basic keratins belong to SHC 2. Interestingly, keratin filaments are always heterodimers consisting of one type 1 and one type 2 keratins [19, 20]. The proteins from either SHC 3 and SHC 4 are homopolymer-forming IFs but they are also able to form heteropolymers within one group or between these two groups [18]. The proteins vimentin, desmin and glial fibrillary acidic protein belong to the group SHC 3 and the neurofilament (NF) triplet proteins NF-L, NF-M and NF-H belong to the group SHC 4. Nuclear lamins are associated to the group SHC 5 and they do not co-assemble with proteins of any other group. Moreover, the different IF proteins vary in their primary sequences [21]. For example, the rod domain of lamins contains 42 additional amino acids compared to the cytoplasmic IFs (SHC 1-SHC 4) [22], but also the head and tail domains differ in size and in their amino acid sequence between different IF proteins. To conclude, different IFs are expressed in different cell types and there, they fulfill different functions.
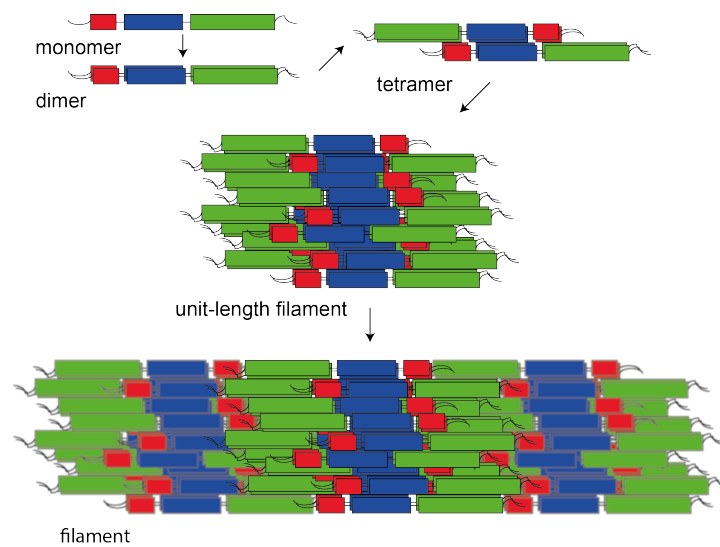
Figure 2.3: *Sketch of the hierarchical assembly pathway of IFs.*

2.1.3   Assembly of Intermediate Filaments

All types of IFs do not only share the same secondary structure but also the hierarchical assembly pathway. The complete assembly process, apart from the additional compaction step, is sketched in Fig. 2.3 and is as follows: two monomers align and form a coiled-coil dimer, subsequently two dimers form an antiparallel, halfstaggered tetramer, multiple tetramers then form a so-called unit-length filament (ULF) with a length of about 58 nm [12] and longitudinal annealing of ULFs leads to elongated filaments with a diameter of about 10 nm [9]. The number of tetramers assembling to a ULF varies for the different types of IFs. The ability of keratins to form dimers in presence of 5 M urea [23] and for vimentin to form dimers in presence of 6 M Urea and tetramers in 4.5 M urea [12] is noteworthy for proteins. Additionally, the formation of IFs does not require additional energy but for the assembly to ULFs and elongated filaments *in vitro*, additional ions or a change in pH is required. It is important to note that there are different factors that influence the speed of the assembly process, such as the protein concentration, temperature and present ions [24]. The general assembly process of IFs can be divided into two steps with different time scales, the formation of the ULF which is very fast and takes place within seconds and the elongation to filaments which is a matter of minutes [25, 26].

2.1.4 Modification of Intermediate Filaments

The mechanical properties of cells and tissues highly influence their function, and, importantly, need to flexibly adapt, *e.g.* during embryonic development, wound healing or cancer metastasis, where tissues are rapidly and extensively deformed. Adaptation may occur by differential expression of structural proteins, such as cytoskeletal filaments but this is a comparatively slow process. A faster mechanism to modify IFs after their translation are so-called post-translational modifications (PTMs). These result either in a covalent modification of the functional group of the corresponding amino acid or they introduce a new functional group, like a phosphate group. These PTMs do not only modify the protein itself but also provide the possibility to bind to other proteins, such as signaling proteins. One example of these binding partners for modified vimentin IFs is the protein 14-3-3 [27]. The protein 14-3-3 is involved in several cellular processes like signal transduction, adhesion and inhibition of tumorigenesis [28] and its role depends on the interaction partner. For instance it binds to keratin during the cell cycle [29] or it can affect the assembly dynamics of neurofilaments [30]. There are multiple kinds of PTMs, such as phosphorylation, glycosylation, sumoylation and acetylation and the modifications are conducted by different PTM enzymes. The most studied PTM for IFs is phosphorylation, which is the addition of a negatively charged phosphate group to the amino acids serine, threonine or tyrosine through a phosphoester bond, typically in the head and tail domain [31]. Previous studies have shown that phosphorylation of vimentin and keratins promotes protein solubility and, thereby, enables disassembly and reorganization of the IF network [31, 32]. Phosphorylation of neurofilaments probably leads to a decrease of the speed of axonal transport caused by bundling of the neurofilaments [33–35].

2.2 Mechanics of Single Intermediate Filaments

2.2.1 Experiments on Intermediate Filaments

The first experiments on IF mechanics on single IFs were performed already in 1924 by Shorter who investigated the stretching behavior of wool, *i.e.* hard-α-keratin. Hard-α-keratins have a higher amount of cysteins compared to cytoplasmic keratins which results in an increase in disulfide bonds and, therefore, those keratin filaments are more stable compared to cytoplasmic keratins. Shorter explained his observations

with a model consisting of two springs connected in series with one spring working in a viscous medium and the other one being free [36]. In his experiments, he showed that wool that was stretched up to 40% is able to fully recover to its initial length upon relaxation and that this process was much faster when the fibers were wet compared to experiments with lower humidity [36]. He also observed the different regimes for these fibers during stretching and relaxation and these observations could be covered with the two-spring model. Later on in 1927, Speakman found a loading rate dependent behavior of the extensibility and the breaking load of single wool fibers [37].

The first X-ray experiments of unstretched and stretched hard-α-keratins performed by Astbury revealed differences in the structure of the polypeptide chain. Astbury observed that the structure of stretched keratin is comparable to natural silk which is composed of β-keratins and the structure of unstretched keratin corresponds to α-keratins. He concluded that the difference in structure arises from the polypeptide chain which is folded in the unstretched keratin and extended in the stretched state [38–40]. Later on, Bendit studied the α-β-transition in wool by X-ray diffraction experiments. He found that the transition from α to β patterns occurs already at very low extensions of 5% or less [41–43].

Nowadays, there are multiple different approaches to investigate the mechanical properties of IFs and one has to distinguish between the diverse measurement levels which are bundles of IFs, whole networks or single filaments. For example, the mechanics of individual IFs can be studied by using atomic force microscopy (AFM) experiments. For these experiments, IFs are assembled *in vitro* and placed on a solid support in physiological buffer where they can adsorb to the surface. By moving the AFM tip across the filament, the single IFs are displaced laterally or stretched and subsequently imaged to obtain the elongation of this displacement [44, 45]. This method revealed the high extensibility of the filaments as it is possible to stretch them to a maximum of 3.6-fold and this leads to the hypothesis that IFs may function as mechanical shock absorbers in cells [44]. Different stretching regimes for single IFs were found: the filaments are fully elastic at small strains and forces and further extensions lead to a strain hardening in the AFM experiments [45].

To exclude the influence of the surface, optical tweezers are employed to investigate the mechanical properties of single IFs. Optical tweezers allow for contact-free measurements in any buffer system. For these experiments, a pair of beads is trapped and in between a single filament is bound to the beads. By moving one of the beads, the filament is stretched and the force needed for stretching is measured. During

this stretching of single vimentin filaments, three different regimes can be observed in the force-strain curves: 1) a linear, elastic increase, 2) a plateau region and 3) a subsequent stiffening of the filament [46–49], as shown in Fig. 2.4.
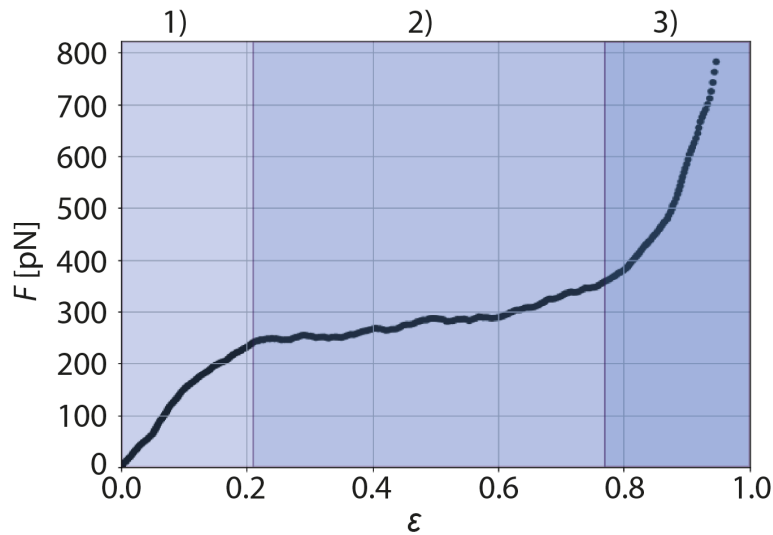
Figure 2.4: *Different regimes in a force-strain plot for vimentin filaments stretched with optical tweezers.*

These different regimes can be assigned to structural changes within the rod domain of vimentin IFs from α helices to β sheets which will be explained in more detail in the following sections. Furthermore, optical trapping experiments on single vimentin IFs revealed that IFs are able to dissipate large amounts of energy which could protect the cellular integrity and this assumption further strengthens the role of vimentin IFs as shock absorbers [50].

2.2.2   Variation of Mechanical Properties of Intermediate Filaments

Even though there is a high similarity between different types of IFs, they all have different mechanical properties, as shown for example for single vimentin and keratin filaments [51]. Already small changes in the amino acid sequence lead to completely different stretching behaviors for these filaments. But also the mechanical and structural properties for one type of IF can be individually tuned by the presence of different ions or variation of the pH [52, 53]. The change of mechanics can be explained by electrostatic interactions of subunits within the filament. These results suggest that it is possible to locally modify the mechanical properties of the cell by the availability of different ions without changing the entire cytoskeleton [52].

2.2.3 Simulation of Intermediate Filament Mechanics

There are different approaches to simulate the mechanics of intermediate filaments under load. The first approach is molecular dynamics simulation of vimentin dimers or tetramers [47, 54] which is very useful to describe the transition from α helices to β sheets in the rod domain during stretching. In Ref. [47, 54], the simulations show the same regimes during stretching as described here in the previous section. An advantage of this method is that a high resolution of the stretching on single amino acid level is possible which allows to associate the different regimes to structural changes in the vimentin dimer and tetramer. Nevertheless, an entire vimentin filament cannot be described with this method as excessive computational effort would be required.

The second approach enables the modelling of the entire vimentin filament by using a two-state model which fits the experimental force-strain stretching curves of vimentin, as shown in Fig. 2.4 [49, 55]. The principle of this approach is described in more detail in Section 2.3.3.

The third approach uses Monte-Carlo simulations to describe the hysteresis and tensile memory of vimentin filaments during cyclic stretching [50]. In this model, the vimentin filament is described by springs and elements that can open and elongate to an unfolded state [50]. The length of a ULF is determined by the shortest element which means if there is one element in the folded state, *i.e.* an α helix, and all the other 31 elements in an unfolded state, the respective ULF is in the short state. This model is described in more detail in Ref. [50]. The Monte-Carlo simulations can be extended to describe other IFs or the effect of modifications of IFs. This is done by taking lateral association forces between dimers, tetramers or other subunits within a ULF into account and this extension is described in detail in Subchapter A.2 and in Ref. [51].

2.3 Polymer Theory

Polymers are composed of a large number of repeating monomers [56]. Most types of biological material such as DNA, the components of the cytoskeleton and proteins in general can be described as polymers. There is a variety of physical models for describing different polymers depending on the characteristics of the polymers and the necessary accuracy of description. Two basic models to describe biopolymers are

the freely-jointed chain and the worm-like chain which will be described in more detail.

2.3.1 Worm-Like Chain

To describe cytoskeletal filaments which can bend very smoothly, the worm-like chain model can be used. This model by Kratky and Porod describes ideal flexible and bendy thin filaments [57–59], a sketch being shown in Fig. 2.5a. The difference compared to the freely-jointed chain model or the Kuhn chain model, which describes a polymer consisting of independent successive rigid monomers with a fixed length l that are linked by perfectly flexible joints, is a change in the limit to a continuous chain by moving the step length l to zero and the number of monomers N to infinity [60]. In Fig. 2.5 an elastic filament with a segment length s and a constant curvature
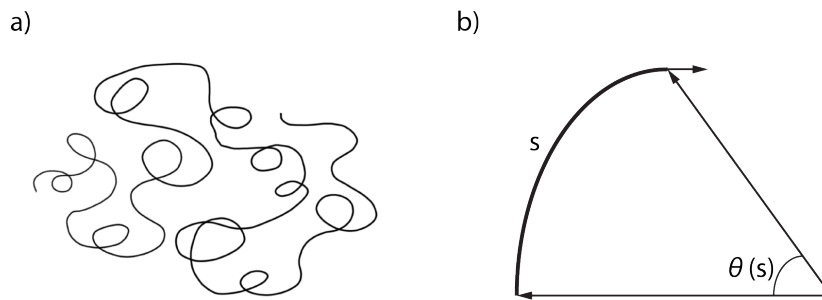
Figure 2.5: *a) Schematic representation of a worm-like chain. b) Segment of an elastic filament with length s and a curvature of θ/s. Adapted from [60].*

θ/s is shown and the elastic bending energy ΔU of that segment can be calculated by Hooke's law

$$\Delta U = \frac{1}{2} \cdot s \cdot \kappa_b \cdot \left(\frac{\theta}{s}\right)^2 , \tag{2.1}$$

with κ_b denoting the bending rigidity constant [60]. This equation can then be used to calculate the mean square bending angle $\langle \theta^2 \rangle$ as an average at thermal equilibrium [60]

$$\langle \theta^2 \rangle = 2 \frac{\int \exp(-\Delta U/k_B T) \theta^2 \, d\theta}{\int \exp(-\Delta U/k_B T) \, d\theta} = 2 \frac{s}{\kappa_b} k_B T. \tag{2.2}$$

The persistence length L_p is a mechanical property that describes the bending stiffness or the flexibility of a polymer and it describes the length scale where the orientation correlation is lost. When two vectors are separated by a distance s along the contour

of the filament, the directional correlation $\langle \cos \theta(s) \rangle$ decreases exponentially [60]

$$\langle \cos \theta(s) \rangle = \exp \left(-\frac{|s|}{L_p} \right). \tag{2.3}$$

This shows that two points along the filament that are closer than the persistence length ($s \ll L_p$) are likely to have similar orientations, *i.e.* tangential vectors, whereas points that are further apart which are more likely to have different orientations [59]. For a smaller length $s \ll L_p$ a Taylor expansion of the cosine term and the exponential up to the first order in the lengths s is possible

$$1 - \frac{1}{2} \langle \theta^2(s) \rangle \approx \langle \cos \theta(s) \rangle = \exp \left(-\frac{|s|}{L_p} \right) \approx 1 - \frac{s}{L_p}. \tag{2.4}$$

From these two estimations directly follows $\langle \theta^2(s) \rangle = 2\frac{s}{L_p}$ and with eq. (2.2) $L_p = \frac{\kappa_b}{k_B T}$ [60].

The end-to-end vector $\vec{h}_E$ for a worm-like chain can be calculated by [60]

$$\vec{h}_E = \int_0^L \vec{l}(s) \, \mathrm{d}s, \tag{2.5}$$

with $\vec{l}(s)$ being the tangential vector at a distance s from the start of the chain and L being the contour length of the polymer. The mean square end-to-end distance is calculated by [60]

$$\begin{aligned}
\langle R^2 \rangle &= \int_0^L \vec{l}(s) \, \mathrm{d}s \cdot \int_0^L \vec{l}(s') \, \mathrm{d}s' \\
&= \int_0^L \int_0^L \langle \cos \theta(s - s') \rangle \, \mathrm{d}s \, \mathrm{d}s' \\
&= \int_0^L \int_0^L \exp \left(\frac{-|s - s'|}{L_p} \right) \mathrm{d}s \, \mathrm{d}s' \\
&= 2L_p^2 \cdot \left[\frac{L}{L_p} - 1 + \exp \left(-\frac{L}{L_p} \right) \right],
\end{aligned} \tag{2.6}$$

with two limiting situations of interest: $L \ll L_p$ and $L \gg L_p$, representing the case of a freely-jointed and a worm-like chain, respectively. For the first case $\langle R^2 \rangle$ approaches L^2 which would be expected for a nearly straight filament rod. In the second case, $\langle R^2 \rangle$ approaches $(2L \cdot L_p)$ and this result agrees with the freely-jointed chain model if the segment length equals $2L_p$. Therefore, $2L_p$ is called the statistical Kuhn length of the worm-like chain model [59]. Due to the definition that there is no

orientation correlation between Kuhn segments, the orientation correlation is lost when the distance reaches twice the persistence length of the filament [60].

2.3.2   Entropic Elasticity

Filaments can exert forces when being stretched [59]. This effect is called entropic elasticity and it is due to the fact that there are less possible configurational states available when the filament is stretched [59]. For small displacements, the freely-jointed and worm-like chain act as ideal springs:

$$F = \frac{3k_BT}{lL}x \qquad \text{and} \qquad F = \frac{3k_BT}{2LL_p}x, \qquad (2.7)$$

with the spring constants $\frac{3k_BT}{lL}$ and $\frac{3k_BT}{2LL_p}$, respectively [59]. Here, x is the distance between the two ends of the filament. This force-extension relationship allows to calculate the extension of large and small displacements for the freely-jointed chain by [59, 61]

$$x = L\coth\left(\frac{F\cdot l}{k_BT} - \frac{k_BT}{F\cdot l}\right). \qquad (2.8)$$

Large displacements for the worm-like chain model can be approximated by [59, 62]

$$F = \frac{k_BT}{L_p}\left[\frac{1}{4}\left(1 - \frac{x}{L}\right)^{-2} - \frac{1}{4} + \frac{x}{L}\right]. \qquad (2.9)$$

Nevertheless, the worm-like chain model is a simple model and deviations from its predictions can be expected. In reality, forces do not diverge towards infinity when the extension approaches the contour length but the filaments will break apart [59]. To cope with these deviations for highly stretched filaments, for example a linear elastic stretch modulus term can be added to the worm-like chain model [59].

2.3.3   Two-State Model

Considering IFs, they are not only bendy but they can be stretched and during stretching, two different conformational states of the rod domain were observed early on: the rod domain can be in the α-state for the unstretched filament or at low strains or in the β-state for larger strains [38–40]. Due to the conformational changes in the filament, the models need to take the change of the contour length into account. Such a model was introduced to describe the stretching behavior of wool fibers [63].

This two-state model was then further developed and it was shown that it could reproduce data for a variety of biopolymers that undergo conformational transitions [64]. The IF or the biopolymer consists of modules that undergo a transition upon stretching between two energetically different states (A and B) in which the modules have a different length (l_f for the folded state and l_u for the unfolded state) [64]. As described before, the polymer consists of N monomers, N_f of which are in the folded state and N_u of which are in the unfolded state. This leads to a new definition of the contour length L which is described by

$$L = N_f \cdot l_f + N_u \cdot l_u. \tag{2.10}$$

The force-extension relation for a worm-like chain given by eq. (2.9) needs to be extended to be able to describe the actual polymer contour length at a given force. For the unfolding of the polymer, *i.e.* the transition from state A to state B, the rate k_0 is given by [64]

$$k_0 = \omega \exp\left(-\frac{\Delta E}{k_B T}\right), \tag{2.11}$$

with ω being the reciprocal of a diffusive relaxation time [65] and ΔE denoting the activation barrier, *i.e.* the energy needed for the unfolding process, as shown in Fig. 2.6. Bell and Evans considered the influence of an external force on the unfolding

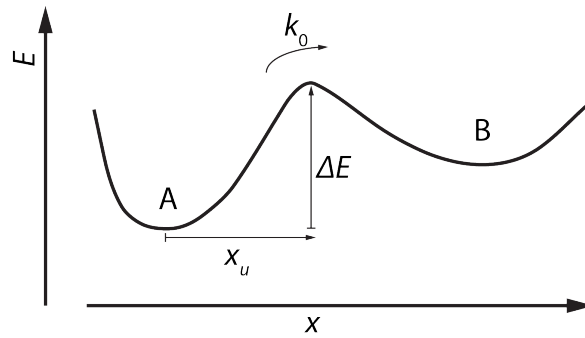**Figure 2.6:** *Sketch of the energy landscape for the two-state model. The energetically lower state A describes the folded polymer and the energetically higher state B describes the unfolded polymer. Adapted from [64].*

rate and this leads to the force dependent unfolding rate

$$k(F) = \omega \exp\left(-\frac{\Delta E - F \cdot x_u}{k_B T}\right) = k_0 \exp\left(\frac{F \cdot x_u}{k_B T}\right), \tag{2.12}$$

with x_u being the width of the activation barrier and F being the applied force [64–66]. When the polymer is stretched with a constant speed v_c, an elongation Δx at each time interval Δt of

$$\Delta x = v_c \Delta t, \tag{2.13}$$

can be observed. The probability that a folded monomer of the polymer undergoes an unfolding event from state A to state B is given by [64]

$$\mathrm{d}P_u = N_f k_0(F) \Delta t. \tag{2.14}$$

For the case of IFs, the polymer does not consist of a single chain of monomers but several monomers in parallel (the ULF). To take this fact into account, two cases are considered: in the first case (coupled) the IF elongates, when all monomers of one ULF are in the unfolded state [50] and in the second case (uncoupled) the IF elongates when all monomers within one subunit, for example within one tetramer, are in the unfolded state [51]. The difference between those two cases is how the force is shared among the monomers [51] and the mechanically different behavior of different types of IFs can be explained by the two different coupling cases. Simulations of the coupled model reproduce the stretching behavior of untreated single vimentin IFs [50] and simulations of the uncoupled model can reproduce the stretching of single keratin IFs [51].

2.4 Fundamentals of Fluorescence Microscopy

To obtain images of single IFs, fluorescent molecules can be attached to IF monomers which then can be observed by fluorescence microscopy. Fluorescence microscopy is based on the chemical property of some molecules to be excited by a photon which carries a energy $h\nu$ corresponding to the transition between the molecular energy levels. This effect is called absorption. Following the absorption, the phenomenon of fluorescence describes the emission of a photon as a result of an electron returning from an excited state back to the ground state. The absorbance can be calculated using the Beer-Lambert law

$$A = \log\left(\frac{I_0}{I}\right) = c\epsilon_\lambda l, \tag{2.15}$$

with I_0 being the intensity of the incident light, I the intensity of the transmitted light, c the molar concentration of the absorbing molecule, ϵ_λ the extinction coefficient at a specific wavelength λ and l the optical path length [67]. This equation can also be used to calculate the concentration of an unknown sample by measuring the absorbance.

To graphically describe the decay of an excited electron to the ground state, the Jablonski diagram [68] can be used, as shown in Fig. 2.7. If a fluorophore is excited by
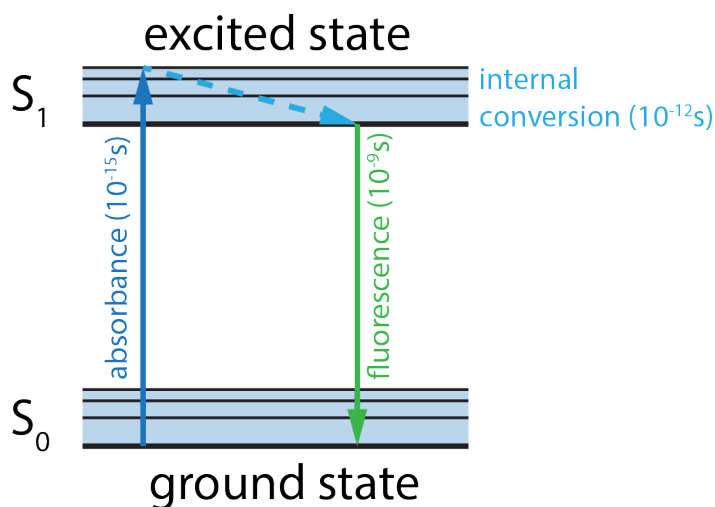
Figure 2.7: *Jablonski diagram. A molecule gets to an excited state S_1 by absorbing a photon, indicated by the blue arrow. From this excited state, the molecule looses energy in a non-radiative manner to a lower vibrational state (internal conversion) of the excited state, indicated by the dotted light blue arrow. Fluorescence occurs when the molecule relaxes to the ground state by emitting a photon, indicated by the green arrow.*

a photon, it leaves the ground state S_0 and gets to the excited state S_1. The molecule looses some energy in a non-radiative manner to a lower vibrational state and this process is called internal conversion. Because of the reduction of the energetic state due to the internal conversion, fluorescence occurs at lower energies compared to the absorption and, therefore, the emitted light has a longer wavelength. This shift in wavelength is called Stokes shift [69].

An important characteristic of a fluorophore is the quantum yield Q, which is the ratio of the number of emitted to the number of absorbed photons

$$Q = \frac{k_f}{k_f + k_{nr}},\tag{2.16}$$

with k_f being the rate of radiative decay, *i.e.* fluorescence, and k_{nr} being the rate of non-radiative decay [67]. Due to the internal conversion, the quantum yield is always

lower than 1. The fluorescence lifetime τ is obtained from [67]

$$\tau = \frac{1}{k_f + k_{nr}}. \tag{2.17}$$

This principle of fluorescence is used in fluorescence microscopy. The basic structure of a so-called epi-fluorescence microscope is as follows: for the setup, a light source is used which emits light, for example laser light or white light with appropriate spectral filters towards the sample. In front, there is a dichroic mirror which reflects the excitation light and the emitted light can pass through. The reflected light with the appropriate wavelength is focused with an objective on the sample. Thereby it excites the fluorophores which are usually bound to the examined structure, for example fluorescently labeled vimentin IFs. As described above, the emitted fluorescence light has a longer wavelength compared to the excitation light and, therefore, it passes through the dichroic mirror without being reflected.

2.5   Optical Traps

2.5.1   Development of Optical Traps

In the early 1900s it was discovered that light can exert forces to matter. In the 1960s Arthur Ashkin conducted an experiment where he focused an argon laser into a suspension of transparent latex microparticles in water. He discovered that the particles were pushed along the direction of the laser beam and that spheres at the periphery were drawn towards the center of the beam [70, 71]. Ashkin proposed different applications of the optical trap, such as the potential to manipulate or trap macromolecules, polymers or biological particles [71]. Ashkin was the first to apply this method to biological systems by trapping and manipulating viruses and bacteria and he revealed the need to change to an infrared laser to reduce damage to the biological samples [71–73]. With this improvement, it was possible to trap and manipulate different kinds of cells but also proteins or DNA [71]. Block *et al.* invented a method to measure the forces generated by the flagella of *E.coli* and *Streptococcus* bacteria [74]. Shortly after this discovery, Ashkin trapped mitochondria within cells that were transported along microtubules by the motor protein dynein. With these measurements he could estimate the force generated by dynein while transportation of organelles and, in fact, he performed the first measurement of forces within living cells [75]. By combining optical traps with interferometry, Svoboda *et al.* were able

to detect the position of the trapped particle and thereby observe the motion of the protein kinesin walking along microtubules in 8 nm steps [71, 76]. New possible applications for optical trapping experiments evolved and soon the first experiments on DNA were performed. First, the elasticity of single-stranded and double-stranded DNA was probed [77] and later on, RNA polymerase, a powerful motor protein that copies DNA to RNA, was investigated [78]. Regarding the application of optical traps in research on the cytoskeleton, it was shown that nonmotor microtubule-associated proteins can generate frictional forces in dynamic cytoskeletal networks [79]. Moreover, it was shown that diffusible microtubule cross-linkers generate directed microtubule sliding when these cross-linkers are confined between over-lapping microtublues [80]. Recent studies showed that it is possible to manipulate membranes with optical traps. Optical traps were used to fuse individual membrane domains with one another or the lipid composition of a vesicle was altered by adding new membrane material through fusion [81]. Until today, optical traps were further developed and the field has broadened, from measuring Ångstrom-scale movements to hybridizing with other single-molecule techniques [71].

2.5.2   Fundamentals of Optical Traps

Physical Background

Generally spoken, an optical trap consists of a highly focused laser beam that can trap and manipulate small dielectric objects that have a different refractive index compared to the surrounding solution. The underlying principle of an optical trap is the fact that light carries momentum and a change in momentum is a force. These forces occur due to an interaction between the focused laser beam and the trapped object [82]. This can be explained by a combination of ray optics using momentum conservation and the refraction of rays by Snell's law [82]

$$k_i = k_0 \cdot n_{\text{water}} \cdot \sin(\theta_i) = k_0 \cdot n_{\text{bead}} \cdot \sin(\theta_t) = k_t, \qquad (2.18)$$

with the length of the wave vector in vacuum $k_0 = 2\pi/\lambda$, with λ denoting the wave length, the refractive indices for water $n_{\text{water}} \approx 1.33$ and the polystyrene bead $n_{\text{bead}} \approx 1.59$ and the incident angle θ_i and transmitted angle θ_t. Here, k_i describes the length of the wave vector of the incident ray and k_t the transmitted ray. Commonly for optical trapping experiments a laser wavelength in near infrared is used to minimize both, the absorption by water and the damage of the biological sample [83]. Fig. 2.8

shows a sketch of the trapped particle at a distant position from the focus of the laser beam. It illustrates how two incident rays $k_{i,1}$ and $k_{i,2}$ get refracted as they pass
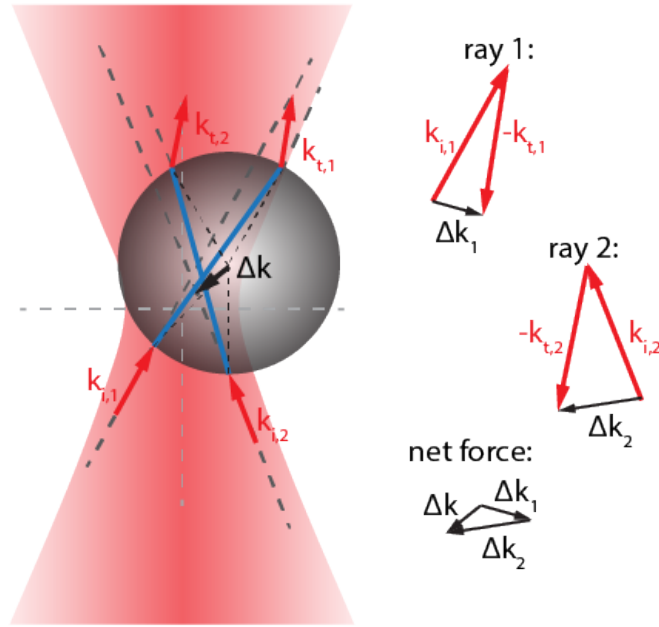

Figure 2.8: *Sketch of the ray optics. Forces acting on a bead in a highly focused laser beam. Adapted from [82].*

through the particle with a different refractive index compared to the surrounding medium (water) and the transmitted rays $k_{t,1}$ and $k_{t,2}$ get refracted a second time as they exit the particle. Therefore, the ray is deflected from its initial pathway which leads to a change in momentum Δk_1 and Δk_2 (calculated by $\Delta k_n = k_{i,n} - k_{t,n}$). Due to the conservation of momentum, the change of the total momentum is zero and the trapped particle experiences a force according to the compensatory momentum Δk which pulls the bead towards the focus of the laser [82].

This assumption is only valid for particles with a diameter $d \gg \lambda$, with λ being the wavelength of the laser which is approximately $1\,\mu m$. This assumption often is not true for particles used for biophysical trapping experiments. To overcome this problem, the Rayleigh approximation can be used which considers the diameter of the particle $d \ll \lambda$. In this theory, the particle is treated as a dipole which interacts with the electric and magnetic fields of the laser. The optical force $\vec{F}_{opt}$ acting on the particle can be calculated by integration over the volume V of the scatterer. The optical force can be divided into two parts, the gradient force $\vec{F}_{grad}$ and the scattering force $\vec{F}_{scat}$

$$\vec{F}_{opt} = \int_V \vec{f} \, dV = \vec{F}_{grad} + \vec{F}_{scat}, \tag{2.19}$$

where $\vec{f}$ denotes the force density inside the scatterer. For small particles, the intensity gradient does not vary a lot over the volume of the particle and therefore the gradient force can be written as [84]

$$\vec{F}_{\text{grad}} = \frac{n_{\text{water}}\mathfrak{Re}(\alpha)V}{2c}\nabla I(\vec{x}). \tag{2.20}$$

Here, α is the polarizability, c the speed of light and I the intensity of the laser. The gradient force for small displacements x depends linearly on the displacement [82]. Due to the Gaussian beam profile of the laser, the gradient and the linear force relationship can be calculated by

$$\vec{F}_{\text{grad}}(\vec{x}) = \vec{F}_{\text{grad}}\Big|_{\vec{x}=0} + \nabla\vec{F}_{\text{grad}}\Big|_{\vec{x}=0}\vec{x} + \mathcal{O}(\vec{x}^2)$$

$$\approx \frac{n_{\text{water}}\mathfrak{Re}(\alpha)VI_0}{\sqrt{8\pi}c}\begin{pmatrix} \frac{1}{\sigma_x^3} & 0 & 0 \\ 0 & \frac{1}{\sigma_y^3} & 0 \\ 0 & 0 & \frac{1}{\sigma_z^3} \end{pmatrix}\vec{x} = -\boldsymbol{\kappa}\cdot\vec{x}, \tag{2.21}$$

with the diagonal matrix $\boldsymbol{\kappa}$ being the so-called trap stiffness [82]. The scattering force F_{scat} cannot be calculated in a simple way but by using the Rayleigh-Gans theory it can be described as a function of the scattering and extinction cross-sections [82, 85]. However, for the linear force regime, $\vec{F}_{\text{scat}}$ is approximately constant for all displacements [82].

Calibration

There exists a variety of methods to calibrate the optical trap. One method uses the assumption that optical traps can be described by Hookean springs. As described above, for small displacements the force is proportional to the displacement of the bead from the center of the laser beam

$$F = -\kappa_{\text{trap}}\cdot x, \tag{2.22}$$

with F being the force, κ_{trap} the spring constant of the trap or the so-called trap stiffness and x the displacement of the bead. In order to obtain the motion of the particle within the optical trap, the Langevin or Power-Spectrum approach can be applied. The Langevin equation describes the displacement of a trapped particle due

to thermal forces F_{th} by

$$\gamma \dot{x} + \kappa x = F_{\text{th}}, \tag{2.23}$$

where the drag coefficient γ is given by $\gamma = 3\pi D\eta$ which describes the random movement of a sphere with a diameter D in a fluid with viscosity η. The thermal forces average to zero for different times and due to the used setup, we have very low Reynolds numbers and therefore, inertia can be neglected. According to the fluctuation dissipation theorem, the force spectrum can be described by white noise

$$\langle F_{\text{th}}(t) F_{\text{th}}(t') \rangle = 2\gamma k_B T \delta(t - t'), \tag{2.24}$$

with δ being the Dirac delta function [82] which indicates that the forces at time t are uncorrelated to the forces at another time t'. Performing a Fourier transformation of the Langevin equation, see eq. (2.23),

$$-i\omega\gamma\tilde{x}(\omega) + \kappa\tilde{x}(\omega) = \tilde{F}_{th}(\omega), \tag{2.25}$$

allows to directly calculate the power-spectral density (PSD) [82]

$$PSD(\omega) = |\tilde{x}(\omega)|^2 = \frac{2k_B T}{\gamma} \frac{1}{\omega^2 + \omega_c^2}. \tag{2.26}$$

The so-called corner frequency $\omega_c = \kappa/\gamma$ is the frequency at which the power is reduced by 50% compared to the PSD at the time point $t = 0$. We have to distinguish two different cases. First, if the detector sensitivity is known and we have calibrated positions $x(t)$, the amplitude $PSD(t = 0) = 2k_B T\gamma/\kappa$ combined with the corner frequency $f_c = \omega_c/2\pi$ can be used to calculate the trap stiffness and the drag coefficient [82]. Second, if the detector sensitivity is unknown, we need information about the size of the particle and the viscosity of the used medium to be able to calculate the trap stiffness.

It is important to note that this calibration method can be used for *in vitro* measurements. For measurements inside a living cell other approaches have to be used. This is due to the fact that the calibration of a bead outside of the cell cannot be transferred to a system with a bead inside the cell as the intracellular visco-elastic environment is completely different to the environment outside the cell [82].

2.6   Mechanics of Intermediate Filament Networks

2.6.1   Fundamentals of Rheology and Microrheology

To investigate whether the mechanical properties of individual filaments translate to the mechanical properties of filament networks, rheological measurements can be performed. Rheology describes the deformation and flow of a material in response to an applied stress. There are two limiting cases of materials that can be distinguished: simple solids which can store energy and provide a spring-like, elastic response, or simple liquids which are able to dissipate energy through viscous flow [4]. More complex fluids, like vimentin networks, show an intermediate behavior between solids and fluids [4, 86]. Rheometry measurements allow to obtain the bulk response and require large amounts in the milliliter range of material which can be difficult for most biological materials. To measure samples in the microliter volume range, and to obtain local measurements of inhomogeneous samples, microrheology measurements are performed. Small particles in the micrometer range are embedded within the network where they locally deform the sample. There are two main approaches to microrheological measurements: active and passive microrheology. Active microrheology describes the active manipulation of the network by applying external forces to the studied networks and passive microrheology measures the passive motion of the embedded particles within the network due to Brownian motion [4].

Active Microrheology

To actively manipulate the network, different approaches are used to apply external forces, such as magnetic or electric fields or forces created by an atomic force microscope [4]. The particles within the network are moved by an external force which results in a strain of the network that can be measured. With this method the network gets locally deformed and, therefore, a local viscoelastic response of the measured sample is obtained. An advantage of this method is the possibility to locally apply large strains which is useful for stiffer materials [4]. One possible implementation of microrheology are magnetic manipulation techniques such as magnetic tweezers. Strong magnetic fields induce a magnetic dipole in the super-paramagnetic beads and the magnetic field gradients are used to generate a force [4]. This method of magnetic tweezers has been used, for example, to probe the viscoelastic behavior of actin filament networks [87, 88]. Another implementation of active microrheology uses optical traps which allows to capture and manipulate dielectric particles
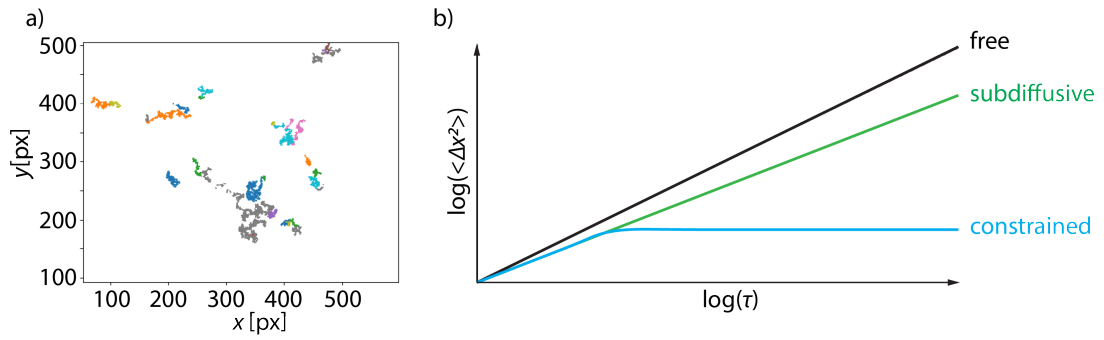
Figure 2.9: *Calculation of MSD's from bead traces. a) Individual traces of beads in water. b) Theoretical MSD curves at lag-times τ for free diffusion, shown in black, subdiffusive motion, shown in green, and constrained diffusion, shown in blue.*

with highly focused laser beams [70], as described in the previous section. With this method it was possible to measure, for example, the mechanical contribution of the IF vimentin to the cytoplasmic stiffness in mouse embryonic fibroblasts [89]. The third approach uses forces which are created by an atomic force microscope (AFM). This technique is sensitive to the required force which is needed to indent a surface and thereby measures the local elasticity and viscoelasticity of thin samples. For example, this method has been employed to study the effect of various drugs affecting the components of the cytoskeleton on the elasticity of fibroblasts [90].

Passive Microrheology

For passive microrheological measurements the Brownian motion of particles within the studied network is analyzed to investigate the rheological properties of the network [4, 91]. Therefore, the studied network has to be sufficiently soft such that the movement of the particles can be detected and analyzed. In a purely viscous medium like water, the particles undergo simple diffusion which is caused by Brownian motion of the particles. For micro particle tracking, individual particles are tracked using a video microscopy setup (see Fig. 2.9a) and from these traces the time dependent position correlation function, the so-called mean-square-displacement (MSD), is calculated by

$$\langle \Delta \vec{x}^2(\tau) \rangle = \langle |\vec{x}(t + \tau) - \vec{x}(t)|^2 \rangle, \tag{2.27}$$

with $\vec{x}$ being the vector of the particle position. The lag time τ describes the different time intervals that are analyzed and the displacement of the particle is averaged over all times t as shown in Fig. 2.9b, black line [4]. As we average over time, we assume

that the material properties do not change within the observed time range [4]. The
MSD for simple diffusion

$$\langle \Delta \vec{x}^2(\tau) \rangle = 2dD\tau, \tag{2.28}$$

gives us the diffusion coefficient D of the particle moving due to Brownian motion
observed in d dimensions [92]. The diffusion coefficient D of a particle is inversely
related to the frictional coefficient f of the particle scaled by the thermal energy

$$D = \frac{k_B T}{f}, \tag{2.29}$$

and f is calculated from Stokes' law

$$f = 6\pi \eta r, \tag{2.30}$$

with η denoting the viscosity of the fluid and r the radius of the particle [86]. Com-
bining these two equations leads to the Stokes-Einstein relationship [93]

$$D = \frac{k_B T}{6\pi \eta r}. \tag{2.31}$$

However, this diffusion coefficient is different for viscoelastic samples [4]. The motion
of the embedded particles reveals viscous and elastic contributions in the MSD curves
[4, 91] and the diffusion scales differently with τ according to

$$\langle \Delta \vec{x}^2(\tau) \rangle \sim \tau^\alpha, \tag{2.32}$$

with $\alpha < 1$ being the diffusive exponent [4]. For long time scales, this exponent
gives information about the particles which can either show subdiffusive motion for
$\alpha < 1$ (see Fig. 2.9b, green line) or they are locally constrained by the surrounding
network with $\alpha = 0$ (see Fig. 2.9b, blue line) [4]. For a homogeneous, elastic sample
the thermal motion of the particle depends on the stiffness of the micro environment
and equating the thermal energy density of a particle to the energy needed to deform
the sample yields

$$\frac{k_B T}{r^3} = \frac{G' L^2}{r^2}, \tag{2.33}$$

with the radius r of the particle, the elastic modulus G' of the sample and the defor-
mation length L [4]. For this purely elastic sample, the MSD shows a plateau when
the thermal energy density of the particle equals the elastic energy density of the

deformed network which leads to [4]

$$\langle \Delta \vec{x}^2 (\tau \to \infty) \rangle = \frac{k_B T}{\pi G' r}.$$ (2.34)

The elastic contribution from the deformation of the network can be described as the energy of a spring with a spring constant which is proportional to $G'r$ [4]. Hence, a viscoelastic network can be modeled as an elastic network viscously coupled to an incompressible fluid [4, 94]. To incorporate the elastic response, the standard Stokes-Einstein equation, eq. (2.31), can be generalized to rheologically complex networks with a complex shear modulus $G(\omega) = i\omega\eta$ which combines storage (real part) and loss (imaginary part) components [4, 94].

To be able to use the full potential of this method of passive microrheology, the MSDs of the embedded particles have to be measured with good temporal and spatial resolution. The MSDs of the embedded particles can be calculated by tracking the position of the particles. Here, the temporal resolution is determined by the frequency at which the particle position is recorded and the spatial resolution is determined by how precisely the differences in the position of the particles are measured [4]. When using a video-microscopy setup, the highest possible frequency is limited by the camera but an advantage of this method is that multiple particles can be recorded and tracked simultaneously. There are algorithms that are able to uniquely identify different particles in each frame and to find the center of each particle to locate the position of each particle and to correlate it with positions in later images to generate the traces [4, 95].

2.6.2   Rheology on Intermediate Filaments

The methods described in this previous section have also been used to study the properties of IF networks. The first rheological measurements on the IF vimentin revealed a striking difference compared to the other components of the cytoskeleton, namely actin and microtubules [96]. While rigid actin networks fluidize at high strains, vimentin networks are less rigid at low strains but stiffen at high strains and resist to breakage which has led to the assumption that the vimentin network maintains the cell integrity [96]. For several types of IFs, like vimentin, desmin, neurofilaments and keratin K8/K18, strain stiffening is observed [97–100] even though they differ in their linear and nonlinear viscoelastic properties [97]. Rheological measurements allow us

for instance, to derive the persistence length. The calculation of the persistence length showed for example, that desmin is stiffer compared to vimentin [97]. The mesh size and heterogeneity of reconstituted vimentin networks were measured with microrheology and it was obtained that at low concentrations Mg^{2+} ions act as cross-linkers between vimentin filaments with minimal changes to the structure of the network [101]. Also other divalent cations such as Ca^{2+} stiffen vimentin networks, further supporting their role as cross-linkers [98]. By truncating parts of the vimentin tail it could be shown that the last eleven amino acids of the tail domain are crucial in mediating the cross-links between vimentin filaments *via* divalent cations [98]. When higher concentrations of divalent ions are present, bundling of vimentin filaments can be observed, for example for Zn^{2+} [102]. Interestingly, the stiffness of IF networks increases with increasing divalent cation concentration until a concentration is reached at which bundling occurs which then leads to softening of the network [102]. Another important parameter to consider during network formation is the temporal evolution of the IF network. Over time, vimentin networks stiffen which can be linked to an increase in filament length [103]. However, reduction of the hydrophobic or an increase in electrostatic interactions in between vimentin filaments leads to slower filament elongation and therefore to delayed network formations [103]. This strengthens the importance of various conditions that have an impact on filament network mechanics: elongation kinetics as well as filament-filament interactions [103]. Despite all the research done on mechanics of IFs, they are not as extensively studied compared to actin and microtubules which are the other two components of the cytoskeleton and various aspects still remain unclear.

3

Material and Methods

Parts of this chapter have been published in parts or completely in the material and methods sections of [55] and [104]. Every protocol has been performed by myself unless stated otherwise.

3.1 Protein Purification

This section is published in parts in Ref. [104].

All vimentin variants were expressed recombinantly in *E. coli*. The purification of human vimentin with the mutation C328A and additional amino acids glycine-glycine-cysteine at the C-terminus from *E. coli* based on Herrmann *et al.* [16] was performed according to Ref. [50]. The additional amino acids were included to enable binding of the vimentin filaments to maleimide-functionalized beads and for fluorescent labeling of the monomers. Removing the cysteine from the rod domain of the protein enables assembly even after labeling [105]. Two phosphomimetic mutants, S38E and S72E, as well as control mutants S38A and S72A of vimentin C328A were produced according to the same protocol. The protein was stored in 8 M urea (Carl-Roth GmbH, Karlsruhe, Germany), 5 mM Tris(hydroxymethyl) aminomethane (Tris; Carl-Roth GmbH), 1 mM ethylenediaminetetraacetic acid (EDTA; Carl-Roth GmbH),

0.1 mM ethylene glycol bis(β-aminoethyl)-ether N,N,N',N' tetra- acetic acid (EGTA; Carl-Roth GmbH) and adjusted to a pH of 7.5 with hydrochloric acid (HCl; Carl-Roth GmbH).

3.2   Protein Labeling

To enable visualization of the filaments during the optical trapping experiments, vimentin was fluorescently labeled with ATTO647N (ATTO-TEC GmbH, Siegen, Germany) or ATTO488(ATTO-TEC) via maleimide chemistry according to the protocol published in Ref. [49]. For the labeling, 1 mL of vimentin in storage buffer is pipetted into a dialysis tubing with a 50 kDa cutoff (Th. Geyer Ingredients GmbH & Co. KG, Höxter, Germany) and dialyzed against *labeling buffer* over night. To prepare this buffer, a solution A of 5 M urea and 50 mM NaH_2PO_4 (Carl-Roth GmbH) in 750 mL distilled water and a solution B of 5 M urea and 50 mM Na_2HPO_4 (Carl-Roth GmbH) in 750 mL distilled water were prepared. Solution A and B were mixed until a pH of 7.0 was reached. Next, the protein was adjusted to a concentration of 1.0 mg/mL and mixed with 20 µL of the corresponding dye at a concentration of 10 mM dissolved in dimethyl sulfoxid (DMSO; Carl-Roth GmbH) in 5 µL steps with 5 min incubation time in between. The vimentin solution is incubated for 2 h at room temperature protected from light. In order to bind unbound and free dye molecules, 100 µL of a 1 M L-cysteine (Carl-Roth GmbH) solution was added to the vimentin solution and incubated for 1 h at room temperature protected from light. To separate the free dye from the labeled protein, size exclusion chromatography (Bio-Gel P-30, Bio-Rad Laboratories GmbH, Feldkirchen, Germany) with a 27 mL column was performed. The protein was washed through the column by adding labeling buffer and the protein concentration was measured by using a NanoDrop (Thermo Fisher Scientific, Kandel, Germany). The samples with the highest amount of label were pooled and dialyzed in a dialysis tubing against *storage buffer* (8 M urea, 50 mM Tris-HCl, pH 8.4) over night. The labeled protein was stored at -80°C. With this labeling procedure, the cysteine at the tail domain of vimentin is labeled and thereby the effect on the hierarchical structure of vimentin is minimized.

3.3   Filament Assembly

In order to remove the urea from the storage buffer and to be able to assemble filaments, a stepwise dialysis was performed. Depending on the experiment, different buffers were used for the stepwise dialysis: either a 2 mM phosphate buffer (PB) at pH 7.5 or a 5 mM Tris-HCl buffer (TB) at pH 8.4.

For the experiments in PB the *urea buffer* consists of a solution A of 6 M urea in 2 mM NaH_2PO_4 (Carl-Roth GmbH) and a solution B of 6 M urea in 2 mM Na_2HPO_4 (Carl-Roth GmbH). Solution A and B were mixed until pH 7.5 was reached. The *dialysis buffer* consists of 50 mL 20 mM NaH_2PO_4 and 150 mL 20 mM Na_2HPO_4, in 2 L milliQ water.

For experiments in TB the *urea buffer* consists of 6 M urea with 5 mM Tris in 0.5 L milliQ water and set to pH 8.4 by titration with HCl. The *dialysis buffer* consists of 5 mM Tris in 2 L milliQ water and set to pH 8.4 with HCl.

To prepare the protein for filament assembly, 200 µL unlabeled vimentin at a concentration of 1.3 mg/mL was mixed with 25 µL ATTO647N-labeled vimentin at a concentration of 0.4 mg/mL resulting in a labeling ratio of 4 %, and dialyzed using dialysis tubing with a 50 kDa cutoff from storage buffer against the corresponding *urea buffer*. Then another dialysis in a stepwise manner (4 M, 2 M, 1 M, 0 M urea, 30 min for each step) against the corresponding *dialysis buffer* with a subsequent dialysis step against fresh *dialysis buffer*, over night. Afterwards the protein concentration was adjusted with *dialysis buffer* to about 0.2 mg/mL by using a NanoDrop. It has been shown that the protein does not change its conformation within 7 days [106] and thus can be kept in the fridge for this amount of time, protected from light.

The *assembly buffer* contains either 7.5 mL of 1 M KCl, 20 mM NaH_2PO_4 and 42.5 mL of 1 M KCl, 20 mM Na_2HPO_4 in 450 mL of milliQ water with a final pH of 7.5 for assembly in PB or 500 mL of 25 mM Tris-HCl, 50 mM sodium chloride (NaCl; Carl-Roth GmbH) with a pH of 7.5 for assembly in TB. To initiate filament assembly, 200 mL protein was dialyzed against the corresponding *assembly buffer* at 37°C over night [107]. Afterwards the protein was transferred into reaction tubes and stored in the fridge until use. The assembled protein can be stored for up to 2 days.

3.4   Maleimide Bead Functionalization

The beads used for trapping experiments were functionalized with maleimide according to Ref. [108]. Carboxylated polysterene beads (PPs-4.2 COOH 4.0 µm to 4.4 µm,

5%(w,v); Kisker Biotech GmbH & Co. KG, Steinfurt, Germany) were agitated on a shaker at 40 rpm for 30 min to avoid colloidal aggregates. 100 µL of the stock solution with a bead concentration of 5 % were transferred into a 1.5 mL reaction tube and were spun down until a speed of 10.000 rcf (MiniSpin F-45-12-11, Eppendorf, Wesseling-Berzdorf, Germany) was reached. The supernatant was discarded and the beads were washed twice with 1 mL 100 mM 2-(N-Morpholino)ethanesulfonic acid sodium salt (MES; Sigma-Aldrich) buffer for 10 min each. In-between the washing steps, the beads were centrifuged down and the supernatant was discarded.

For the functionalization, beads were transferred in 100 µL 100 mM MES buffer mixed with 100 µL 100 mM MES buffer containing 8 mg NH_2-PEG-maleimide (Nanocs, New York, NY, USA), 16 mg NH_2-PEG-OH (Iris-Biotech, Marktredwitz, Germany) and 40 mg 1-Ethyl-3-(3-dimethyl aminopropyl)carboxiimide) (EDC; Sigma-Aldrich). This mixture was mixed thoroughly for 2 min with a vortex mixer (Scientific Industries SI™Vortex-Genie™2, Fisher Scientific GmbH, Schwerte, Germany) and sonicated for 2 h in 20 min intervals with mixing steps for 30 s in between.

The beads were washed three times with 1 mL phosphate buffered saline (PBS; Invitrogen AG, Carlsbad, CA, USA) containting 2% bovine serum albumin (BSA; Sigma-Aldrich) for 10 min. In between, beads were centrifuged down and the supernatant was discarded. For storage the functionalized beads were resuspended in 1 mL PBS containing 2% BSA and kept at 4°C.

3.5 Vimentin Phosphorylation

3.5.1 Vimentin Phosphorylation with Protein-Kinase A

This section is published in parts in Ref. [104].

For the *phosphorylation buffer* we used 25 mM Tris-HCl, pH 7.5 containing 50 mM NaCl, 2 mM magnesium dichloride ($MgCl_2$; Sigma-Aldrich) and added 100 µmol adenosine triphosphate (ATP; Carl Roth), and protein kinase A (PKA; New England Biolabs, Frankfurt am Main, Germany). The amount of PKA was adjusted according to the amount of vimentin used, with 1 µL PKA solution per 1 µg vimentin. Vimentin solution and *phosphorylation buffer* were mixed at a ratio of 1:9 resulting in a final vimentin concentration of 0.11 mg/mL. This mixture was incubated for about 1 h at 37°C and dialyzed into 8 M urea in 5 mM Tris-HCl, pH 8.4 for about 1 h at room temperature. This step was performed to stop the phosphorylation by inactivation of the PKA. In a next step the phosphorylated vimentin was mixed at the desired ratios

with unphosphorylated vimentin, which was diluted to the same concentration by adding 8 M urea in 5 mM Tris-HCl, pH 8.4. This vimentin mixture was then dialyzed as described before from 8 M urea in 5 mM Tris-HCl, pH 8.4 in steps of 4 M, 2 M, 1 M and 0 M urea to 5 mM Tris-HCl, pH 8.4 and afterwards assembled in 25 mM Tris-HCl, pH 7.5 and 50 mM NaCl at 37°C over night.

3.5.2 Verification of the Phosphorylation

This section is published in Ref. [104].

To test whether the phosphorylation of vimentin tetramers was successful, phosphorylation analysis gels (Phos-tag™Acrylamide AAL-107, FUJIFILM Wako Chemicals Europe GmbH, Neuss, Germany) were used. These gels show additional bands above the actual protein band if the protein is phosphorylated successfully. The phosphorylation analysis sodium dodecyl sulphate (SDS) gels were produced according to the manufacturer's instructions. Samples were prepared by mixing 13 µL protein with 7 µL sample buffer (150 µL Laemmli SDS sample buffer (Alfa Aesar, Kandel, Germany), 60 µL 1 M dithiothreitol (DTT; Carl-Roth GmbH)), followed by an incubation at 95°C for 5 min. The gel was loaded with 15 µL of each sample and run at a constant current of 40 mA for about 35 min. Afterwards the gel was stained (InstantBlue, Sigma-Aldrich) for 1 h followed by several washing steps with water. To check the incorporation of the phosphorylated monomers within the filament, ultra-centrifugation was performed. The partially phosphorylated vimentin filaments were centrifuged at 34,000 rpm for 10 min (rotor: Fiberlite F50L-25x1.5; centrifuge: Sorvall WX80+ Ultra Series centrifuge, Thermo Fisher Scientific). The supernatant was removed and mixed with sample buffer as described above. The pellet was dissolved in 8 M urea, 5 mM Tris-HCl, pH 8.4, with subsequent dialysis (8 M, 4 M, 2 M, 1 M, 0 M urea in 5 mM Tris-HCl, pH 8.4). Afterwards the dissolved pellet was mixed with sample buffer followed by an incubation at 95°C for 5 min for all samples. The samples were then loaded on an SDS gel and it was run and stained as described above.

3.6   Vimentin Binding to the Protein 14–3–3

3.6.1   Binding Process

This section is published in parts in Ref. [104].

The protein 14–3–3 was purified and kindly provided by Julia Menzel (Department of Molecular Biology, University Medical Center Göttingen, Göttingen, Germany). The full protocol can be found in Appendix A.2.1.

To bind the protein 14–3–3 to vimentin it was first diluted to the same concentration determined in mg/mL as the vimentin solution. Then, 14–3–3 and assembled vimentin filaments were mixed at a ratio of 1:1 with respect to the concentration in mg/mL and incubated for 1 h at 37°C. For the optical trap measurements, 30 µL of this solution were diluted in 1 mL assembly buffer (25 mM Tris-HCl, pH 7.5 and 50 mM NaCl).

3.6.2   Verification of the Binding

This section is published in Ref. [104].

To test whether the binding of 14–3–3 to vimentin was successful, a streptavidin pulldown assay was performed (adapted from Ref. [109]). Unless otherwise stated, a centrifugation speed of $200 \times g$ for 30 s was used. First 200 µL biotin-labeled vimentin (labeling with biotin-maleimide (Jena BioSciences GmbH, Jena, Germany) was mixed according to the protocol described in Ref. [49]), dialyzed to tetramers and phosphorylated as described above. This biotin labeling of vimentin is necessary for the binding to the beads. The streptavidin-agarose beads (Sigma Aldrich) were washed. To do so, 70 µL beads (for 1 µg of vimentin) were pipetted into a reaction tube (1.5 mL) and washed three times with phosphorylation buffer (25 mM Tris-HCl, pH 7.5 containing 50 mM NaCl, 2 mM MgCl$_2$). In between the washing steps the beads were centrifuged down for 30 s at 1,700 rpm (MiniSpin F-45-12-11, Eppendorf) and the supernatant was discarded. Vimentin was diluted with phosphorylation buffer to a concentration of 0.02 mg/mL and then 50 µL of vimentin solution (total protein amount of 1 µg) was mixed with the beads in the reaction tube. The solution was incubated for 1 h at 8°C on a rotation wheel. During this time, vimentin bound to the beads due to the biotin-streptavidin binding. In order to remove the unbound vimentin, this mixture was pipetted on a column (35 μm pore size, MoBiTec GmbH, Göttingen, Germany), centrifuged down and the flow-through was kept for later analysis. The bead mixture was then again washed twice with phosphorylation buffer

and the flow-through was kept. Afterwards, 14–3–3 was diluted to 0.02 mg/mL in phosphorylation buffer containing 0.01 % Triton X-100 (Carl-Roth GmbH) and 50 μL was mixed with the beads to which vimentin was bound. This mixture of beads and 14–3–3 was incubated for 1 h at 8°C on a rotation wheel so the 14–3–3 bound to the vimentin on the beads. To remove the unbound 14–3–3, the mixture was centrifuged down, and the flow through was kept for later analysis. The bead mixture was then washed twice with phosphorylation buffer. To remove the bound vimentin and 14–3–3, eluation buffer was used. The eluation buffer consisted of 90 μL SDS loading buffer, 10 μL fresh DTT and 5 μL 100 mM biotin (Jena Bioscience GmbH, Jena, Germany) which was mixed and incubated for 10-15 min at 95°C. This eluation buffer was added to the beads, mixed well and incubated for 7 min at 70°C. In the next step the mixture was centrifuged down and the flow through was kept as it should contain the vimentin which bound to the beads and the 14–3–3 which bound to the vimentin. As a last step all the flow through samples were mixed with sample buffer and a phosphorylation analysis SDS gel was run as described above.

3.7 Mass Spectrometry Analysis

Different methods for mass spectrometry experiments were performed to investigate the effect of phosphorylation on vimentin at the level of the amino acid sequence. The experiments to obtain the exact position of phosphorylation were performed by Ivan Silbern (Bioanalytical Mass Spectrometry, Max Planck Institute for Biophysical Chemistry, Göttingen, Germany) and a detailed description of the experiment and analysis can be found in Chapter 5 and in Appendix A.2.1. Quantitative cross-linking experiments were performed by Iwan Parfentev (Bioanalytical Mass Spectrometry, Max Planck Institute for Biophysical Chemistry, Göttingen, Germany) and the detailed description can be found in Chapter 5 and in Appendix A.2.1.

3.8 Optical Trap Measurements

For all measurements, a commercial optical trap setup (C-trap, Lumicks, the Netherlands) which combines optical traps with a microfluidic chip and a confocal microscope was used. Two different experiments were conducted at the optical trap, which will both be shortly described in the following.

3.8.1   Cyclic Loading Experiments

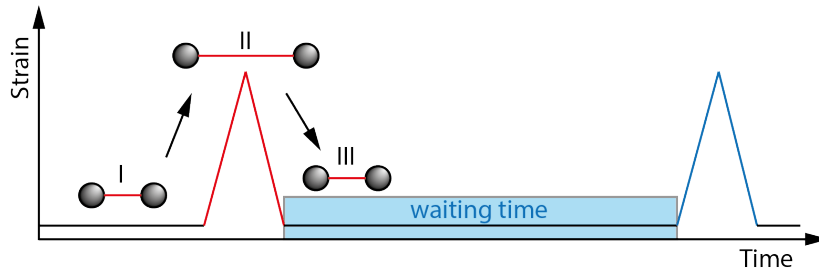This subsection is published in Ref. [55] and [104].

Figure 3.1: *The first cycle, depicted in red, is divided in three parts (I-III). In the first part the vimentin filament is in a relaxed state. In the second part the bead distance is increased and thus the filament is stretched and the strain of the filament increased. By reducing the bead distance the filament is relaxed again (part III). The filament is kept attached to the beads during the waiting time and subsequently stretched again in a second cycle, here depicted in blue.*

Cyclic loading experiments, as depicted in Fig. 3.1 were performed in order to investigate the mechanical recovery behavior of stretched vimentin filaments. In short, a fresh pair of beads was captured for each experiment in the bead channel (Fig. 3.2, channel 1).

A vimentin filament was captured in the vimentin channel (Fig. 3.2, channel 2) and bound to the second bead in the buffer channel (Fig. 3.2, channel 3), containing the PB *assembly buffer*. Parts of the measurements were performed with filaments bound to the beads by maleimide-chemistry and parts of the experiments with filaments bound via biotin-streptavidin. The covalent attachment of the filaments via maleimide-groups enables us to introduce waiting times between the filament stretching cycles. For cross-linking experiments, the captured vimentin filament was moved to channel 4 (Fig. 3.2) filled with buffer containing either paraformaldehyde (PFA; Sigma-Aldrich) (0.12 % (v/v)) or glutaraldehyde (GA; Polysciences Europe GmbH, Hirschberg an der Bergstrasse, Germany) (0.5 % (v/v)). Before a force-distance curve was recorded, the filaments were always moved back to the channel that only contained buffer (Fig. 3.2, channel 3). Additionally, a prestrain of 5 pN was imposed for all recovery experiments. This prestrain prevents the filaments from wrapping around the beads during the waiting time as well as the loss of the filament during that time. Before the actual measurement, this value was set to 0 pN and this prestrained length of the filament was used as initial length L_0 to calculate the dimensionless strain during stretching. Following the measurement protocol sketched in Fig. 3.1, the filament was stretched beyond the linear regime into the
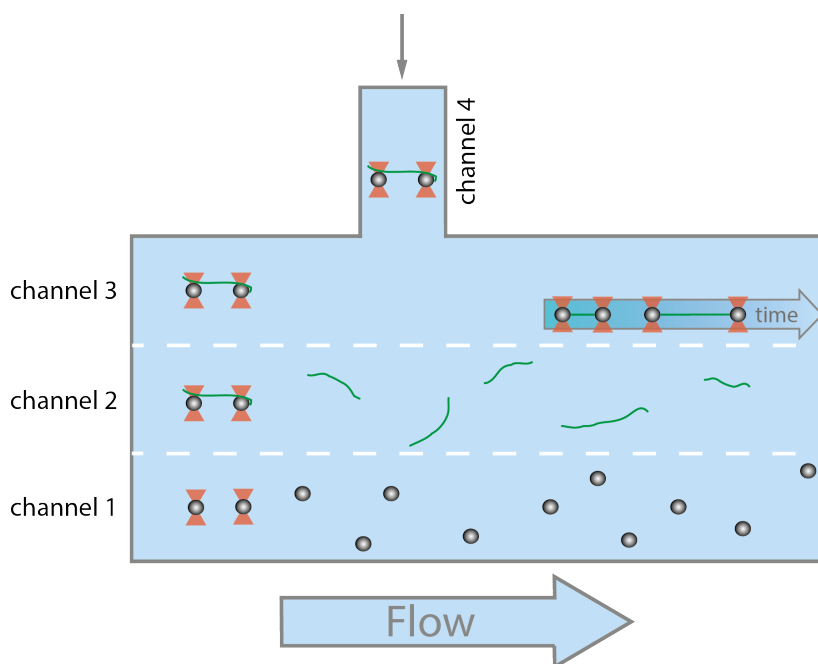
Figure 3.2: *The microfluidic chip contains three main channels (channel 1-3) which are separated by laminar flow. Channel 1 contains the beads, channel 2 contains vimentin filaments and channel 3 is filled with the PB assembly buffer. The additional channel, channel 4, can be used with a different buffer to change the conditions.*

characteristic plateau region, where unfolding of the α-helices occurs. Subsequently, the filament was relaxed and, after a defined time $t_{\text{wait}} \leq 1\,\text{h}$, stretched again to the same trap position as in cycle one. The length of the filament and the applied force were recorded over the full experiment.

3.8.2   Phosphorylation Experiments

The preparation of the stretching measurements for phosphorylated vimentin filaments was conducted as described in the previous section, but the arrangement of the channels was slightly different, see Fig. 3.3. For each measurement a fresh pair of beads was captured in the bead channel (see Fig. 3.3). The beads were moved to the buffer channel (TB *assembly buffer*) for calibration. Afterwards, they were moved to the vimentin channel (vimentin filaments in TB *assembly buffer*), while scanning with the confocal microscope, until a single vimentin filament was captured on one bead. Then the beads were moved back to the buffer channel where the filament was attached to the second bead. In contrast to the cyclic loading experiments we ensured that the filament was relaxed to avoid prestrain. The measurements were performed by moving one bead with a constant speed of about $0.7\,\text{µm/s}$ to stretch the filament
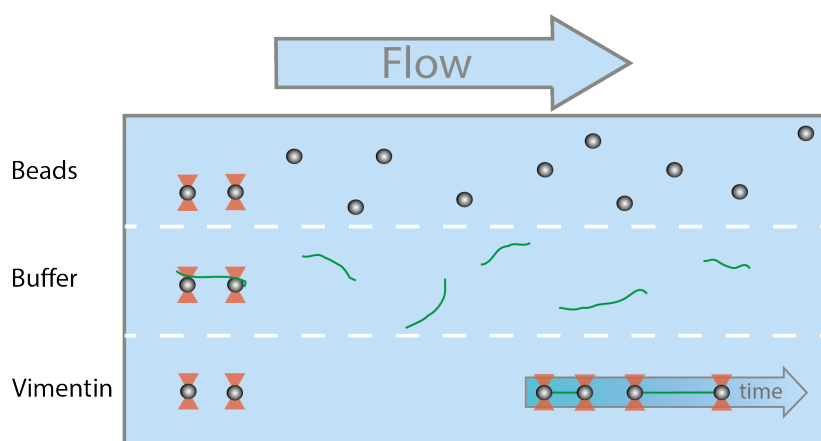
Figure 3.3: *Schematic overview of the experimental setup with the microfluidic chip within the optical trap. The different compartments are realized by laminar flow and the filaments are measured in the buffer region. All compartments have different functions. In the beads channel, a pair of beads is captured, the buffer channel is used for calibration and the actual measurement and the vimentin channel is used to capture a single vimentin filament.*

until it ruptured or the force on the second bead were higher than 700 pN. During the stretching, force-distance curves were recorded.

3.9   Small-Angle X-Ray Scattering Experiments

These experiments were performed together with Manuela Denz (Institute for X-Ray Physics, University of Göttingen, Göttingen, Germany). The protein preparation was conducted by myself and Manuela Denz performed the small-angle X-Ray scattering (SAXS) experiments and the data analysis described in more detail in Appendix A.2.1.

3.9.1   Sample Preparation

In general, the protocol for the protein dialysis and phosphorylation were the same as described above. All experiments were performed in TB. The vimentin concentration before the dialysis was 4.5 mg/mL. In order to maintain a high vimentin concentration, the phosphorylation protocol was adapted as follows: the *phosphorylation buffer* contained 70 mM Tris-HCl, 150 mM NaCl, 6 mM $MgCl_2$ at a pH of 7.5 and for the phosphorylation 25 µL dialyzed vimentin was mixed with 12.5 µL *phosphorylation buffer*, 1 µL ATP and 67.5 µL PKA. After that step the initial protocol from above was followed. For the assembly a so-called *kick-start buffer* was used as the assem-

bled protein was too viscous to be inserted properly into the capillaries afterwards. With this method, the assembly is not started slowly via dialysis but the protein is directly mixed with the buffer which starts the assembly process rapidly. The *kick-start buffer* contained 45 mM Tris-Hcl, 100 mM NaCl at a pH of 7.5. The *kick-start buffer* is mixed 1:1 with the vimentin protein with different phosphorylation ratios, namely 0%, 1%, 5% and 10% phosphorylation, and pipetted into glass capillaries. The assembly was performed in 1.5 mm diameter quartz glass capillaries, wall thickness 0.01 mm (Hilgenberg GmbH, Malsfeld, Germany) for 4 h at 37 °C in a temperature controlled water bath. Directly after filling of the capillaries, they were sealed with wax (Hampton Research, Aliso Viejo, CA, USA).

3.10   Data Analysis

3.10.1   Cyclic Loading Experiments

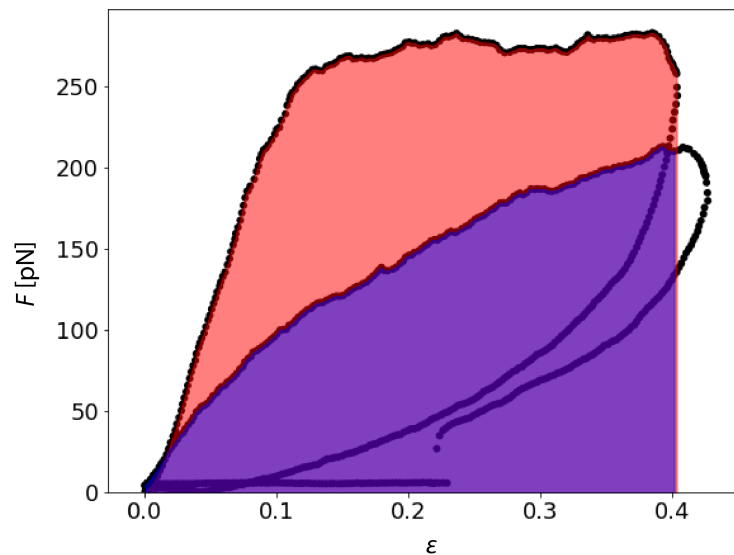This subsection is published in parts in Ref. [55].

Figure 3.4: *The energy needed to stretch the filament in the first cycle is calculated by integration of the area underneath the curve up to the maximum strain depicted in red. The energy needed to stretch the filament a second time, up to the maximum of the first cycle, is depicted in blue.*

All data were converted to ASCII format with the measuring software (TWOM, Lumicks) and the rest of the analysis were analyzed with self-written Python scripts.

The bead diameter was subtracted from the distance and the time and force data were used as measured. The calibration of the optical trap was performed by analysis of the power spectral density of the thermal fluctuations of the trapped beads in the buffer channel. To calculate the energy for the first cycle, the area beneath the stretching curve up to the maximum strain was calculated by integration, see Fig. 3.4 (red area). The curve was smoothed with a Savyzki-Golay filter of second order and a window size of 9. This step was performed to reduce errors due to fluctuations. The maximum strain value was defined as the inflection point of the curve. The integral was calculated according to the trapezoidal rule. As we can only control the position of the trap and not the position of the bead, the maximum strain of the second stretching cycle is slightly higher than the maximum strain for the first stretching cycle, due to the softening of the filament. To compare the input energy that was needed to strain the filament to the same length again, the energy needed for the second stretching was calculated by integrating the area beneath the second stretching curve but only up to the maximum strain of the first stretching curve as depicted in Fig. 3.4 (blue area). The two energy values were then divided to obtain the input energy ratio. Further analysis have been performed by Johanna Forsting (Institute for X-Ray Physics, University of Göttingen) together with Hannes Witt (Institute for Physical Chemistry, University of Göttingen) as described in further detail in Chapter 4 and in Appendix A.1.

3.10.2   Phosphorylation Experiments

This subsection is published in parts in Ref. [104].

All data were saved as hdf5 files. The measurements were performed by moving one bead at about 0.7 μm/s to stretch the filament until it ruptured or the forces on the second bead were so high that the bead was pulled out of the trap. During the stretching, force-distance curves were recorded.

Data were analyzed with self-written Python scripts. The calculation of the mean curves for each condition was adapted from Ref. [51]. For the averaging of the curves of one data set, the force data were interpolated to the same number, 200, of data points. The maximum strain of the averaged curve was calculated by the average of the individual maximum strain values. Thereby, the strain data consists of 200 equally distributed points up to the average maximum strain. Then, the force values of all individual curves were averaged for each of the strain values to gain an average force-strain curve. For the calculation of the Young's modulus, a linear fit up to a

force of 130 pN was performed for the initial slope in the linear regime of the mean force-strain curves. The Young's modulus was calculated *via* the ratio of stress and strain, $Y = \frac{\sigma}{\varepsilon} = \frac{F/\pi R^2}{\varepsilon}$. For the radius R the corresponding radius of gyration of the cross-section defined by small-angle X-Ray scattering was used.

3.11 Microrheology

3.11.1 Bead Coating

The beads used for the microrheology experiments were coated with poly(ethylene glycol and poly-L-Lysine)-PEG (PLL-g-PEG; Susos AG, Dübendorf, Switzerland) to inhibit interactions between beads and vimentin filaments. To wash the beads, 20 µL of 1.9 µm beads was diluted in 1 mL of TB *dialysis buffer* (5 mM Tris-HCl, pH 8.4) and mixed briefly with a vortex mixer. They were centrifuged for 75 s at 12.4×10^3 rpm (MiniSpin F-45-12-11, Eppendorf). The supernatant was discarded and 1 mL of fresh TB *dialysis buffer* was added to the beads. Like this, the beads were washed three times in total. Then 50 µL of PLL-PEG at a concentration of 1 mg/mL were diluted in 500 µL TB *dialysis buffer*. The PLL-PEG solution was added to the bead pellet and briefly mixed with a vortex mixer. They were covered from light and agitated on a shaker at 40 rpm over night. The next day the beads were washed three times with TB *dialysis buffer* as described above. Finally, 150 µL of 10x TB *assembly buffer* (245 mM Tris-HCl, 500 mM NaCl, pH 7.3) was added to the bead pellet and stored in the fridge until use.

3.11.2 Microrheology measurement

To assemble the measuring chamber, glass slides were first cleaned. The glass slides were placed in isopropanol and then placed in an ultrasonic bath for 15 min. Afterwards they were dried with a nitrogen gun and stored away from dust until used. For one measuring chamber, one silicone isolator (Press-to-Seal silicone isolater, 9 mm diameter, 0.5 mm deep; Thermo Fisher Scientific) was glued to one cleaned glass slide. The edges of the silicone isolator were covered with vacuum grease to prevent the liquid from evaporating. Then 40.5 µL of vimentin solution at a concentration of 1.05 mg/mL was mixed with 4.5 µL of the bead solution and 45 µL were pipetted into the chamber, which corresponds to assembly *via* the kick-start method described above. The chamber was closed with a smaller glass slide on top of the silicone

isolator. The finished chamber was mounted on a rotation wheel and it was rotated at low speed until the measurement was performed. This prevents the beads from sinking down to the bottom of the chamber. Measurements were usually taken after 6 h, 24 h and 72 h. A chamber was placed on the microscope with a 60x water immersion objective (UPLSAPO60XW, 1.2 NA, Olympus, Hamburg, Germany) and focused 30 μm from the bottom of the chamber. Then a series of brightfield images was taken with a camera (PCO.edge 5.5, PCO AG, Kelheim, Germany) at 139 fps for a total of 70,000 images. The raw file was saved and later on converted to tif files with the PCO software. Each sample was measured at two or three positions to increase the number of tracked particles. For the microparticle tracking, the Python software *trackpy* was used, which is based on the algorithm of Crocker *et al.* [95]. To track the particles, bright spots were chosen as the center of the bead appears very bright and therefore only high masses, *i.e.* masses greater than the first high peak as shown in Fig. 3.5a, were chosen. This gives us a list of initial tracks. Next, the size
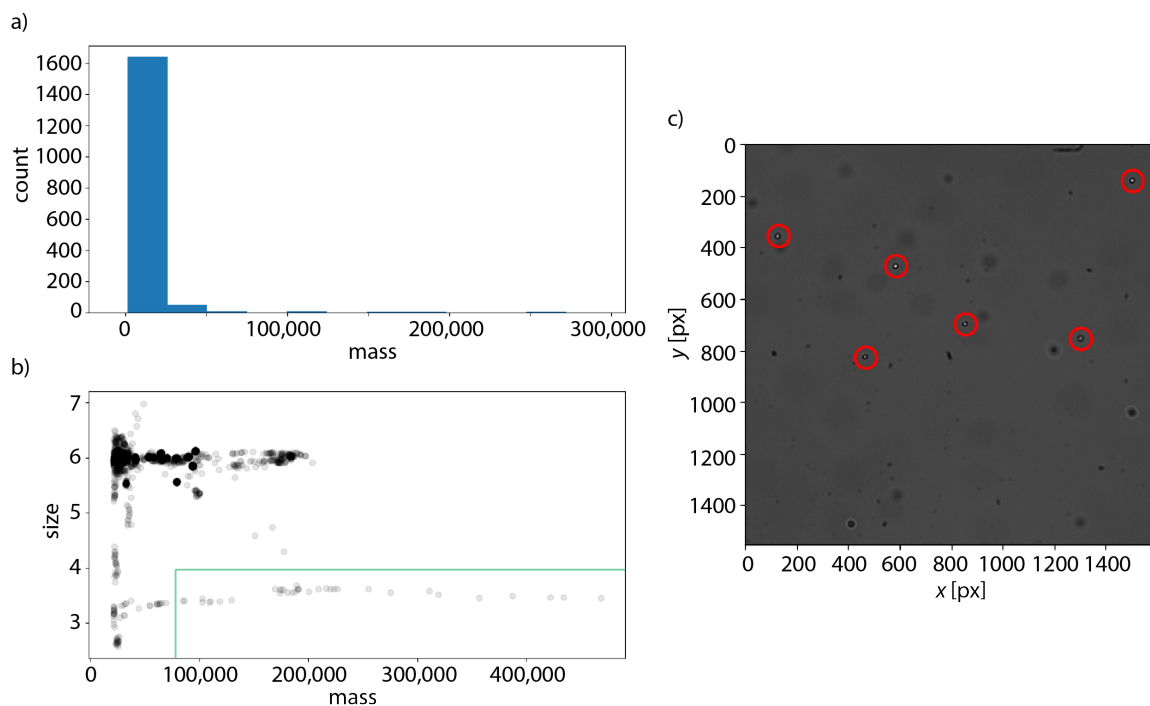

Figure 3.5: *Bead tracking. a) Histogram of particle masses. b) Mass versus size plot of the individual tracked particles. A large mass corresponds to the brightest spots which is the center of the beads. A small size is chosen to avoid tracking clusters of beads. The final chosen particles are within the green rectangle. c) Brightfield image with the final choice of beads marked by a red circle.*

over mass for the initial tracks is plotted. Here, we chose again the particles with the highest mass as this corresponds to the brightest spots and therefore the center of the particles. Further, a small size is chosen to avoid tracking clusters of beads. An

example of the final choice of parameters is shown in Fig. 3.5b indicated by the green rectangle. This step has to be done individually for each data set as the parameters vary slightly. This sorted set of tracks is then stored in a new list of tracks. To check whether the selection was right, the brightfield image with the chosen particles is plotted, as shown in Fig. 3.5c marked by the red circles. The individual trajectories were plotted and it was checked by eye whether drift can be observed. If so, the drift correction function of *trackpy* was used. Next, the individual MSDs and the median MSD of one data set are plotted with the corresponding functions in *trackpy*.

4

Vimentin Intermediate Filaments During Cyclic Loading

To investigate the response of individual vimentin filaments to mechanical stress, we perform repeated stretching cycles. In the first part, we investigate the recovery behavior of vimentin filaments after being stretched and relaxed again. In the second part, we perform experiments to study the influence of different loading rates on the recovery behavior. In the last part we investigate the involvement of the elastic stretching regime of vimentin during multiple stretching cycles.

4.1 Vimentin Intermediate Filaments Undergo Irreversible Conformational Changes during Cyclic Loading

Johanna Forsting[1]*, Julia Kraxner[1]*, Hannes Witt[2]*, Andreas Janshoff[3], Sarah Köster[1]

[1] Institute for X-Ray Physics, University of Goettingen, 37077 Göttingen, Germany.
[2] Max Planck Institute for Dynamics and Self-Organization, 37077 Göttingen, Germany.
[3] Institute of Physical Chemistry, University of Goettingen, 37077 Göttingen, Germany.
* Equal contribution

Contribution to this article: SK conceived the project. JF and JK each performed parts of the experiments and the data analysis. HW performed parts of the data analysis, developed and implemented the models and performed all simulations. AJ and SK supervised the project. All authors wrote the manuscript.

4.1.1 Abstract

Intermediate filaments (IFs) are part of the cytoskeleton of eukaryotic cells and are thus largely responsible for the cell's mechanical properties. IFs are characterized by a pronounced extensibility and remarkable resilience that enable them to support cells in extreme situations. Previous experiments showed that under strain, α helices in vimentin IFs might unfold to β sheets. Upon repeated stretching, the filaments soften, however, the remaining plastic strain is negligible. Here we observe that vimentin IFs do not recover their original stiffness on reasonable time scales, and we explain these seemingly contradicting results by introducing a third, less well-defined conformational state. Reversibility on the nanoscale can be fully rescued by

introducing cross-linkers that prevent transition to the β sheet. Our results classify IFs as a nanomaterial with intriguing mechanical properties, which is likely to play a major role for the cell's local adaption to external stimuli.

4.1.2 Introduction

The mechanical properties of biological cells are defined by the cytoskeleton, a composite network of microtubules, actin filaments and intermediate filaments (IF) [110, 111]. Although the exact division of labour among the three filament types is still not fully resolved [110, 111], there is ample evidence that IFs are the load bearing elements when cells are subjected to external tensile [112, 113] or compressive [114] stress. During embryogenesis and tissue formation, in particular, cells undergo dramatic changes in shape and size. The force scales expected for cellular processes lie between single motor protein forces of a few pN, which can be measured by FRET sensors, [115] and the collective forces of several nN measured for whole cells, as determined, e.g., by traction force microscopy [116]. In order to withstand strong transitions, cells show reversible superelasticity, which is linked to their IF network [112]. In order to achieve the required material properties for IFs, nature applies design principles on the nanoscale distinct from human engineering solutions and instead relies on self-organization and structural hierarchy. As a consequence, IFs stand out among the cytoskeletal filaments by their high flexibility [117, 118] and enormous extensibility [44, 45, 49, 50].

Within the IF family, vimentin is typical for cells of mesenchymal origin [18]. Like all cytoskeletal IFs, vimentin monomers comprise an α-helical rod domain with intrinsically unstructured head and tail domains [9]. The monomers assemble following a hierarchical pathway resulting in filaments with laterally and longitudinally arranged monomers (Fig. 4.1a) [12, 119]. Theoretical considerations [49, 50], molecular dynamics simulations [47, 54] and X-ray diffraction studies [48] have shown that the intriguing tensile properties of IFs originate from conformational changes on different levels of the hierarchical filament structure. Upon stretching, the α-helical parts of the vimentin monomers and, as a consequence, also the dimeric coiled coils unfold, leading to an elongation of the filament. There is evidence from studies on vimentin and other IFs that the unfolded strands at least partly form β sheets [47, 48, 54].

As the measured forces during relaxation of the filament are greater than zero and we previously observed only little plastic deformation upon stretching and relaxing

[50], it was concluded that this conformational change is reversible and that relaxed vimentin IFs eventually return to the α-helical state [50]. In the same study it was observed that, when repeatedly stretched, vimentin IFs become softer with every cycle, indicated by a decrease of the slope in the force-strain curve (Fig. 4.1b) [50]. Monte Carlo simulations suggest that this behavior is due to the presence of mixed conformational states of parallel monomers [50]: Fewer and fewer α-helical monomers survive, rendering the filament softer. These observations raise the question if and on which time scales a complete recovery of the initial mechanical properties, connected to refolding into α helices, occurs.

Here, we find that, surprisingly, the initial tensile behavior cannot be recovered on reasonable time scales suggesting that this reversibility on the nanoscale is not achieved, although the filaments show negligible excess strain after relaxation. However, cross-linking of the filaments leads to a restoration of the initial tensile behavior. We present an attempt to disentangle the seemingly contradicting results towards a comprehensive understanding of the intricate mechanical behavior of IFs. We propose a consistent mechanistic model for the observed phenomena that requires to include a third, disordered, conformational state, and postulate that the native system cannot return to the α helix, which becomes less populated with each loading cycle.

4.1.3   Results

In order to examine the mechanical recovery after stretching of vimentin filaments we perform a straight-forward optical trapping experiment: Between two stretching cycles the filament is kept at its initial contour length for a varying time t_{wait} (Fig. 4.1c). By this procedure, conformational changes caused by straining the filament may be reversed and the filament is allowed to return to its equilibrium conformation. The first stretching cycle shows the characteristic non-linear force response described previously [50] (Fig. 4.1d-f, dark blue), comprising an initial linear force increase, followed by a force plateau and eventually a pronounced hysteresis upon relaxation to zero strain. Note that in all experiments shown here, we pull the filament into the plateau region but not beyond. When the filament is stretched again (Fig. 4.1d-f, light blue), we observe softening, but almost reach zero strain at zero force. Furthermore, the hysteresis decreases, supporting that full recovery of the initial conformation is not achieved. However, the relaxation curve of the first cycle always lies below the
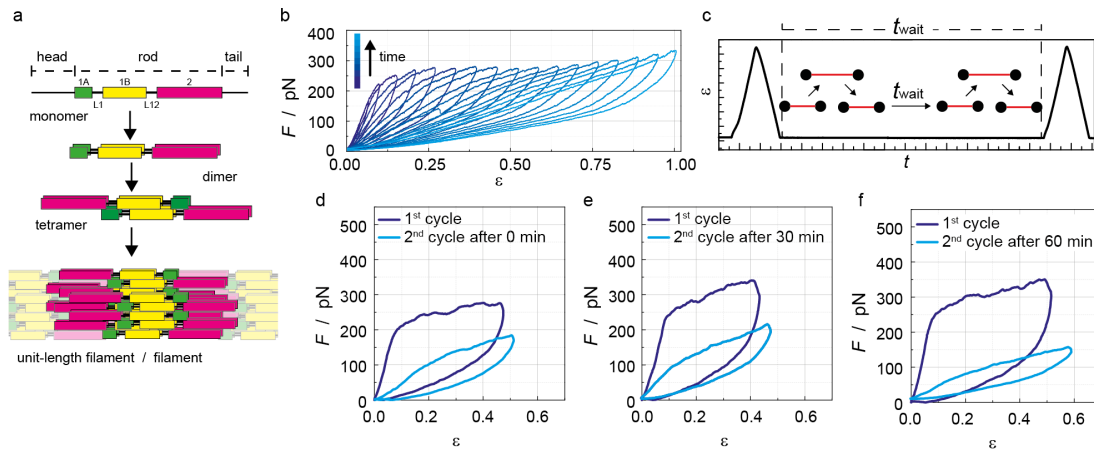
Figure 4.1: *Cycle experiments on untreated vimentin IFs.* **a** *Schematic overview of the vimentin assembly pathway from the monomer to the mature filament, via the parallel coiled-coil dimer, the half-staggered anti-parallel tetramer and the unit-length filament that on average consists of eight tetramers.* **b** *Vimentin filament stretched to increasing distances with each cycle (for a filament stretched for several times to the same distance see Appendix Fig. A.1),* **c** *Sketch of the experimental protocol for stretching cycles including waiting time t_{wait}.* **d, e, f** *Examples for force-strain data from experiments with different waiting times t_{wait}.* **d** $t_{wait} = 0$, **e** $t_{wait} = 30$ min and **f** $t_{wait} = 60$ min. *For examples of all values of t_{wait} and a box plot diagram of the input energy ratios see Appendix Fig. A.2.*

stretching curve of the second cycle, indicating partial reversibility. The ratio of the input energies required to stretch the filament the first and second time shows that the degree of reversibility is independent of t_{wait} (Appendix Fig. A.2) even after 1 h. From these experiments, we conclude that the conformational changes occurring during the initial extension of the filament are microscopically not reversible on reasonable experimental time scales. An easy way to limit the degrees of freedom upon unfolding is by introducing permanent cross-linkers, *i.e.* glutaraldehyde (GA, 5 C-atoms) and paraformaldehyde (PFA, 1 C-atom), and thereby increasing the refolding probability along the same path on which unfolding occurred. Both aldehydes may form covalent bonds with amine groups through imine formation, in particular targeting accessible lysine residues. The longer the cross-linker, the more links are expected to form.

Qualitatively, the force-extension curves are not altered by cross-linking and show the same characteristic force plateau as found for untreated filaments, albeit shifted to higher forces (Fig. 4.2a). For native, untreated vimentin IFs the origin of the force plateau was previously assigned to an increase of the contour length of the filament due to force-induced conformational changes [49, 50, 54]. The conservation of the curve shape after cross-linking indicates that unfolding of α helices in the vimentin
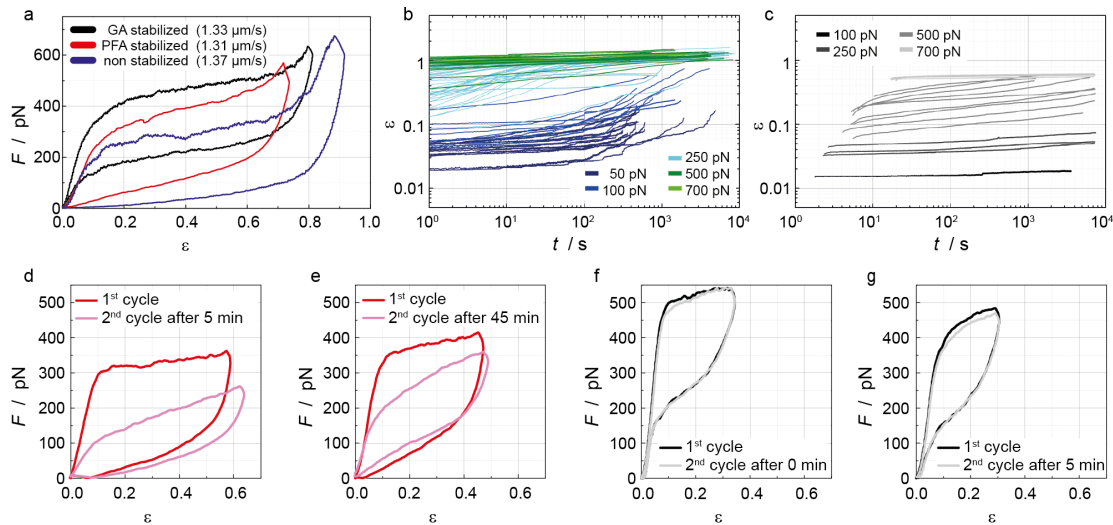
Figure 4.2: *Recovery experiments with cross-linked IFs. **a** Typical force-strain cycles of untreated (blue), PFA-cross-linked (red) or GA-cross-linked (black) filaments. **b** Force clamps of untreated vimentin IFs ranging from 50 to 700 pN, presented as a log-log plot of strain versus time. [50] **c** Force clamps of GA-cross-linked vimentin IFs ranging from 100 to 700 pN, presented as a log-log plot of strain versus time. **d**, **e**, Examples for recovery experiments performed with PFA-cross-linked vimentin IFs with $t_{wait} = 5$ min (d) and $t_{wait} = 45$ min (e). For examples of all values of t_{wait} and a box plot diagram of the energy ratios for PFA cross-linked filaments, see Appendix Fig. A.3. **f**; **g** Examples for recovery experiments performed on GA-cross-linked vimentin IFs with $t_{wait} = 0$ min (f) and $t_{wait} = 5$ min (g). For examples of all values of t_{wait} and a box plot diagram of the energy ratios for GA cross-linked filaments, see Appendix Fig. A.4.*

monomer is still possible after cross-linking with either PFA and GA. The relaxation curves of GA-cross-linked filaments, however, show a distinctly different progression compared to the untreated filaments with a force plateau and an inflection point, similar to the extension curve, albeit at a lower overall force. Force-clamp data of untreated and GA-cross-linked filaments (Fig. 4.2b, c) confirm that a much higher force is needed to extend the cross-linked filaments. Whereas the untreated filaments can be stretched up to strains higher than 1.0 at 250 pN, GA-cross-linked filaments stay at strains below 0.1 even after two hours at this force level. The force needed to stretch GA-cross-linked filaments to strains of about 0.8 is most likely around 400 pN. Repeated force-distance cycles of cross-linked filaments reveal striking differences to untreated IFs concerning the reversibility of unfolding. When PFA-cross-linked filaments are stretched again after $t_{wait} = 5$ min, they behave similar to untreated filaments (Fig. 4.2d). However, for $t_{wait} = 45$ min, there is a clear recovery towards the initial curve shape (Fig. 4.2e). By contrast, GA-cross-linked filaments show identical force-distance curves in the first and the second cycle even without any waiting time (Fig. 4.2f,g). These observations are confirmed by the input energy ratio as

a function of t_{wait} (Fig. 4.3a). Notably, at low strain the GA-cross-linked filaments behave fully elastic, *i.e.* at small strains the relaxation curve reproduces the initial slope (Fig. 4.2f, g). Thus, cross-linking with GA remodels the energy landscape of IF stretching and cross-linked filaments return to the initial conformation. These
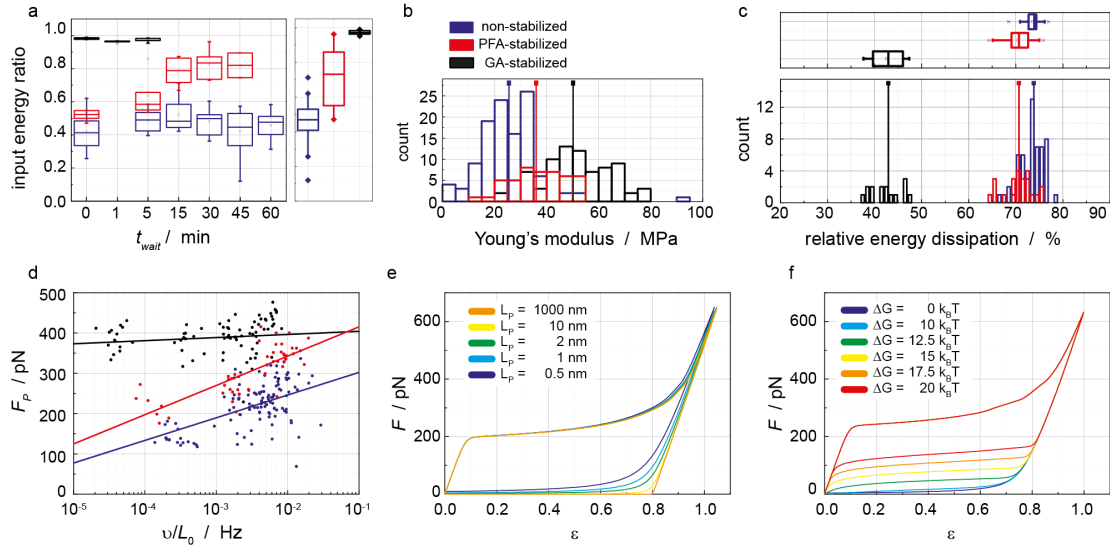

Figure 4.3: *Physical analysis and numerical simulations of vimentin IF mechanics. **a** Left: ratio of input energies between the first and the second stretching event versus t_{wait}. Right: distribution of input energy ratios for all t_{wait}. The input energy ratio for PFA-treated filaments shows a slow increase and reaches values of about 0.85 after 30 min (red). For GA-treated filaments the input energy ratio stays constant around 1 as the first and second force-distance cycles show almost identical progressions (black). **b** Histograms of Young's moduli of untreated, PFA- and GA-stailized IFs calculated from the initial slope (Appendix Fig. A.5) of the first force extension curve of each vimentin IF assuming a circular filament cross-section and a filament radius of 5 nm. Legend and color codes apply to a,c, and d as well. **c** Bottom: histograms of relative dissipated energies for untreated, PFA- and GA-cross-linked filaments. Top: distributions of dissipated energy. **d** Force at the onset of unfolding (i. e. the beginning of the plateau region) versus the normalized loading rate (Appendix Fig. A.5). **e** Simulation of force-strain curves according to Block et al. [50] without any back-reaction but with a decreasing persistence length for the retraction part of the curves. **f** Simulation of force-strain curves according to Block et al. [50] with back-reaction for different ΔG.*

results raise the question whether there exists a fundamental difference between the conformational changes during stretching for cross-linked and untreated filaments. The Young's modulus (Fig. 4.3c) already shows a clear trend. It increases from 26 MPa to 36 MPa and eventually to 50 MPa for untreated (blue), PFA-cross-linked (red) and GA-cross-linked IFs (black), respectively, indicating a strong effect caused by cross-linking. Fig. 4.3b shows histograms of the energy dissipated during the first stretching-relaxing cycle, normalized by the input energy. For PFA-treatment (red), similar values (~70-80%) to untreated filaments (blue) are found [50], whereas GA treatment (black) drastically decreases the energy dissipation to only ~ 45%.

To examine the energy landscape associated with folding and unfolding, the force at the onset of the plateau is determined and plotted against the loading rate v normalized by the initial filament length L_0 (Fig. 4.3d). Whereas the plateau forces for PFA-cross-linked and untreated filaments show a similar velocity dependence, albeit with slightly higher plateau forces for the cross-linked filaments, the GA-cross-linked filaments show very high plateau forces around 400 pN that are almost independent of the loading rate. We have shown previously that the force-extension curve of vimentin can be modelled with an elastically coupled two-state-model [49]. This model predicts a logarithmic scaling of the plateau force with pulling velocity (see Supporting Information, equation 5). For the untreated filaments we find a potential width $x_u = 0.17 \pm 0.02$ nm (mean $\pm$ st.d.) and a zero-force reaction rate of $k_0 = (5 \pm 4) \cdot 10^{-7}$ s^{-1} in good agreement with the parameters found previously by directly fitting to individual force-strain curves [49]. Treatment with PFA leads to an only slightly decreased potential width of $x_u = 0.13 \pm 0.02$ nm and zero-force reaction rate of $k_0 = (2.5 \pm 2) \cdot 10^{-7}$ s^{-1}. By contrast, GA drastically alters the energy landscape. The reaction is slowed down dramatically, $k_0 = (1 \pm 8) \cdot 10^{-54}$ s^{-1}, which is accompanied by an enormous increase of the potential width, $x_u = 1.2 \pm 1$ nm. This huge change probably indicates that the molecular elongation mechanism is fundamentally different after GA-treatment. Therefore, it is remarkable that basic characteristics of the tensile behavior like the high extensibility and the force plateau are largely conserved after cross-linking.

We can only speculate about the molecular origin of the observed changes due to cross-linking. However, a previous cross-linking study employing disulfosuccin-imidyl tartrate (DST), which is only one carbon atom shorter then GA, led to a dense network of cross-links in vimentin IFs [120, 121]. It has been shown previously that the formation of intramolecular cross-links is highly unlikely. Downing [121] showed that cross-linking between two lysine groups that are both within an α-helical region is unusual. This is true within dimers as well as between dimers as steric hindrance prevents linkage between lysines in identical sequence locations in the α-helical regions of parallel chains. As a consequence, intermolecular cross-links are predominately found in random coil conformations and β sheets. It is expected that these cross-links prevent the necessary rotation of the peptide chain for the α helices to completely unfold, so we regard them as pinning points for the protein conformation, which ensure the presence of a reasonably close starting point for the reformation of the α helices.

Molecular dynamics simulations have shown that coiled coils need a critical length

of about 40 amino acids in order to be able to undergo an α-β-transition [122], which is in good agreement with the dramatically increased stability we observed for the short α-helical segments between the cross-links. Furthermore, we assume that, when the α helices in GA-cross-linked filaments unfold, parallel helices have to unfold simultaneously since they are covalently connected. This is in contrast to the untreated filament, where computational models have predicted that parallel unfolding is initiated by stochastic opening of a few monomers which leads to loss of stability of all remaining parallel helices, [50] similar to what has been observed in binding clusters [123, 124]. Using the analogy to binding clusters, this can be regarded as an extreme case of shared loading which might explain the huge increase of the potential width [125, 126].

The relaxation force curve of untreated vimentin IFs as shown in Fig. 4.2a, blue, decays almost linearly from a restoring force around 100 pN at a strain of 0.8 to zero force at strains below 0.1. This positive restoring force was earlier interpreted as a sign of reversibility of the underlying molecular process. This can be illustrated by modelling the force extension curve using a two-state-model for the filament elongation introduced earlier [50]. If we switch off the back-reaction in the model (Fig. 4.3e) the force drops to zero already at large strains around 0.8 if we assume that the persistence length of the filament stays constant at 1 μm upon stretching (orange). If, however, the persistence length is decreased dramatically upon stretching, a force progression closer to the experimental relaxation curve is recovered (green, blue, purple). This is plausible, since a thinning of IFs upon stretching has been observed [44, 45] and would lead to smaller persistence lengths. Furthermore, since coiled coils are particularly rigid, it is likely that the filament gets more flexible when being unfolded. Indeed, a similar mechanism with a drastic decrease in persistence length upon unfolding was proposed by Minin et al. for the α-β-transitions in simpler coiled-coil peptides [127]. In contrast to an earlier interpretation, we conclude that entropic elasticity of the protein chain is sufficient to explain the restoring force upon filament relaxation for untreated vimentin filaments.

The force plateau and inflection point in the relaxation curves of GA-cross-linked filaments (Fig. 4.2a, black), are reproduced by the two-state-model when increasing the energy difference ΔG between the shorter and the longer state and thereby the reversibility of the transition (Fig. 4.3f). This indicates that the positive restoring force of GA-cross-linked filaments originates from the refolding enthalpy of the α helices. Interestingly, a similar increase in reversibility might also be achieved by a symmetrization of the energy landscape. The strongest argument for the proposed
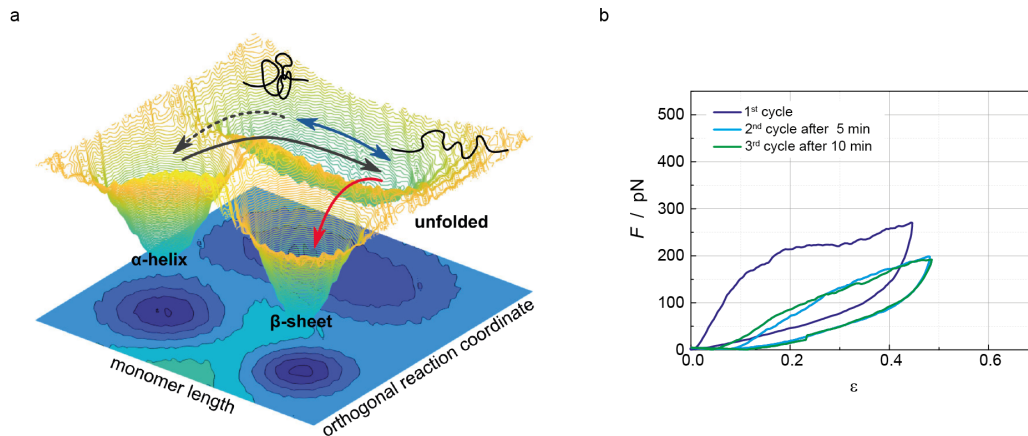
Figure 4.4: *Introduction of a third conformational state during vimentin IF stretching. **a** Energy landscape illustrating the proposed model. Besides the two well-defined α-helical and β sheet conformations, there exists a less defined unfolded conformation along an orthogonal reaction coordinate. When a force is applied, the α helix can unfold (black arrow) and the unfolded random coil can be stretched (blue arrows). **b** An untreated vimentin IF is cycled three times with t_{wait}=5 min between the cycles. Whereas the force-strain behavior of the second cycle differs considerably from the first one, the data for the third cycle are almost identical to the second one.*

reversibility of vimentin elongation was the observation that repeated cycles always start at nearly the same strain (Fig. 4.1a) and that only very little residual plastic strain of vimentin was observed (Appendix Fig. A.6). The softening of filaments without residual strain was explained by mixed states – α-helical and elongated – in the parallel monomers. However, the observed force plateau requires all parallel monomers in a unit length filament to elongate in a cascading manner [50]. Thus the softening with repeated cycles can only be explained when there is a way for elongated monomers to return to a shorter effective length, which seems to contradict the non-reversibility we observe here.

To resolve the contradiction, we propose a model for which the transition between the shorter and the longer state is not a one-step process as assumed in the two-state-model proposed previously [49], but consists of three distinct states (Fig. 4.4a). When a force is applied to the filament, the α-helical coiled coils unfold (black arrow) and the polypeptide chains assume a random coil. This unfolding can be described as a transition along a reaction coordinate orthogonal to the applied force. Due to its high energy cost this reaction does not occur spontaneously but only at high loads around 200 pN, *i.e.* the plateau force. The unfolded chain can elongate in response to the applied strain leading to a reversible extension of the monomer (blue arrow). This elongation has presumably not only an entropic cost to extend the semiflexible polypeptide chain, but also an enthalpic component due to the breaking

and formation of hydrogen bonds, rendering the energy landscape of the unfolded state rather rough. This roughness of the energy landscape might indeed give rise to the viscoelastic relaxation behavior investigated earlier, where we find a power law behavior [50]. When the random coil is elongated, hydrogen bonding between parallel polypeptide chains can lead to the formation of β sheets (red arrow). This process is presumably rather slow, since the polypeptide chains need to assume the exact right geometry, and irreversible, due to the high energy difference. When the filament is subsequently relaxed, only the peptide chains that were not able to form a β sheet will return to a shorter contour length. Since the relaxed unfolded polypeptide chain can assume many possible conformations, reformation of α helices is highly unlikely (dashed arrow).

Our model is supported by an experiment, where we cycle an untreated filament three times with a waiting time of $t_{wait}=$ 5 min between the cycles. Whereas the data for the second cycle (light blue) differ from the first one (dark blue), in line with the data shown in Fig. 4.1, the third cycle (green) progresses in an identical manner to the second one. In our model energy landscape (Fig. 4.4a) we interpret this as follows: upon first stretching, the α helices are unfolded into random-coils, which are subsequently elongated. Relaxation and repeated stretching leads to "shuffling" between the short and the long random-coil state and thus to identical force-strain curves.

This model is sufficient to justify why the filament always returns to essentially the same contour length, while also explaining the observed irreversibility. Apparently, PFA-cross-linked polypeptide chains are kept close enough to the starting conformation that slow refolding of the α helices is observed, leading to a slow recovery of the initial force extension curve. By contrast, the energy landscape of the GA-cross-linked filaments is strongly altered, and rather resembles the idealized two-state-model, with an energetically heavily favored shorter state and a spontaneous back-reaction from the elongated state. From our measured force-strain cycles (Fig. 4.2a, black) and the proposed model, one may draw an analogy to pseudoelastic (also referred to as superelastic) shape-memory alloys, which, when heated after being strained, return to a previous shape [128]. Of note, however, in our system, we do not observe a phase transition, as required for pseudoelasticity.

4.1.4   Conclusion

By employing controlled *in vitro* experiments, we are able to precisely tune mechanical strain-response of vimentin IFs to applied stress. Untreated IFs can be stretched to high strains and largely recover their original length upon relaxation, *i.e.* only neglectable residual strain is observed. As the filaments soften with each subsequent cycle and the original stiffness is not recovered on reasonable experimental time scales, we examine the energy landscape of strained IFs in detail. Our experiments lead to the conclusion that besides the *α* helix and the *β* sheet a third – presumably random coil – conformational state must exist, and that subunits are not able to return to their initial state after stretching. This irreversible transformation is avoided when introducing permanent cross-linkers into the system and thereby reducing the degrees of freedom upon stretching.

The irreversibility of the conformational changes we observed here might indicate that vimentin filaments that were strained in the past are not as capable to protect the cellular integrity. This implies that cells need a mechanism to "repair" strained vimentin. This reversibility may be achieved by either subunit exchange along the filaments [129–131], which is, however, very slow, or by disassembly and reassembly of filament structures as observed *e.g.* for keratin networks [132, 133].

Interestingly, the microscopic reversibility and the increased stiffness we observed as a result of GA-fixation seem to be advantageous mechanical properties for cells that are heavily subjected to external strains. For keratin IFs in maturating keratinocytes, controlled covalent cross-linking of subunits by disulfid bond formation is indeed observed and might be a possible avenue for cells to tune their resistance to external forces [134, 135]. Interestingly, vimentin was identified as a substrate for proteins introducing covalent cross-links between different monomers, specifically transglutaminases, in two human tissues where structural integrity is paramount, arteries and lens [136, 137]. Like the cross-linkers used in our work, transglutaminases target primary amines suggesting they might alter the energy landscape in a way similar to what we show in our *in vitro* system.

4.1.5   Methods

Vimentin production and purification

The production and purification of recombinant human vimentin C328A with additional amino acids GGC at the C-terminus for force clamp and multiple-cycle-

measurements was performed as described previously [50]. For all other experiments the protein purification was performed similar to the protocol described previously [50] but with several changes to the buffers used, as described in the Appendix A.1.

Vimentin and bead functionalization

Vimentin was labeled, reconstituted, and assembled according to previously published protocols. Labeling with ATTO647N (ATTO-Tech GmbH) and biotin-maleimide (Jena BioSciences GmbH) was performed according to Block et al. [49] and Winheim et al. [105]. Reconstitution and assembly were performed as described by Block et al. [50].
Carboxylated polystyrene beads were functionalized according to Janissen et al. [108] as described in Block et al. [50].

Optical tweezers measurements

Optical tweezers measurements were performed using a commercial instrument (C-trap, Lumicks, Amsterdam, Netherlands), combining optical tweezers with a microfluidic setup and confocal microscopy (Appendix Fig. A.7), similar to what was described previously [50]. In short, a fresh pair of beads was captured for each experiment in the bead channel. A vimentin IF was captured in the vimentin channel and bound to the second bead in the buffer (100 mM KCl in 2 mM phosphate buffer, pH 7.5) channel. Parts of the measurements were performed with filaments bound to the beads by maleimide-chemistry and parts of the experiments with filaments bound via biotin-streptavidin. The covalent attachment of the filaments via maleimide-groups enables us to introduce waiting times between the filament stretching cycles. For cross-linking experiments the captured vimentin IF was moved to channel 4 (Appendix Fig. A.7) filled with buffer containing either PFA (0.12 % (v/v)) or GA (0.5 % (v/v)). Before a force-distance curve was recorded, the filaments were always moved back to the channel that only contains buffer (channel 3, Appendix Fig. A.7). Additionally, a prestrain of 5 pN was imposed for all recovery experiments. This prestrain prevents the filaments from wrapping around the beads during the waiting time as well as the loss of the filament during that time. Before the actual measurement, this value was set to 0 pN and the thus defined prestrained length of the filament was used as initial length L_0 to calculate the dimensionless strain during stretching.
Following the measurement protocol sketched in Fig. 4.1b, we stretched the filament

beyond the linear regime into the characteristic plateau region, where unfolding of the α helices occurs. Subsequently, we relaxed the filament and, after a defined time $t_{\text{wait}} \leq 1$ h, stretched the filament again to the same trap position as in cycle one. The length of the filament and the applied force were recorded over the full experiment.

Data Sets

For the untreated filaments 57 individual recovery experiments were performed. The total number of recovery measurements for GA-cross-linked filaments was 15 and for PFA-cross-linked filaments it was 23. For the force-clamp experiments of untreated filaments about 100 measurements were performed. The number of force-clamps of GA-cross-linked filaments was 18.

Data analysis

All data were converted to ASCII format with the measuring software (TWOM, Lumicks). The bead diameter was subtracted from the distance and the time and force data were used as measured. To calculate the energy for the first cycle, the area beneath the stretching curve up to the maximum strain was calculated by integration. As we can only control the position of the trap and not the position of the bead, the maximum strain of the second stretching is slightly higher than the maximum strain for the first stretching cycle, due to the softening of the filament. To compare the input energy that was needed to strain the filament to the same length again, the energy needed for the second stretching was calculated by integrating the area beneath the second stretching curve but only up to the maximum strain of the first stretching curve. The two energy values were then divided to obtain the input energy ratio. In order to determine the Young's modulus, the initial slope of the force extension curve was determined by a linear fit. Only data points with forces larger than 10 pN and smaller than 80% of the plateau force and at positive strains where considered. The force at the onset of the plateau was determined by connecting the first and the last data point of an extension curve with a straight line and subtracting this straight line from the force curve. This effectively tilts the force curve, such that the beginning of the plateau can be determined as the maximum of the tilted curve. A logarithmic scaling law (see Supporting Information, equation 5) was fitted to the plateau force as a function of the pulling velocity v normalized by the initial filament length L_0. To estimate the uncertainty of the parameters, a bootstrapping algorithm [138] with 10000 iterations was used.

4.2   Vimentin Stretching Cycles at Varying Loading Rates

Previous studies have shown that single vimentin filaments exhibit a loading rate dependent stretching behavior [49]. Here, we investigate whether this loading rate dependency has an effect on the recovery behavior of vimentin filaments. The same setup as in Chapter 4.1 is used. In addition to the single loading rate used there, which is $0.7\,\mu m/s$, loading rates of $0.1\,\mu m/s$ and $2.8\,\mu m/s$ are used, and the waiting times range from $0\,min$ to $45\,min$. The different loading rates were chosen such that a wide range of pulling speeds from very slow, to medium and fast are achieved. To estimate the ability of recovery, we calculate the energy needed to stretch the filament up to a specific strain, *i.e.* the area underneath the stretching curve as described in more detail in Chapter 4.1, for the first and second stretching cycle and calculate the ratio between those two values. As discussed in Chapter 4.1, no recovery is observed for waiting times of up to $60\,min$. Therefore, waiting times up to $45\,min$ are recorded in this chapter. The input energy ratio for small loading rates, *i. e.* $0.1\,\mu m/s$, shows a slight increase from $0\,min$ to $5\,min$, see Fig. 4.5a, unlike the input energy ratio at medium loading rates of $0.7\,\mu m/s$ which stays constant over time, see Fig. 4.5b. Nevertheless, the distribution of energy ratios over all waiting times for these two data sets are similar as shown in Fig. 4.5d, blue and red plot. For the high loading rate, *i. e.* $2.8\,\mu m/s$, we also observe a slight increase of the input energy ratio between $0\,min$ and $5\,min$ waiting times but it stagnates for longer waiting times, see Fig. 4.5c. In comparison, the input energy ratio at the highest loading rate is shifted to higher values as shown in Fig. 4.5d, black plot.

To understand these observations, the structural changes of vimentin during stretching are important. While a single vimentin filament is stretched, different regimes are observed: a linear, elastic stretching, a plateau regime and a subsequent stiffening [47–49, 139]. For the experiments described in this chapter, we stretch the filaments up to the plateau regime and this regime is linked to the unfolding of α helices in the rod domain of vimentin. A possible explanation of the increased ability to recovery at high loading rates is that the filaments are stretched so rapidly that fewer α helices have time to fully unfold before the filament is relaxed again. Hence, not completely unfolded α helices can return to their initial state and this results in an overall higher energy ratio which means we have an increased ability to recover the initial state during the relaxation. This hypothesis is in accordance to the observations in Ref.
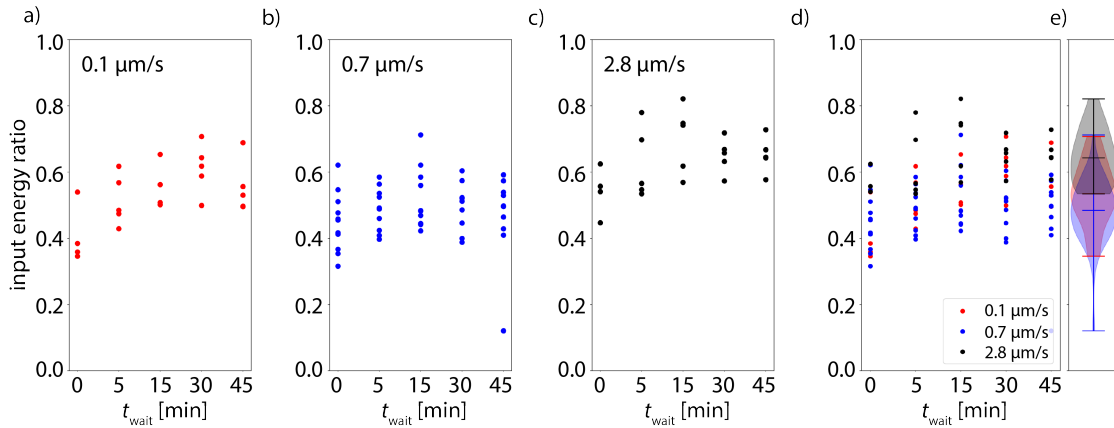
Figure 4.5: *Stretching cycles with varying loading rates lead to changes in recovery behavior of vimentin. a)-c) Input energy ratio for waiting times ranging from 0 min to 45 min, at the loading rates of a) 0.1 µm/s, b) 0.7 µm/s and c) 2.8 µm/s. Each data point represents the repeated stretching of one single filament. d) Comparison of the input energy ratios at different loading rates. e) The violin plot shows the distribution of all energy ratios for all waiting times. The energy ratio for small loading rates, 0.1 µm/s and 0.7 µm/s, strongly overlap while the energy ratio at high loading rates, 2.8 µm/s, are slightly increased.*

[49] where higher forces were needed to reach the plateau region at a high loading rate, comparable to the highest loading rate used in these experiments. Thus, using higher loading rates requires higher forces to unfold the α helices in the rod domain of vimentin. Therefore, the probability to unfold the same amount of α helices, compared to lower loading rates such as 0.7 µm/s and 0.1 µm/s, decreases.

To summarize our findings from these vimentin recovery experiments at varying loading rates, we observe that the recovery behavior of vimentin at both small loading rates is similar. However, if we increase the loading rate, the ability to recover from stretching increases. Nevertheless, full recovery is not achieved at any of the tested loading rates and this observation is independent of the waiting times used in these experiments.

4.3 Repeated Stretching Cycles in the Elastic Regime

The linear increase at low strain values observed while stretching single vimentin filaments is associated to the elastic stretching of the α helices in the rod domain [47, 139, 140]. Here, we study the recovery behavior of vimentin filaments under repeated cyclic stretching to small strains within this elastic regime. We observe that repeated cycles with a maximum force in the first cycle above 200 pN, close to the beginning of the plateau regime, show a softening at repeated stretching, see
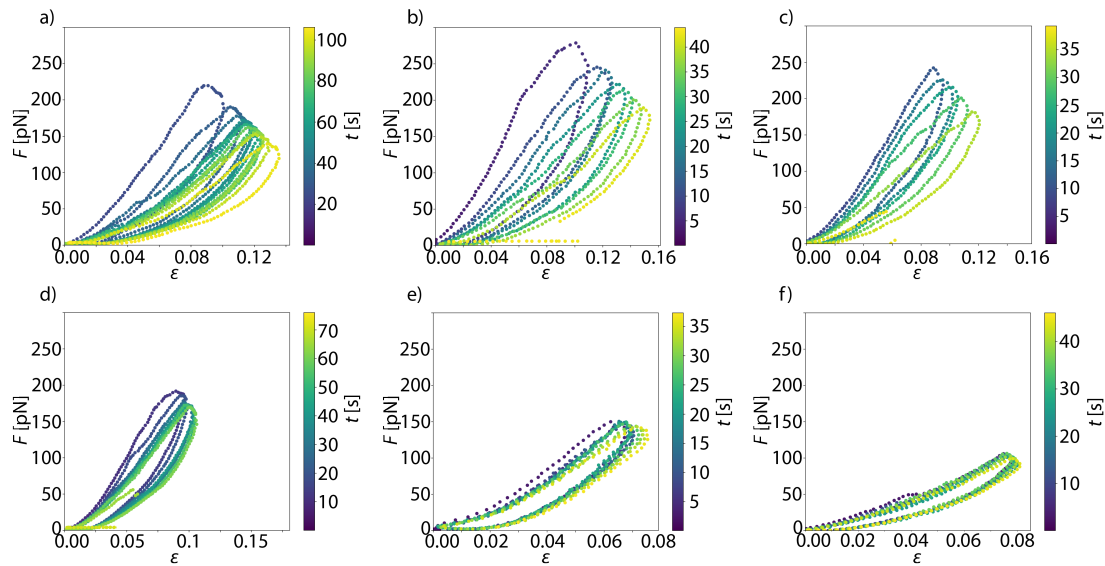
Figure 4.6: *Repeated stretching cycles in the elastic regime of vimentin. The filaments are stretched repeatedly until the filament breaks or it releases from one of the beads. a)-c) Repeated cycles with a maximum force of the first cycle of more than 200 pN. All show a softening at repeated stretching. d)-f) Repeated cycles with a maximum force of the first cycle of less than 200 pN. All show low or no softening at repeated stretching.*

Fig. 4.6a-c. For repeated cycles with a maximum force below 200 pN we see much less or no softening at repeated stretching, see Fig. 4.6d-f. An explanation for this behavior is that the unfolding of α helices in the rod domain of vimentin occurs only at higher loads of around 200 pN. The closer we get to the onset of the plateau, the more likely it is that more α helices unfold and we therefore observe the softening from repeated stretching cycles. For forces lower than 200 pN it is less likely that α helices unfold and therefore we see much less or no softening. These findings further support our hypothesis in Chapter 4.1: for the unfolding of α helices a large amount of input energy is needed, therefore the softening behavior at repeated stretching cycle is only observed at forces around 200 pN or higher. The unfolded α helices are not able to fold back to their initial structure and therefore the filaments get softer with each stretching cycle. As we do not observe this softening behavior for forces below 200 pN, this observation can be linked to the unfolding of α helices and the inability to return to the initial state when the filament is relaxed again.

5

Influence of Post-Translational Modifications on Vimentin Mechanics

The properties of single vimentin filaments do not only change when external stress is applied but also when the protein gets modified. These kind of protein modifications take place after the translation of the protein and are therefore called post-translational modification. To investigate the effect of post-translational modifications on single vimentin filaments, we induce such a modification by phosphorylation and test the mechanical properties by stretching the modified vimentin filaments. Next, we employ phosphomimetic mutants to further investigate the change in mechanics. As a last step, additional mutants are used to test and strengthen our hypothesis.

5.1 Post-Translational Modifications Soften Vimentin Intermediate Filaments

Julia Kraxner[1], Charlotta Lorenz[1], Julia Menzel[2*], Iwan Parfentev[3], Ivan Silbern[3,4], Manuela Denz[1], Henning Urlaub[3,4], Blanche Schwappach[2,5], Sarah Köster[1,5,6]

[1] Institute for X-Ray Physics, University of Göttingen, 37077 Göttingen, Germany
[2] Department of Molecular Biology, University Medical Center Göttingen, 37073 Göttingen, Germany [3] Bioanalytical Mass Spectrometry, Max Planck Institute for Biophysical Chemistry, 37077 Göttingen, Germany [4] Bioanalytic Group, Institute of Clinical Chemistry, University Medical Center Göttingen, 37075 Göttingen, Germany [5] Cluster of Excellence "Multiscale Bioimaging: from Molecular Machines to Networks of Excitable Cells" (MBExC), University of Göttingen, Germany [6] Max Planck School "Matter to Life"

Contribution to this article: S.K. conceived and supervised the project. J.K. performed the experiments and analyzed the data. J.M. and B.S. provided the 14–3–3 protein. H.U., I. P. and I. S. performed the mass spectrometry measurements. C.L. performed the numerical simulations. M.D. performed the small-angle X-ray scattering experiments. J.K. and S.K. wrote the manuscript with contributions from all authors.

5.1.1 Abstract

The mechanical properties of biological cells are determined by the cytoskeleton, a composite biopolymer network consisting of microtubules, actin filaments and intermediate filaments (IFs). By differential expression of cytoskeletal proteins, modulation of the network architecture and interactions between the filaments, cell mechanics may be adapted to varying requirements on the cell. Here, we focus on the intermediate filament protein vimentin and introduce post-translational modifications as an additional, much faster mechanism for mechanical modulation. We

study the impact of phosphorylation on filament mechanics by recording force-strain curves using optical traps. Partial phosphorylation softens the filaments. We show that binding of the protein 14–3–3 to phosphorylated vimentin IFs further enhances this effect and speculate that in the cell 14–3–3 may serve to preserve the softening and thereby the altered cell mechanics. We explain our observation by the additional charges introduced during phosphorylation.

5.1.2 Introduction

The cytoskeleton of eukaryotes consists of three filament systems – microtubules, actin filaments and intermediate filaments (IFs) – which form a complex biopolymer network. The exact composition of the cytoskeleton and the interplay between the three filament types largely influence the mechanical properties of different cell types [111]. Microtubules and actin filaments are highly conserved throughout cell types, whereas more than 70 human genes encode for IFs [5], yet they all share the same hierarchical assembly pathway from monomers to filaments. The secondary structure of the monomers consists of an α-helical rod domain, flanked by intrinsically disordered head and tail domains [12, 13]. During assembly, two monomers align and form parallel coiled-coil dimers, two dimers form antiparallel, half-staggered tetramers, and multiple tetramers constitute a unit-length filament (ULF) (see Fig. 5.1a). Subsequent longitudinal annealing yields elongated filaments with a diameter of about 10 nm [9]. This hierarchical structure of IFs, in contrast to polar microtubules or actin filaments, grants IFs their unique mechanical properties [47, 49, 51].

The most abundant IF protein, vimentin, is found in cells of mesenchymal origin [9, 141]. Single vimentin filaments are highly extensible and can be elongated up to at least 4.5 fold [44, 45, 49]. During elongation, three regimes are observed in the force-strain curves: an initial linear (elastic) increase, a plateau region and a subsequent stiffening [46–49]. These different stretching regimes have been linked to structural changes in the rod domain of IFs [46] such as the opening of α helices during the plateau regime [47, 50, 55]. Additionally, vimentin filaments are able to dissipate large amounts of the input energy while being stretched [50]. Consequently, vimentin IFs act as shock-absorbers for mechanical protection of the cell as well as scaffolds that help to maintain cell shape and organization of the cytoskeleton [141, 142].

An effective way to tune the mechanics of IFs is the variation of the charges of the amino acids constituting the protein [52]. One cellular mechanism for such charge

variation are post-translational modifications (PTMs). Within the IF cytoskeleton, several types of PTMs have been described [35, 143] and the most abundantly studied PTM in IFs is phosphorylation, which is involved in regulation of IF dynamics by leading to disassembly and in providing binding sites to signaling proteins [31, 32]. It has been shown that the phosphorylation of vimentin by protein-kinase A (PKA) leads to various phosphorylated sites, most of which are positioned in the head region (see Fig. 5.1a) [31]. The importance of the head domain in the assembly process was shown in Refs. [12, 144], stressing the obvious link between phosphorylation and assembly dynamics. Although such changes in the molecular interactions during assembly are likely to influence the behavior of the fully assembled filaments, the influence of phosphorylations on filament mechanics is not yet resolved.

A further interesting aspect of phosphorylation is the ability of certain proteins to bind to the modified sites. One such protein is 14–3–3 [27], which is involved in several cellular processes like signal transduction, adhesion and inhibition of tumorigenesis [28]. The role of this protein depends on the interaction partner, *e.g.* it binds to keratin during the cell cycle [29] and affects the assembly dynamics of neurofilaments [30]. However, the role of 14–3–3 for vimentin is unknown.

Here we investigate the effect of phosphorylation and 14–3–3 on vimentin mechanics by studying precise force-strain curves from optical trap experiments. We find that the filaments soften with increasing amount of phosphorylated protein within the filament and that interaction with the protein 14–3–3 further enhances this effect. By combining our mechanical measurements with mass spectrometry, cross-linking, phosphomimicry and numeric modeling, we are able to attribute the softening to reduced lateral coupling of monomers within the filaments.

5.1.3   Experimental

An extended version of the Methods section can be found in the Appendix A.2.1.

Vimentin Purification

Purification of recombinant human vimentin C328A with additional amino acids glycine-glycine-cystein at the C-terminus based on Herrmann *et al.* [16] was performed [50]. The additional amino acids were included to enable binding of the vimentin filaments to maleimide-functionalized beads and for fluorescent labeling of the monomers. Removing the cystein from the rod domain of the protein enables smooth assembly even after labeling. As we did not add zinc ions in our experiments
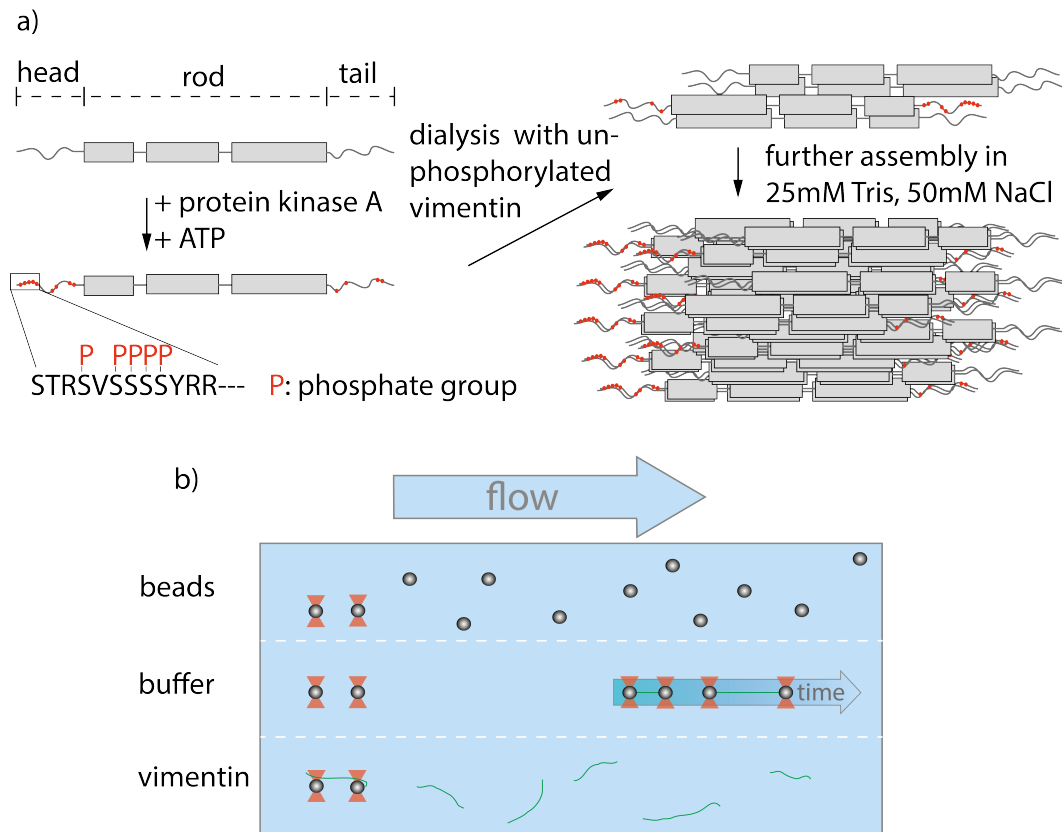
Figure 5.1: *Experimental design and setup. a) Assembly process of partially phosphorylated vimentin. Vimentin monomers consist of a central rod domain flanked by intrinsically disordered head and tail domains. A part of the monomers are phosphorylated by addition of protein-kinase A and ATP leading to several phosphorylated sites in the head and tail, highlighted in red. The phosphorylated monomers are mixed with unphosphorylated vimentin prior to assembly by dialysis into a salt-containing buffer. b) Overview of the microfluidic chip used within the optical trap. The different compartments are realized by laminar flow and the measurements are performed in the buffer region.*

[102], the missing cystein is not expected to influence the assembly and architecture of the filaments. Indeed, it has been shown that vimentin C328A assembles in the same way as wildtype vimentin [105]. Two phosphomimetic mutants S38E and S72E of this vimentin C328A were produced according to the same protocol. We performed all control measurements with vimentin C328A and thus ensured that all observations were due to phosphorylation or phosphomimicry.

Vimentin filament preparation and bead functionalization

Vimentin was fluorescently labeled with ATTO647N *via* maleimide chemistry [49] to enable visualization of the filaments during the optical trapping experiments. To prepare the protein for filament assembly, the protein in storage buffer (8 M urea, 5 mM Tris-HCl, 1 mM EDTA, 0.1 mM EGTA, 0.01 mM MAC and 250 mM KCl, pH 7.5) was dialyzed against 6 M urea, 5 mM Tris-HCl at pH 8.4 and a stepwise dialysis against 5 mM Tris-HCl, pH 8.4 was performed. To initiate the assembly, the protein was dialyzed against 25 mM Tris-HCl, pH 7.5 with 50 mM NaCl over night. The final amount of labeled monomers within the filaments was about 4%. In analogy to the assembly of phosphorylated vimentin, the phosphomimetic mutants were mixed with vimentin C328A at mixing ratios of 1%, 5% and 10%. The mixing was performed in 8 M urea, *i.e.* prior to the dialysis step to ensure mixing at the monomer state of vimentin.
Carboxylated polystyrene beads (Kisker Biotech GmbH & Co. KG, Steinfurt, Germany) with a diameter of 4.4 μm were functionalized with maleimide according to Ref. [108].

Phosphorylation of vimentin

We phosphorylated vimentin tetramers in 5 mM Tris-HCl, pH 8.4 using cAMP--dependent protein kinase A (New England Biolabs, Frankfurt, Germany). The phosphorylated vimentin was mixed at the desired ratios of 1, 5 and 10% with unphosphorylated vimentin. Subsequently, a stepwise dialysis and the assembly were performed as described above.

5.1.4 Experimental setup and data analysis

Optical trap measurements and analysis

For all measurements a commercial optical trap setup (C-trap, Lumicks, Nether-lands), including a microfluidic chip and confocal microscopy, was used. For each measurement a fresh pair of beads was captured in the bead channel (see Fig. 5.1b). The calibration of the optical trap was performed by analysis of the power spectral density of the thermal fluctuations of the trapped beads in the buffer channel. Af-terwards they were moved to the vimentin filament channel, while scanning with the confocal microscope, until a single vimentin filament was captured on one bead. Then, the beads were moved back to the buffer channel where the filament was attached to the second bead. We ensured that the filament was relaxed to avoid prestrain. The measurements were performed by moving one bead at about $0.7\,\mu$m/s to stretch the filament until it ruptured or the forces on the second bead were higher than the maximum trapping force. During the stretching, force-distance curves were recorded.

Data were analyzed with self-written Python codes. The calculation of the mean curves for each conditions was adapted from Ref. [51]. For the calculation of the Young's modulus, a linear fit up to a force of 130 pN was performed for the initial slope in the linear regime of the mean force-strain curves. The Young's modulus was calculated *via* the ratio of stress and strain, $Y = \sigma/\varepsilon = F/(\pi R^2 \varepsilon)$. For the radius R, the corresponding values for the radius of gyration of the cross-section, R_c, obtained from the small-angle X-ray scattering experiments, were used.

Model

To simulate the force-strain behavior of a vimentin IF, we calculated all spring constants of the modeled elements and transition rates of possible reactions and ran a Monte-Carlo simulation with a self-written Matlab code (MathWorks, Natick, Massachusetts, USA) as in Ref. [50, 51].

5.1.5 Results and discussion

To investigate whether phosphorylation of vimentin influences filament mechanics, we record force-strain curves using optical traps. As complete phosphorylation of vimentin filaments leads to disassembly [31], we perform the stretching experiments on partially phosphorylated vimentin filaments with varying percentages of 1, 5 or

10%, as sketched in Fig. 5.1a. The incorporation of the phosphorylated vimentin is confirmed by sodium dodecyl sulfate-polyacrylamide gel electrophoresis (SDS-page) and by fluorescence microscopy, shown in Appendix Figs. A.9 and A.2.1. The single filaments are covalently bound to two polystyrene beads and each bead is captured in an optical trap for precise force measurements. Filaments with 10% phosphorylated protein incorporated assemble to the same total length as unphophorylated filaments, see Appendix Fig. A.11. Additionally, we determine the distance between both beads and calculate the strain as $\varepsilon = \Delta L / L_0$, where L_0 is the original filament length and ΔL the additional extension upon application of a force F. We perform all measurements in the "buffer" channel, *i.e.* without any disturbance from surrounding beads or protein, see Fig. 5.1b. During stretching, we observe the characteristic response of vimentin to the force, including the linear increase for small strains, the plateau region, where the α helices open up [47, 49, 50] and the subsequent stiffening of the filaments. We perform all measurements in 25 mM Tris-HCl, 50 mM NaCl, pH 7.5 and the curves are comparable to the ones previously recorded in phosphate buffer [49, 50], see Appendix Fig. A.12. The pH of the measuring buffer is chosen such that it is comparable to most *in vitro* studies on vimentin filaments. For a lower pH, we expect the same shape of the curve, but slightly shifted to higher forces, as shown recently in Ref. [52]. Such a typical curve for our standard condition is shown in Fig. 5.2a, green. We show an average curve here for clarity, however, the individual data sets are shown in the Appendix Fig. A.13. The measurements end when the force becomes too large for the optical traps, *i.e.* at roughly 550-600 pN. Even though strong phosphorylation leads to disassembly of vimentin filaments [31], we do not observe an increase in the number of breakage events upon increasing phosphorylation.

Fig. 5.2a also shows corresponding data for filaments containing a certain percentage of phosphorylated protein (shades of blue, for color code see legend). To quantify the force-strain data, we focus on the Young's modulus, which we calculate from the initial slope in the linear regime up to a force of 130 pN of each curve, as a measure of the filament stiffness. The Young's modulus for the unphosphorylated vimentin filaments is in good agreement with the results found in Ref. [49]. The analysis procedure is visualized in Appendix Fig. A.14. The Young's moduli plotted in Fig. 5.2d (green) show a strong decrease with increasing percentage of phosphorylated protein. Further analysis of the force-strain curves shows a decrease of the force at the onset of the plateau and an increase of the maximum strain reached with an increasing amount of phosphorylation, shown in Appendix Fig. A.15.
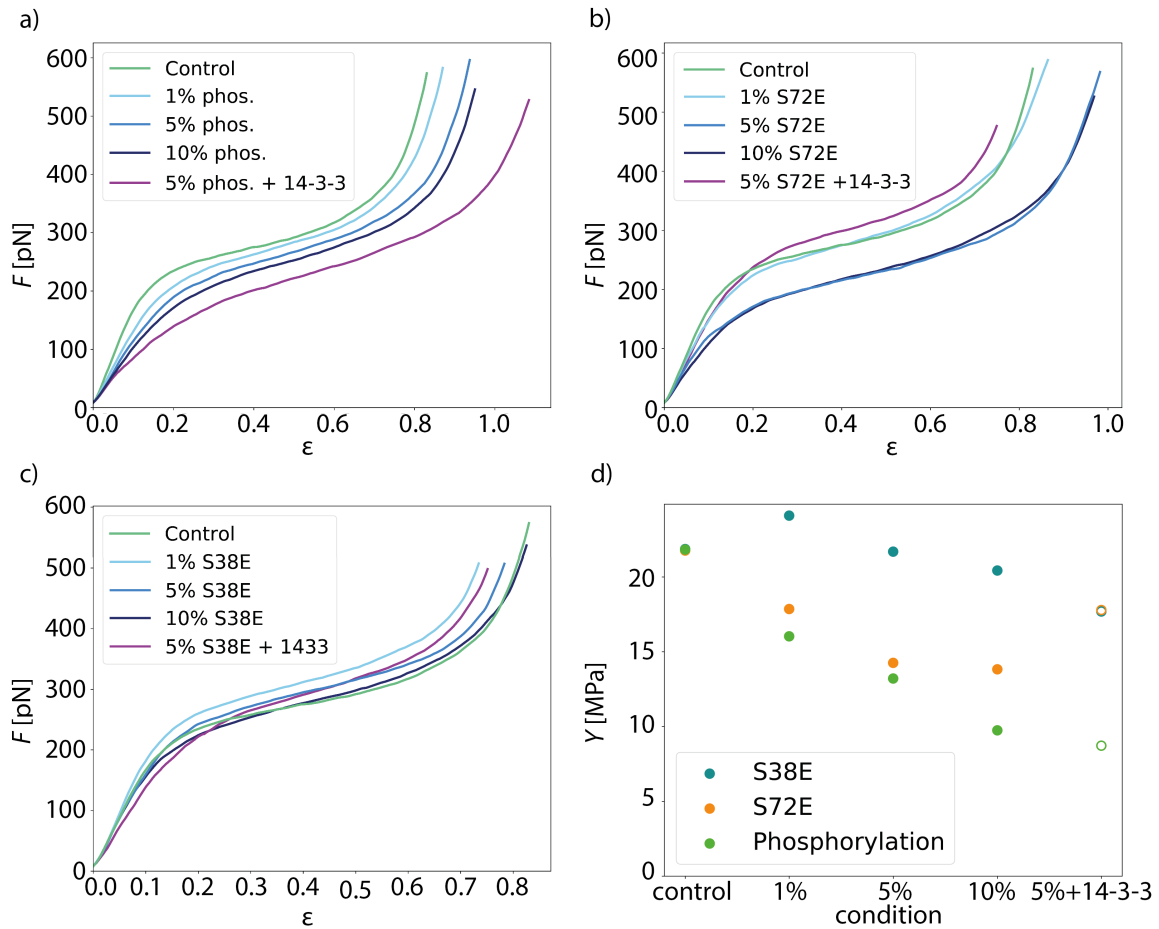
Figure 5.2: *Additional negatively charged amino acids soften vimentin filaments. a) Mean force-strain curves for partially phosphorylated filaments: control (unphosphorylated, green), 1% phosphorylation (light blue), 5% phosphorylation (medium blue), 10% phosphorylation (dark blue) and 5% phosphorylation with 14–3–3 (magenta). With increasing amount of phosphorylated vimentin incorporated, the filaments become softer; the effect is even more pronounced in the presence of the protein 14–3–3. b, c) Mean force-strain curves for the phosphomimicry data. The color code for the individual conditions is the same as in a. b) The mean curves for the phosphomimetic mutant S72E show a similar trend as the phosphorylation data except for the filaments incubated with 14–3–3. c) The mean curves of the phosphomimetic mutant S38E do not show a systematic softening regardless of whether the filaments were incubated with 14–3–3 or not. d) Comparison of the different data sets. The Young's modulus Y, which is a measure of the filament stiffness, is shown in dependence of the amount of phosphorylated or phosphomimetic protein. The phosphorylation (green) and the S72E data (orange) show a softening with increasing phosphorylation or phosphomimicry, whereas the S38E data (blue) remain fairly constant. The Young's moduli for filaments with additional 14–3–3 are depicted as open symbols, as these are only an estimate using the radius of the 5% condition instead of the actual radius that cannot be measured by SAXS.*

Upon phosphorylation of vimentin by PKA, several amino acids are modified. To determine these sites, we perform an LC-MS (liquid chromatography mass spectrometry) analysis. Fig 5.3a shows that phosphorylated sites are dispersed throughout the whole protein, but the most abundant ones ($\log_2(I) > 0$, red lines) are all found in the head region of vimentin. This is in agreement with the head domain of vimentin being a serine rich region and containing multiple motives required for kinases [145]. Strikingly, the positions S71 and S72 are always phosphorylated simultaneously and show the highest degree of phosphorylation. Hence, we speculate that these two positions are the main phosphorylation sites, whereas all other positions occur only sporadically and therefore differ from monomer to monomer. We employ phospho-mimicry to investigate the effect of defined phosphorylated sites and choose two of the most abundantly phosphorylated sites that also occur *in vivo*, S38 and S72 [31]. We perform the same force-strain measurements as described above. For the mutant S72E, we observe a similar trend as in the phosphorylation data including enhanced softening, see Fig. 5.2b, green to dark blue. On the contrary, Fig. 5.2c, green to dark blue, shows filaments containing the mutation S38E and no systematic trend is observed. The individual data sets are provided in Appendix Figs. A.16 and A.17. When comparing these three different conditions, *i.e.* phosphorylation, mutation S72E and mutation S38E, we observe that the Young's modulus, and therefore the filament stiffness, decreases with an increasing amount of phosphorylation (green) and mutation S72E (orange) but stays fairly constant for the mutation S38E (blue), see Fig. 5.2d. These results suggest that the phosphorylation at position S72 influences the filament mechanics whereas at position S38 it does not have any effect. As the filament radius is a critical parameter for calculation of the Young's modulus, we perform small angle X-ray scattering (SAXS) experiments to determine the radius of gyration of the cross-section R_c, see Fig. 5.3c-e. No changes in radius are observed. The individual SAXS curves are shown in Appendix Figs. A.18-A.20.

To explain the softening of vimentin filaments with increasing amount of phosphorylation, we consider previous studies that have shown neighboring dimers to be coupled by electrostatic interactions between specific positively charged amino acids in the head, namely R23, R28, R36 and R45, and the negatively charged coiled-coils [12, 16, 146] as sketched in Fig. 5.4b. When vimentin becomes phosphorylated, the positive charges of the head domain are flanked by negative charges of the phosphorylated amino acids as shown in Fig. 5.4a, which diminishes the electrostatic attraction between the head and the coiled-coils. This observation raises the question
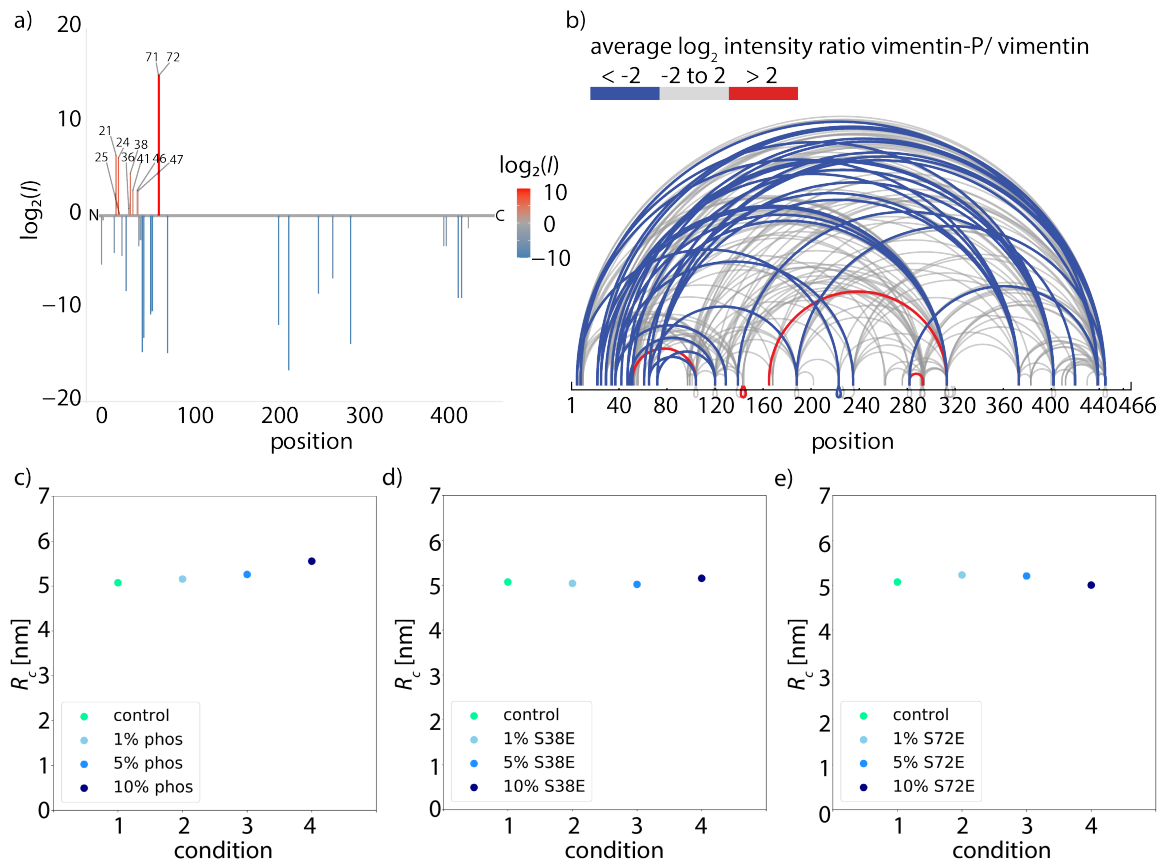
Figure 5.3: *Structural changes caused by phosphorylation. a) Determination of phosphorylated sites in vimentin. Phosphorylated peptides are determined by LC-MS and the degree of phosphorylation of all identified sites is plotted using the $\log_2$ ratios of the LC-MS intensities of phosphorylated over unphosphorylated peptides (intensities I). Identified phosphorylation sites and the numbers of amino acids are listed. The color code represents the degree of phosphorylation of all identified phosphorylation sites. b) Mass spectrometry analysis of cross-linked tetramers. The ratio of the amount of cross-links found in the phosphorylated condition and the unphosphorylated condition is calculated. Linked amino acid positions within a tetramer are indicated by loops and the ratio of cross-links between the phosphorylated and unphosphorylated vimentin tetramers is shown by the color code. Blue loops show a decreased amount of cross-links in the phosphorylated condition, gray loops show no change in the ratio of cross-links between phosphorylated and unphosphorylated condition and red loops show an increase of cross-links in the phosphorylated condition. c)-e) SAXS experiments to analyze the influence of phosphorylation or phosphomimicry on the filament radius. c) Radius of gyration of the cross-section R_c for the different conditions with the control measurement (green), 1% phosphorylation (light blue), 5% phosphorylation (medium blue) and 10% phosphorylation (dark blue). The radius shows no change for the different conditions. d) Radius of gyration R_c for the different conditions with the control measurement (green), 1% S38E (light blue), 5% S38E (medium blue) and 10% S38E (dark blue). The radius shows no change for the different conditions. e) Radius of gyration R_c for the different conditions with the control measurement (green), 1% S72E (light blue), 5% S72E (medium blue) and 10% S72E (dark blue). The radius shows no change for the different conditions.*

of whether the shift in filament stiffness can be explained by weaker coupling. There-fore, we run Monte-Carlo simulations to understand how the coupling of dimers affects the force-strain curves of vimentin by extending the model from Refs. [50, 51] as described in detail in the SI. We model a vimentin monomer by including the α helices in the rod domain as the spring constant κ_α and as elements, which extend in length at a certain force, thereby transitioning to an unfolded state u [50, 51, 55]. The model in Ref. [51] assumes a strong coupling *within* dimers, tetramers or any other subunit of the ULF and weaker coupling *between* these subunits. In that work, the force-strain curves of filaments with smaller coupled subunits exhibit a lower plateau than the force-strain curves of filaments with larger coupled subunits. As demonstrated in Ref. [52], the model can also explain different maximum strains of filaments in different conditions either by a different number of α helices which unfold or a different extension of single α helices. Yet, this previous model does not explain a pronounced decrease in Young's modulus as observed here. We thus supplement the model from Ref. [51] by spring constants κ_{bt}, which represent bonds between tetramers, and κ_{bd} for bonds between dimers within the tetramer. In case of more phosphorylated monomers in the filament, the filament subunits do not interact as strongly as without phosphorylated monomers because the additional negative charges repel each other. Thus, not all bonds between tetramers and dimers can form, so that the spring constants κ_{bd} and κ_{bt} do not contribute to the overall spring constant and the filaments get softer as shown for the simulated force-strain curves in Fig. 5.4d. Consequently, the initial slope of the force-strain curves decreases with more phosphorylated monomers as shown in Fig. 5.2c.

Our results show that the negative charge at position S72, in particular, has an effect on filament mechanics: the phosphomimetic mutant shows a very similar trend compared to the phosphorylation data (Fig. 5.2d). Indeed, this position is also found to be the mayor phosphorylation site (see Fig. 5.3a). By contrast, an additional nega-tive charge at position S38 has no effect on the filament mechanics. Therefore, we conclude that a decreased coupling around position S72 is crucial for the shift in mechanics whereas a decreased coupling at position S38 has no effect.

We confirm these numerical findings with mass spectrometry cross-linking exper-iments. When comparing cross-linked phosphorylated vimentin tetramers and unphosphorylated vimentin tetramers in Fig. 5.3b, fewer cross-links are found in the phosphorylated state, blue lines. All individual cross-linking positions can be found in Appendix Fig. A.21. This supports our proposal that there are decreased interac-tions between neighboring dimers in phosphorylated vimentin which indicates that
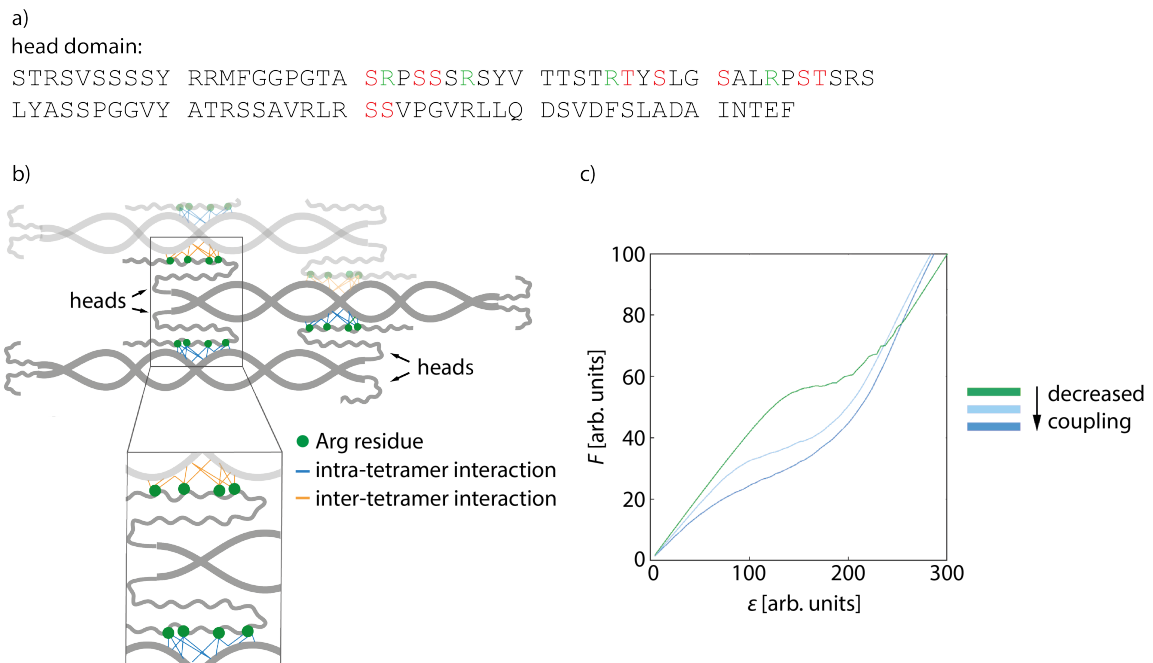
a)
head domain:
STRSVSSSSY RRMFGGPGTA SRPSSSRSYV TTSTRTYSLG SALRPSTSRS
LYASSPGGVY ATRSSAVRLR SSVPGVRLLQ DSVDFSLADA INTEF

b)

heads

heads

● Arg residue
— intra-tetramer interaction
— inter-tetramer interaction

c)

decreased
coupling

Figure 5.4: *Softening of phosphorylated filaments is due to decreased lateral interactions. a) The amino acid sequence of the head domain of vimentin with positively charged amino acids (green) and phosphorylated sites (red). b) Sketch of a vimentin tetramer. The positively charged amino acids in the head domain (green dots) interact with the negatively charged coils of the neighboring dimer. Intra-tetramer interactions are depicted in blue, the neighboring tetramer is illustrated in light gray and inter-tetramer interactions are shown in orange. c) Results of numerical model for the softening of the filaments due to decreased lateral coupling. The influence of decreased coupling is shown in the force-strain plot where the completely coupled system is shown in green and the lateral coupling is decreased from light blue to dark blue.*

the lateral coupling of dimers is reduced. Despite these decreased interactions, we do not observe an increase in filament radius for increasing amount of phosphorylation, see Fig. 5.3c-e. We speculate that the softening effect due to phosphorylation is reversible when the phosphate group is removed again by phosphatases and filaments would recover their initial stiffness.

Besides the fact that phosphorylation modifies the protein itself, it also creates binding sites for other proteins, such as 14–3–3 in the case of phosphorylated vimentin [27]. This raises the question of whether the binding of the protein 14–3–3 to phosphorylated vimentin also has an effect on the mechanics and we perform optical trap measurements of the vimentin/14–3–3 complex. We confirm the interaction between vimentin and 14–3–3 by performing a streptavidin pulldown assay as shown in Appendix Fig. A.22. Fig. 5.2d, open green circle, shows that for phosphorylated filaments the interaction with 14–3–3 softens the filaments even more. By contrast, the original stiffness of the unphosphorylated filaments is recovered for the mutant S72E, Fig. 5.2d, open orange circle, and we observe only a slight influence of 14–3–3 for the mutant S38E, Fig. 5.2d, open blue circle. The individual curves for these experiments are provided in Appendix Fig. A.23. We show that 14–3–3 binds to the phosphorylated sites in the head domain of vimentin, as confirmed by cross-linking the complex and analyzing it with mass spectrometry, see Appendix Fig. A.24. Assumedly, because of this interaction and the similar size of 14–3–3 compared to vimentin, it forces vimentin subunits further apart and thus enhances the decoupling and softening of vimentin filaments. Mostly, vimentin is cross-linked to position 78 of the amino acid sequence of 14–3–3 as shown in Appendix Fig. A.24. By contrast, we cannot unambiguously determine the cross-linking position in the amino acid sequence of vimentin. However, our data show that the amino acids S38 and S72 in vimentin are not the binding sites for 14–3–3 as the complex of the two proteins is retrieved after phosphorylation of the phosphomimetic mutants as confirmed by cross-linking the complex, see Appendix Fig. A.25. Additionally, we find that no complex is formed between 14–3–3 and the phosphomimetic mutants S38E and S72E. The corresponding SDS gel is shown in Appendix Fig. A.25. Despite this lack of complex formation between 14–3–3 and the phosphomimetic mutant S72E, we observe a stiffening of the filaments upon addition of 14–3–3, indicating some kind of interaction between the proteins, such as electrostatic interactions. Such electrostatic interaction could possibly diminish the effect of the negative charges and thus lead to a recovery of the initial stiffness. Taking these results together, we propose that 14–3–3 protects the protein from phosphatases by binding to strategic phosphorylated sites as suggested

in Ref. [147]. Due to the large size of the protein 14–3–3, it sterically hinders the phosphatases, which can reverse the effect of the protein kinases, from binding to neighboring amino acid positions within the vimentin monomer. Thereby the protein 14–3–3 could be able to keep the vimentin filaments in the soft state for extended times, which might be important for *in vivo* situations.

Previous studies have shown that increased vimentin phosphorylation is required for efficient cellular migration [148] and that it is relevant in metastasis [149, 150] which may be linked to a softer vimentin network and therefore render the cells more deformable. In general, phosphorylation controls the assembly and disassembly dynamics of vimentin [31] and in particular the phosphorylation of vimentin leads to disassembly. Phosphatase activity enables recovery to assembled filaments. If 14–3–3 binds to phosphorylated vimentin and inhibits the phosphatase activity, vimentin remains in the phosphorylated state. Such an effect would slow down the assembly dynamics, which is, however, crucial for cell adhesion, migration and signaling [151]. In addition, the vimentin/14–3–3 complex builds a larger ensemble with the phosphorylated protein beclin1, which then promotes tumorigenesis [152]. It was already suggested that vimentin might be a key regulator of tumorigenic pathways as this complex, namely 14–3–3, vimentin and beclin1, might prevent the dephosphorylation of the proteins within the ensemble and thereby inhibit antitumor activity in cells [3].

5.1.6 Conclusion

To conclude, we directly show how post-translational modifications, *i.e.* phosphorylation, change the mechanical properties of vimentin filaments: Vimentin filaments become softer with increasing amount of phosphorylated protein within the filament. These findings may help to understand the relation between the role of phosphorylation in cancer metastasis and the pronounced motility of metastasizing cells. The interaction of phosphorylated vimentin with 14–3–3 enhances this softening effect and may even protect the softer state. We suggest that these changes are induced by reduced electrostatic coupling within the ULF due to additional negative charges introduced by the phosphate groups and support this assumption by a physical model. We thus hypothesize that cells are able to fine-tune and adapt their mechanical properties locally and within seconds by modifications like phosphorylation according to specific external requirements.

5.1.7   Acknowledgement

5.2   Influence of Charges on Vimentin Mechanics

In the previous Subchapter 5.1 we concluded that the change in mechanics resulting from phosphorylation can be explained by additional negative charges. To strengthen our hypothesis, we create uncharged mutants of the respective positions S38 and S72. If our hypothesis is true, we don't expect to see a change in mechanics for these mutants. Therefore, we mutate the serine at the positions S38 and S72 to alanine instead of glutamate. In comparison to glutamate, alanine is relatively small and it is not charged and for this reason it is ideal to test our hypothesis. Additionally, creating these specific mutants with alanine instead of glutamate is used as a control for phosphomimetic mutants. The setup for the experiments is identical to the experiments described in Chapter 5.1 and we assemble filaments containing 1 %, 5 % and 10 % of the respective mutant S38A or S72A. The force-strain curves for the mutant S38A and the corresponding filament stiffness can be seen in Fig. 5.5a,c. To determine the filament stiffness, we determine the Young's Modulus Y by performing a linear fit up to a force of 130 pN. Regardless of the ratio of the mutant S38A, the filament stiffness Y stays relatively constant, so the stretching behavior in the linear regime of these filaments does not change. However, the filament stiffness is about 4 MPa softer compared to the control filaments without any mutation. Furthermore, the force of the plateau decreases with increasing ratio of the mutant. The force-strain curves for the mutant S72A show a very similar trend compared to mutant S83A, as shown in Fig. 5.5b,d. The filament stiffness Y stays constant regardless of the ratio of the mutation and is lower compared to the control. The force of the plateau regime shows the same trend as well, even though it is less pronounced. Comparing the filament stiffness of the mutants S38A and S72A in Fig. 5.5e, shows that it is nearly identical for all 3 conditions.

The exchange of the serine at position 38 and 72 to alanine leads to slighter softer filaments, *i.e.* the Young's modulus is lower compared to the control measurements without any mutant. This can be explained by the exchange of the amino acids: serine and glutamate have a similar size and structure and are both charged, but alanine is smaller and uncharged so this can have an effect on the secondary structure and thereby lead to softer filaments. The effect of the softening of the filaments is the same for position 38 and 72 and it is independent of the amount of mutation. This is in contrast to the phosphomimetic mutants, where S72E shows a softening of the filaments and S38E shows no effect on the mechanics.

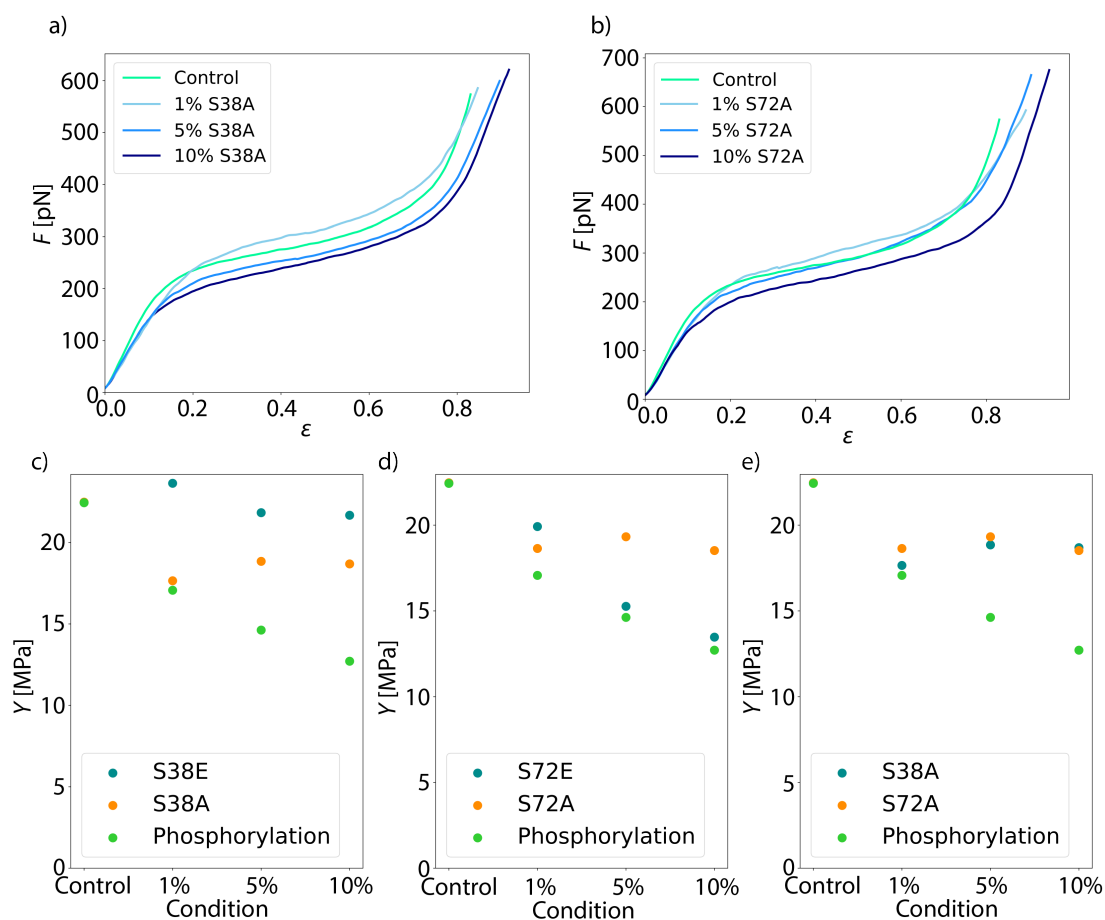These results clearly confirm our hypothesis that the change in mechanics we observe

Figure 5.5: *Mechanical properties of filaments with mutations from serine to alanine at position S38 and S72. a)-b) Force-strain data of vimentin filaments with different ratios of mutation. In green, the control measurement is shown and from light blue to dark blue, the ratio of mutation increases from 1 %, 5 % to 10 %. In a) the mutation S38A is shown and in b) the mutation S72A. c)-d) Filament stiffness for different ratios of mutation. The Young's modulus Y is shown, which is a measure for the filament stiffness. The results for the phophomimetic mutant are shown in blue, for the uncharged mutation from serine to alanine in orange and for the phosphorylation experiments in green. In c) the filament stiffness for S38E and S38A are shown and in d) for S72E and S72A. e) Comparison for the two mutants S38A and S72A and the phosphorylation. The Young's modulus is shown for the different conditions and in blue the results for the mutant S38A are shown, in orange for the mutant S72A and in green for the phosphorylation experiments.*

due to the phosphomimetic mutant S72E from Chapter 5.1 can be assigned to the
negative charge introduced at position S72 and not solely as a result of removing
the serine at that specific position. To summarize, this charge dependent softening
indicates that the softening of vimentin filaments induced by phosphorylation is
caused by the addition of negative charges as the phosphomimetic mutant S72E
shows the same trend in softening.

6

Microrheology on Phosphorylated Vimentin Networks

In the previous chapter we show that PTMs have an influence on single vimentin filament mechanics. However, we do not have single filaments but rather a complex network of vimentin filaments, spanning throughout the cell. In this chapter, we investigate whether changes of the mechanics, induced by phosphorylation, apply to networks of vimentin filaments as well. The method used here to perform passive microrheology is called microparticle tracking.

6.1   Characterization of the Filament Length

First, we characterize the filament length for the two different filament compositions we use for this approach: partially phosphorylated vimentin filaments with a ratio of 10 % phosphorylated monomers, and unphosphorylated vimentin as the control. Both types of filaments are assembled for 72 h at a protein concentration of 0.2 mg/mL at room temperature, and fluorescence images of the filaments are taken at specific times. For every time point, the length of the filaments in the image is measured manually for 550-600 filaments. The distributions of the filament lengths are shown

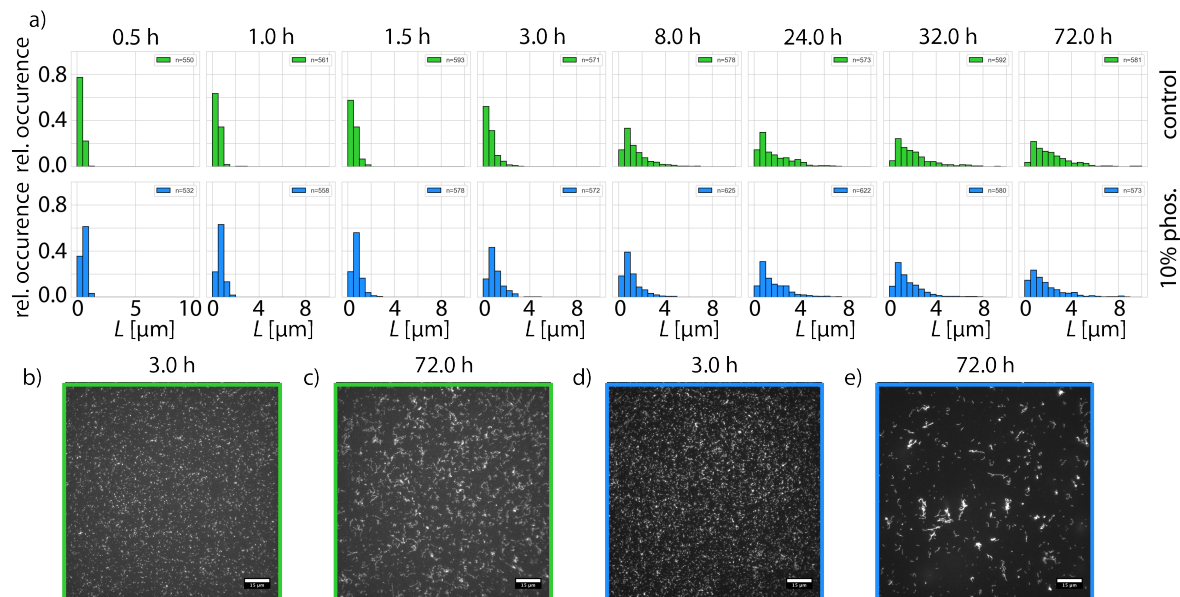in Fig. 6.1a. Comparing the two compositions, we see that the assembly of the control

Figure 6.1: *Filament lengths after different assembly times. a) Barplots, with a bin width of 0.5 µm, of the filament lengths for assembly times of 0.5 h to 72 h. Control filaments without phosphorylation are shown in the upper row in green and phosphorylated filaments are shown in the lower row in blue. b)-c) Fluorescence images of the control filaments after 3 h and 72 h. d)-e) Fluorescence images of the phosphorylated filaments after 3 h and 72 h. Scale bar corresponds to 15 µm.*

(shown in green) is slower within the first 3 h compared to the phosphorylated filaments (shown in blue). This is also visible in the fluorescence images taken after 3 h of assembly in Fig. 6.1b and d. From 8 h to 72 h, the distribution of lengths looks similar between the control and the phosphorylated filaments. However, looking at the assembled filaments after 72 h in Fig. 6.1c and e, we clearly see a difference for the two conditions. The image of control filaments looks very homogeneous, whereas the image of phosphorylated filaments looks more heterogeneous with bright spots, which could be aggregates of filaments. After characterizing the length distributions for single filaments of the two different compositions, we investigate entire networks in the next section.

6.2 Characterization of Measurement Chambers

From the previous characterization of the filament lengths for control and phosphorylated filaments, we obtained that after more than 3 h of assembly, the lengths are comparable. Next, we characterize our measurement chambers used for passive microrheology. As a first step, we test whether the results depend on the height

within the sample at which we record our particle tracks. We perform microparticle tracking for control vimentin networks at a distance of 30 μm, 100 μm and 250 μm from the bottom of the chamber. The total height of the chamber is 500 μm. A sequence of 70,000 images is recorded and the thermal motion of the beads is tracked and analyzed with the Python package *trackpy* as described in Chapter 3. The median MSDs (Δr^2) at three different heights for 24 h of assembly at room temperature as a function of the lag-time τ are shown in Fig. 6.2a. We observe that there is no change
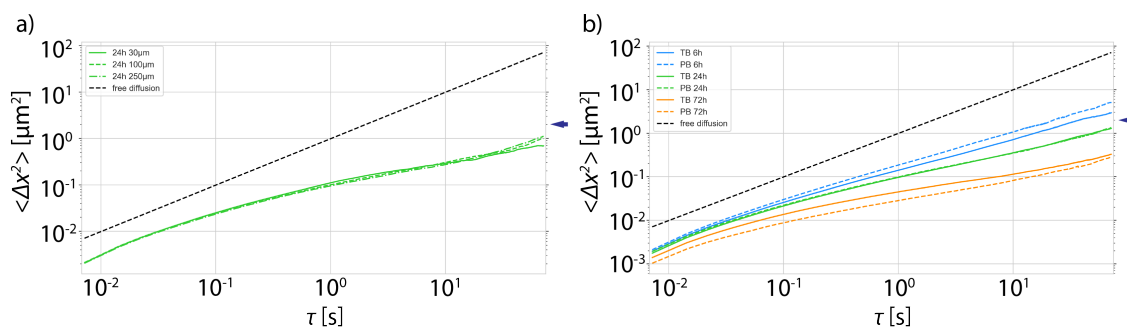
Figure 6.2: *Characterization of the system. a) Median MSD curves obtained at different heights of the chamber for 24 h of assembly. The different heights are indicated by different linestyles: the solid lines corresponds to 30 μm, the dashed line to 100 μm and the dash-dotted line to 250 μm. b) Comparison of network mechanics for two different buffer systems. Measurements in tris buffer are shown as solid lines and in phosphate buffer as dashed lines. The different time points of measurement are as follows: 6 h after assembly are shown in blue, 24 h are shown in green and 72 h are shown in orange. The MSD for free diffusion is shown as the dashed, black line in all plots and the bead diameter of 2μm is indicated by the dark blue arrow on the right side of the plots.*

in the MSD of the particles at the different heights after 24 h of assembly. As a last characterization step, we investigate the influence of the used buffer system on the network mechanics. All experiments on phosphorylated vimentin networks and filaments have to be conducted in tris buffer and therefore the same buffer is used for the control. To be able to compare our results to other studies that conducted experiments on vimentin networks in a phosphate buffer system, as shown in Ref. [103], we examine whether there is a significant difference between those two buffer systems. The results of the measurements are shown in Fig. 6.2b. Three different times of 6 h (shown in blue), 24 h (shown in green) and 72 h (shown in orange) after initiation of assembly are observed and analyzed. After 6 h, the network in the phosphate buffer (dashed line) system is slightly softer compared to the tris buffer system (solid line). After 24 h we do not observe any difference and after 72 h the network in phosphate buffer is slightly stiffer compared to the one in tris buffer. Even though there are minor differences in network mechanics for the two different buffers, we still obtain comparable results.

6.3   Mechanics of Phosphorylated Vimentin Networks

After characterizing our measurement chamber, all following experiments are performed at a height of $30\,\mu m$ from the bottom of the measuring chamber and at three times after initiation of assembly, 6 h, 24 h and 72 h. All networks are assembled at room temperature and with constant slow rotation. First, we record data with phosphorylated filaments from two independent samples to test whether we obtain reproducible results. The comparison of the two samples is shown in Fig. 6.3a. Sam-
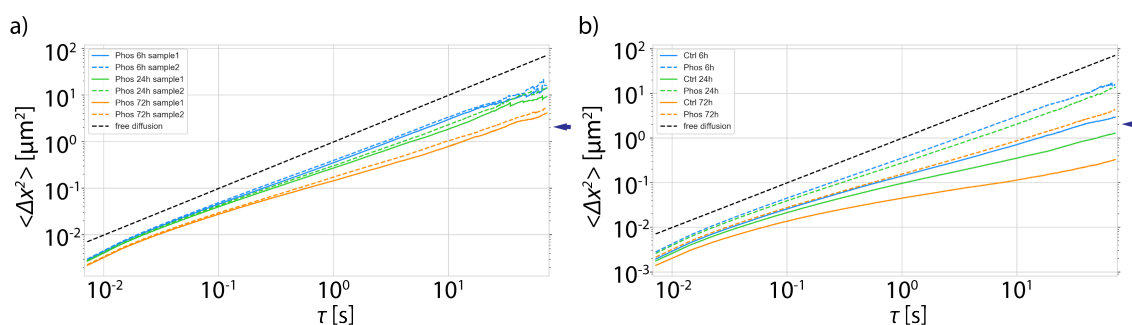
Figure 6.3: *MSDs of phosphorylated vimentin networks. a) Comparison of MSDs at three different times, 6 h (blue), 24 h (green) and 72 h (orange), for two independent samples. Sample 1 is depicted as solid line and sample 2 as dashed line. b) Comparison of phosphorylated networks with unphosphorylated vimentin networks. The color code for the different times is the same and the control measurements are depicted by solid lines and the phosphorylation measurements are depicted by dashed lines. The bead diameter of 2 μm is indicated by the dark blue arrow on the right side of the plot.*

ple 1 (solid lines) shows very similar MSDs compared to sample 2 (dashed lines) for all 3 times observed. Therefore, individual samples of one condition are merged. This merged data set is compared to the unphosphorylated control data, as shown in Fig. 6.3b. For all measurements, microparticle tracking reveals subdiffusive behavior. The curve for diffusive motion is shown as black, dashed line in all plots. Over time, we see a stiffening of both vimentin networks, as the curves flatten for large lag times τ, which corresponds to a decreased motion of the embedded beads. Comparing the two networks at the respective time points, we observe that the networks of phosphorylated vimentin (dashed lines) are always softer than the control networks (solid lines). Here, the last measurement of the phosphorylated network (dashed, orange line) at 72 h has a comparable stiffness to the first measurement obtained for the control measurement (solid, blue line) at 6 h. Therefore, phosphorylated vimentin networks allow more bead movement at all observed times compared to the control network.

6.4   Discussion

In order to interpret the differences of the network mechanics for the two filament compositions, we have to take the filament length and assembly kinetics into account. We observe that for times longer than 3 h after initiation of assembly, phosphorylation does not have an effect on the filament length, compared to control filaments as shown in Fig. 6.1a. However, it is important to note that the protein concentration is set to 0.2 mg/mL and thereby lower compared to the microrheology experiments shown in this chapter which is set to 0.95 mg/mL. This comparably low concentration is used because it allows us to obtain and measure entire single filaments. We can only analyze filaments with a clear start and ending, without loops or other filaments crossing. Therefore, a lower protein concentration is beneficial for this kind of analysis but the concentration clearly has an effect on the assembly kinetics [26]. For the average filament lengths a bin width of 0.5 μm is chosen as smaller structures cannot be distinguished with our imaging setup and analysis. Comparing the filaments 72 h after initiation of assembly, they show clear differences. For the control condition, the filaments look fairly homogeneous, whereas they look much more heterogeneous for the phosphorylated filaments (see Fig. 6.1c and e). The images of phosphorylated filaments show bright spots which might be aggregates of filaments. An explanation of this behavior could be an increased interaction between the more negatively charged phosphorylated filaments and the positively charged glass surface.

To characterize our measurement chamber, we conduct microparticle tracking at different heights of the chamber. This allows us to choose the right height for our experiments and to verify that surface effects do not distort our results. We do not observe any differences for the chosen heights after 24 h of assembly (see Fig. 6.2a). This result allows us to make two estimations: we do not observe any surface effects above 30 μm and we have a homogeneous network throughout the whole chamber. For a last characterization step, two different buffer systems are tested to investigate the influence on network mechanics. We observe only minor differences between the tris and the phosphate buffer system (see Fig. 6.2b). Therefore, our results obtained in tris buffer are comparable to other studies conducted in phosphate buffer.

Comparing independent samples of phosphorylated vimentin networks shows that we obtain very reproducible network mechanics, as shown in Fig. 6.3a. Therefore, samples of the same condition are merged to create the median MSDs. Phosphorylated vimentin networks obtained up to 72 h after initiation of assembly allow more

bead movement compared to the control networks (see Fig. 6.3b). Moreover, within this time, we never observe confinement of the beads within both network, which would be indicated by a plateau of the MSD for large lag-times. For both networks, the maximum MSD values observed for the maximum lag-time indicate that the mesh size of the network is larger then the bead diameter (indicated by the dark blue arrow in Fig. 6.3). As the bead movement in the case of phosphorylated vimentin is mostly diffusive, the mesh size is clearly larger than the bead diameter. In the control condition, the diffusive contribution is reduced, indicating the presence of a network with a mesh size closer to the bead diameter. Thus, we observe a softer network for phosphorylated vimentin as described for single vimentin filaments in the previous chapter. There are additional explanations for the clearly softer networks. First, the structures observed for phosphorylated vimentin filaments in Fig. 6.1 might have an influence on the network mechanics. To test whether these structures occur only due to increased electrostatic interaction with the surface or are also found within the network, the networks should be resolved in future experiments in more detail with other imaging techniques such as AFM or electron microscopy and compared to the control. Second, it is possible that we observe softer networks due to repulsion of the negatively charged vimentin filaments which leads to less dense networks. Most rheological studies on vimentin networks do not consider the evolution of network stiffness over time and the network stiffness is measured 1-2 h after initiation of assembly at a temperature of 37 °C [97, 101, 102]. However, the network stiffness obtained in these experiments is much higher compared to the control measurements presented in this work. In Ref. [102], for example, the protein concentration is comparable at 1.0 mg/mL but a tris buffer with higher ionic strength is used (25 mM Tris-HCl with 160 mM NaCl in contrast to 25 mM Tris-HCl with 50 mM NaCl in our experiments). Both, the ionic strength and the temperature during assembly, have an effect on the assembly kinetics of vimentin. Concerning the temperature, we should be able to gain similar results at room temperature with longer assembly times but we do not reach such stiff networks even after 72 h. It is interesting to test the buffer with the higher ionic strength for future experiments. The buffer with lower ionic strength is chosen to compare the microrheology results with the optical trapping results on single filaments from the previous chapter. For the optical trapping experiments, a buffer with lower ionic strength is needed to reliably obtain single filaments instead of bundles. In addition, comparing our results to experiments with network stiffness measured over time as shown in Ref. [103], further shows that our obtained control vimentin networks are much softer and our MSDs do not reach a plateau for long lag

times τ. The difference between the experiment described in Ref. [103] and the one described here, is the used wall material for the measuring chamber and the height of the chamber. In Ref. [103], double sided tape was used to create a chamber with a height of about 100 µm compared to our chamber created with a silicone isolator with a chamber height of 500 µm. The height of the chamber should not have an influence on the network mechanics as we do not see a change in mechanics depending on the height for distances above 30 µm, as shown in Fig. 6.2a. To exclude the effect of the chamber height and wall material, possible future experiments include thinner silicone isolators and using multiple layers of double sided tape to reach higher chambers.

Nevertheless, the experiments conducted here are consistent for all measured conditions and we clearly see a difference between phosphorylated vimentin networks and unphosphorylated vimentin networks. Thus, we can confirm that phosphorylation does not only lead to a softening of single vimentin filaments but also softens entire networks of phosphorylated vimentin.

7

Summary, Conclusion and Outlook

The ability of eukaryotic cells to resist large strains depends on the cytoskeleton, which is partially composed of IFs. The most abundant IF protein in the human body is vimentin [9, 141]. Vimentin is of high interest in both the biophysical and medical communities as it is directly involved in epithelial-to-mesenchymal transition or the spread of cancer [3]. Although insights on the mechanical properties of vimentin are well understood [49, 50], many mechanisms still need to be elucidated. To understand the underlying mechanical properties of individual parts of the cytoskeleton, studying the mechanics of individual vimentin filaments *in vitro* is an important tool. Optical traps allow for contact-free investigation of the mechanics of single vimentin filaments in pure buffer. In this thesis, highly focused laser beams are used to trap coated beads. The coating of the beads allows for covalent binding of the vimentin filaments. The optical trap is also combined with both a confocal microscope and a microfluidic system. Thus, it is possible to simultaneously acquire confocal images, observe a single filament attach to a pair of beads to ensure successful binding, as well as easily change the buffer conditions.

In this thesis, we used optical traps to study the recovery behavior of vimentin as well as the influence of modification on the mechanics of vimentin. Single vimentin filaments can be stretched to high strains and subsequently recover their initial length

upon relaxation. Previous work suggest vimentin filaments act as shock absorbers of the cell and help maintain their integrity [44, 50]. Therefore, it is important to investigate whether the mechanical properties of vimentin IFs change after applying stress to see, whether they can still function as shock absorbers. Under repeated stretching, vimentin filaments soften and the initial stiffness of the filament cannot be recovered within timescales of up to 60 minutes [55]. We hypothesize that this inability to recover the initial stiffness of the filament arises from a third conformational state that occurs during stretching. For stretching IFs, two conformational states have been observed, namely the α-state and the β-state where the α helices in the rod domain undergo a transition to β sheets [41, 47–49]. We explain our observations by introducing a third state in between these two states which are, presumably, random coils. However, this irreversible transformation upon stretching can be avoided using cross-linkers such as paraformaldehyde and glutaraldehyde. By introducing these cross-linkers to the system, the degrees of freedom are reduced and, depending on the length of the corresponding cross-linker, immediate recovery or recovery within time scales of 45 min is observed.

Moreover, the effect of different loading rates on the recovery behavior is studied. Recent studies have shown that the stiffness of vimentin is loading-rate dependent [49]. This loading-rate dependency means that vimentin is soft when being pulled slowly and much stiffer when being pulled very fast. Therefore, two additional loading rates were chosen such that we have a very slow and a very fast pulling when compared to the speed used in the first experiment of this thesis. The highest loading rate leads to an increase in the ability of vimentin filaments to recover within the observed time scales but full recovery is not achieved with any of these loading rates.

The three different regimes observed while stretching single vimentin filaments are associated to structural changes [46–49]. For example, the linear increase at low strains is associated to elastic stretching of the α-helices whereas the plateau region describes the unfolding of the α helices. We performed multiple stretching cycles within this first linear increase to observe the recovery behavior at low strains. Instant recovery is observed for repeated cycles at low strains. At forces close to the onset of the plateau, *i.e.* above 200 pN, the filaments get softer with each cycle and complete recovery is not possible anymore. We suggest that this is linked to the unfolding of α helices which sporadically takes place at strains close to the onset of the plateau. This result further strengthens our findings that stretching the vimentin filament beyond the plateau region leads to an irreversible transformation of the stretched

and unfolded α helices.

The properties of vimentin IFs do not only change due to mechanical stress but also due to several different modifications which take place after the translation of the protein and are therefore called post-translational modifications (PTMs). One of the most studied PTM in IFs is phosphorylation [35, 143], which is the addition of a negatively charged phosphate group to the amino acids serine/threonine/tyrosine. Phosphorylation of vimentin leads to, for example, disassembly or it can provide binding sites for signaling proteins [31, 32]. It was shown that phosphorylation of vimentin with protein-kinase A leads to several phosphorylation sites, mostly located in the head domain of vimentin [31]. The head domain of vimentin plays an important role during the assembly process [12, 144] and these changes in the molecular interaction could also influence the behavior of fully assembled vimentin IFs. Furthermore, phosphorylation provides additional binding sites for other proteins, such as the protein 14–3–3 which is for example involved in the inhibition of tumorigenesis [28].

To study the effect of phosphorylation on the mechanics of single vimentin IFs, partially phosphorylated vimentin filaments are assembled with fixed ratios of phosphorylated vimentin as full phosphorylation leads to disassembly [31]. These filaments are stretched in an optical trap as described above and we observe a softening of the filaments with increasing amount of phosphorylation. Moreover, when the protein 14–3–3 is bound to partially phosphorylated vimentin filaments, the filaments get even softer. Mass spectrometry analysis revealed that all main phosphorylation sites for vimentin filaments *in vitro* are located in the head domain. To investigate the effect of single phosphorylation sites on the mechanics, stretching experiments with so-called phosphomimetic mutants are performed. Phosphomimetic mutants mimic the effect of phosphorylation by replacing the serine with a negatively charged amino acid, namely glutamate. The mutants are chosen such that they are among the most abundant ones, S38E and S72E. Optical trapping experiments with these filaments reveal no effect for the mutant S38E whereas the mutant S72E shows the same softening effect compared to the experiments with phoshorylated filaments. Incubation of the phosphomimetic filaments with 14–3–3 has no effect on the mechanics. We hypothesize that this softening effect due to phosphorylation can be explained by additional negative charges introduced to the head domain of vimentin. These additional negative charges diminish the coupling effect within tetramers and between neighbouring tetramers. Therefore, the subunits within one ULF do not interact as strongly with each other compared to unphosphorylated vimentin

and due to this diminished interaction, the filaments are softer. We suggest that the protein 14–3–3 further enhances this effect due to its similar size compared to vimentin and by the binding to vimentin, it forces the vimentin subunits further apart and thereby enhancing the decoupling of vimentin subunits.

To further strengthen our hypothesis that the negative charges in the head domain are responsible for the softening, we perform experiments with uncharged mutants of the positions S38 and S72. For both of the mutants we observe that the filament stiffness stays constant regardless of the amount of the respective mutant S38A and S72A. These results strengthen our initial hypothesis that the change of filament stiffness arises from the negative charges introduced by phosphorylation.

Whereas optical traps allow us to measure single vimentin filaments, microrheology is used to study a network of vimentin filaments. With rheological measurements, the deformation and flow of a material in response to an applied stress is described. Here, we use the method of microparticle trapping to obtain the mechanical properties of vimentin networks. To perform passive microrheology, small beads are embedded in the network and the mean-square displacement of the beads due to Brownian motion is observed. This allows us to characterize the network under different conditions, for example for modified vimentin filaments. Therefore, networks of partially phosphorylated vimentin filaments are investigated. First, the assembly kinetics of phosphorylated and unphosphorylated vimentin filaments are compared. For more than 3 h after initiation of assembly, the filament lengths for both conditions are very similar. However, we observe differences in the appearance of the single filaments after long assembly times between 24 h to 72 h. Unphosphorylated filaments look fairly straight and homogeneous, whereas phosphorylated filaments tend to aggregate more. The mechanical properties of networks assembled in two different buffer conditions, phosphate buffer and tris buffer, are very comparable and show only minor differences. Networks of phosphorylated vimentin filaments show a stiffening over the assembled time but are softer at all observed times compared to unsphosphorylated vimentin networks.

To conclude, in this thesis two main topics are investigated. First, the ability of vimentin filaments to recover from repeated stretching. Vimentin softens under cyclic stretching and the original stiffness is not recovered on reasonable experimental time scales for up to 60 min. This result leads to the conclusion that a third conformational state must exist. Besides the two known conformational states, the α-helix and the β-sheet, this third state is presumably a random coil and subunits transforming into this third state are not able to return to their initial state after stretching. However,

this irreversible transformation is avoided when vimentin filaments are incubated with cross-linkers which leads to reduction of the degrees of freedom while stretching the filaments. These findings suggest that previously stretched vimentin filaments are no longer able to protect the cellular integrity. Two possible mechanisms to repair strained vimentin IFs are by subunit exchange along the filament [129–131] or by disassembling and reassembling the filament by, *e.g.*, phosphorylation [31]. As the combination of vimentin filaments with cross-linkers seems to be advantageous for instant recovery of the filament stiffness, this could be a good mechanism for cells that are exposed to high external strains. Indeed, vimentin has been identified as a substrate for transglutaminases which introduce covalent cross-links between different monomers [136, 137]. Transglutaminases target primary amines comparable to the cross-linkers used in this thesis and we therefore hypothesize that they might be able to alter the energy landscape in a similar way to what we could show in our *in vitro* system.

Second, the influence of post-translational modifications, specifically phosphorylation, on the mechanics of vimentin filaments is investigated. We show, that phosphorylation indeed changes the mechanics of vimentin filaments as they become softer with an increasing amount of phosphorylated protein within the filament. This change in mechanics is explained by additional negative charges introduced mainly to the head region of vimentin by phosphorylation. It has been shown that the head domain of vimentin plays an important role during its the assembly process [12, 144]. By introducing negatively charged phosphate groups to the head domain of vimentin, the electrostatic coupling between the head and the coiled-coils of the neighbouring dimers/tetramers gets diminished, which leads to weaker lateral coupling of vimentin dimers/tetramers within the unit-length filament. The effect of negative charges at specific positions in the amino acid sequence of vimentin is investigated by using phosphomimetic mutants. We show that a negative charge at position S72 is important for the change in mechanics as this mutant replicates the softening of the filament whereas negative charges at another position S38 does not have an effect on the mechanics at all. Increased phosphorylation leads to softer vimentin filaments and therefore, this might lead to more deformable cells. These results may help to understand the relation between the role of increased phosphorylation of vimentin in cancer metastasis and the pronounced motility of metastasizing cells. Furthermore, we suggest that cells are able to fine-tune and adapt their mechanical properties locally and, in a fast way, by post-translational modifications like phosphorylation according to specific requirements.

With passive microrheology experiments we can confirm that this softening due to phosphorylation of vimentin is observable in network mechanics as well. Even though there is a lot of potential for further experiments and some open questions, we can clearly see a difference in network mechanics for phosphorylated vimentin filaments compared to unphosphorylated vimentin filaments.

In this thesis we showed that phosphorylation has an effect on the mechanics of vimentin IFs and further investigation of the influence of phosphorylation on entire networks of vimentin IFs are possible to answer the unsolved questions described in Chapter 6. To study the differences in filament length between partially phosphorylated and control filaments for early time points, as shown in Chapter 6, fluorescence fluctuation spectroscopy could be used to compare the assembly process. Another possibility could be using a setup of four optical traps which allows to study the effect of phosphorylation on direct interactions between two partially phosphorylated vimentin filaments. Furthermore, the optical trap setup used in this thesis could be used to study the effect of phosphorylation on other IFs. It would be revealing to find out to what extent these induced changes apply for similar proteins.

A
Appendix

A.1 Vimentin Intermediate Filaments Undergo Irreversible Conformational Changes during Cyclic Loading

This subchapter was published as supplementary information of "Vimentin Intermdiate Filaments Undergo Irreversible Conformational Changes during Cyclic Loading" (Johanna Forsting*, Julia Kraxner*, Hannes Witt*, Andreas Janshoff, and Sarah Köster, Nano Letters 2019 19 (10), 7349-7356, DOI: 10.1021/acs.nanolett.9b02972). Reproduced with permission from American Chemical Society, Nano Letters Copyright 2019 American Chemical Society.
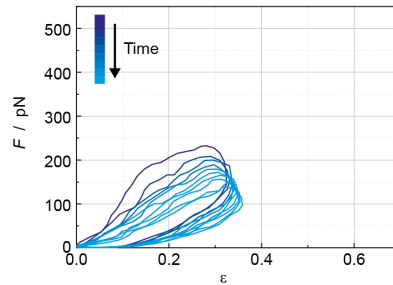
Figure A.1: *Stretching cycle experiment. A vimentin filament is stretched several times to an almost constant distance. For technical reasons, a fully constant distance is not possible.*
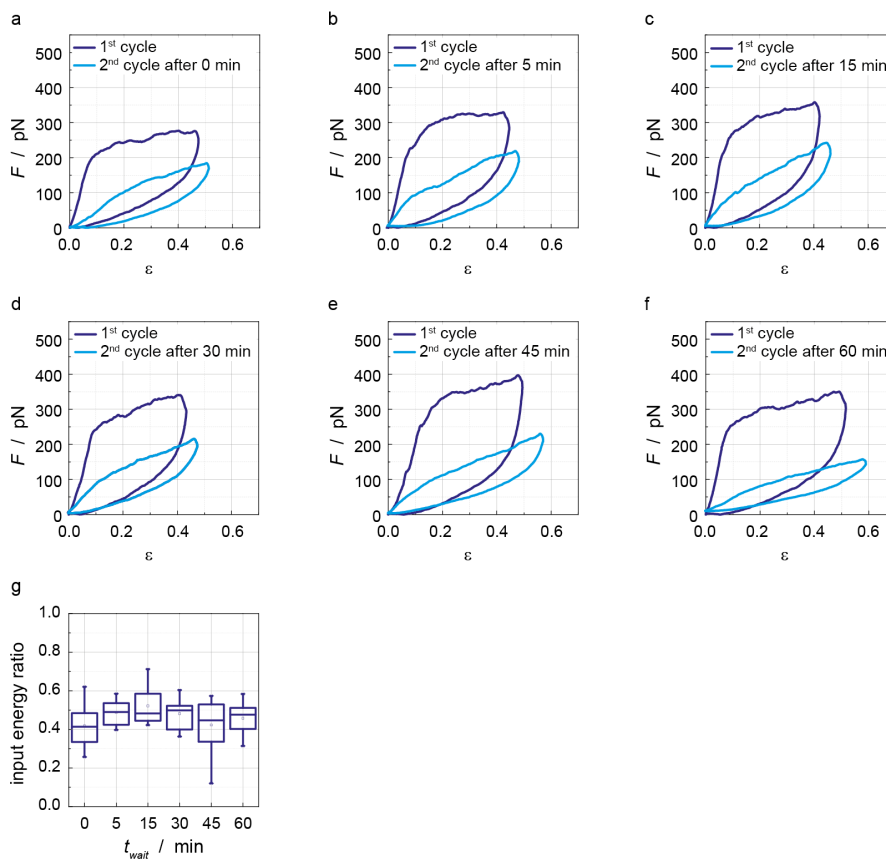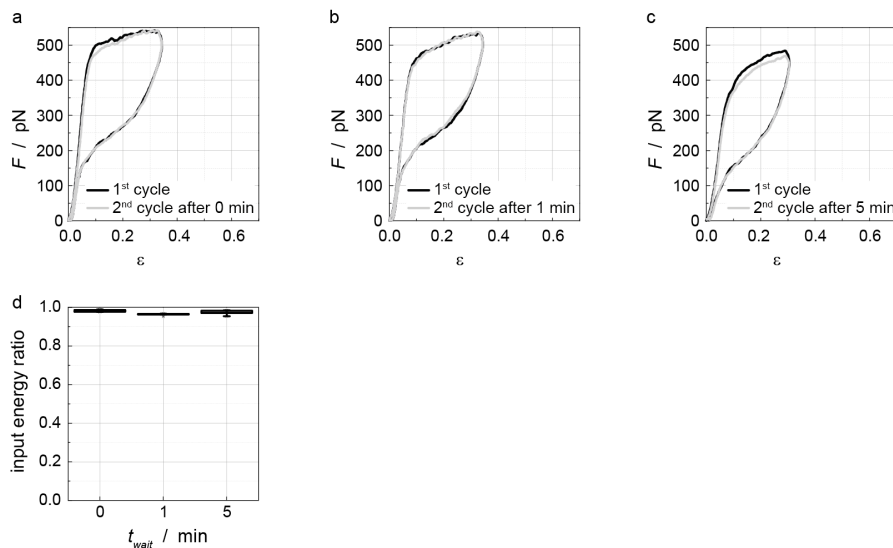

Figure A.2: *Recovery experiments with untreated vimentin filaments. Examples for force-strain data from experiments with different waiting times t_{wait}. **a** $t_{wait} = 0\,min$. **b** $t_{wait} = 5\,min$. **c** $t_{wait} = 15\,min$. **d** $t_{wait} = 30\,min$. **e** $t_{wait} = 45\,min$. **f** $t_{wait} = 60\,min$. **g** Box plot of input energy ratios versus t_{wait}.*
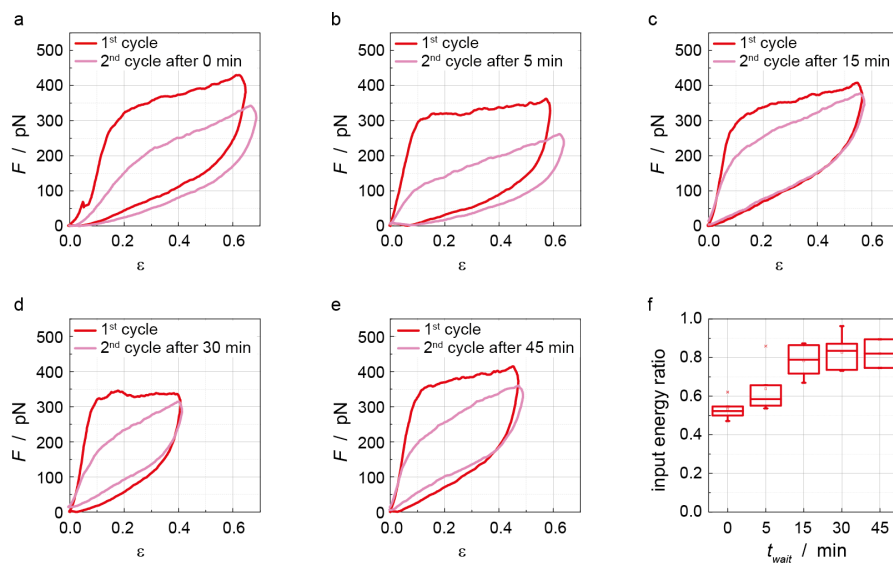
Figure A.3: *Recovery experiments with PFA-cross-linked vimentin filaments. Examples for force-strain data from experiments with different waiting times t_{wait}. **a** $t_{wait} = 0\,min$. **b** $t_{wait} = 5\,min$. **c** $t_{wait} = 15\,min$. **d** $t_{wait} = 30\,min$. **e** $t_{wait} = 45\,min$. **f** Box plot of input energy ratios versus t_{wait}.*

Figure A.4: *Recovery experiments with GA-cross-linked vimentin filaments. Examples for force-strain data from experiments with different waiting times t_{wait}. **a** $t_{wait} = 0\,min$. **b** $t_{wait} = 1\,min$. **c** $t_{wait} = 5\,min$. **d** Box plot of input energy ratios versus t_{wait}.*
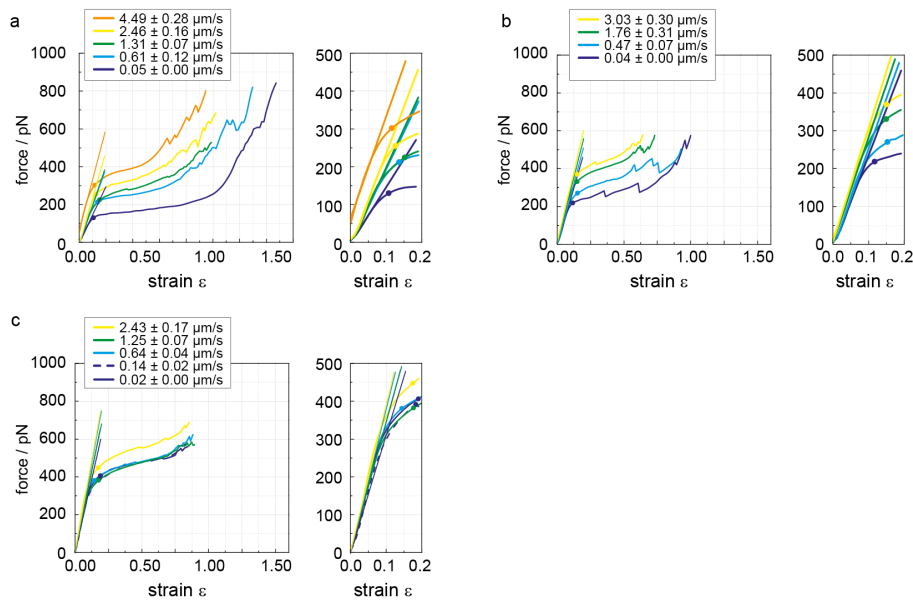
Figure A.5: *Typical force strain curves (left) and magnifications of the elastic initial regime (right) of **a** untreated, **b** PFA-cross-linked, and **c** GA-cross-linked vimentin filaments at different pulling velocities (color-coded) illustrating how the Young's modulus (linear fit) and the plateau force (dot) are quantified.*
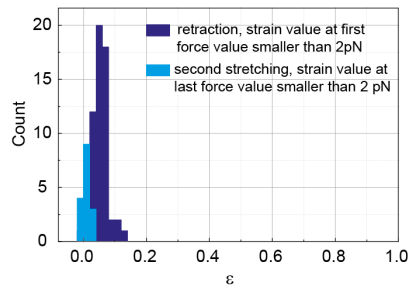
Figure A.6: *Quantification of remaining strain. When we quantify the strain an untreated filament has reached when the measured force during the retraction drops below 2 pN, we gain a distribution of strains with a median at 0.05 and a maximum at 0.12 (dark blue). The strains we observe for the last force value smaller than 2 pN for the second stretching are even smaller values (light blue). The histogram of strains for the second stretching shows a median at 0.007 and a maximum at 0.03, supporting the hypothesis that there is only neglectable plastic deformation in the filament.*
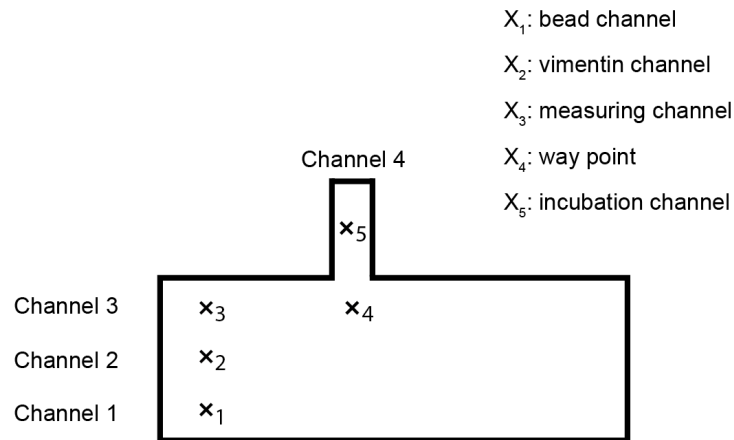
X_1: bead channel

X_2: vimentin channel

X_3: measuring channel

X_4: way point

X_5: incubation channel

Channel 4

$\times_5$

Channel 3 $\times_3$ $\times_4$

Channel 2 $\times_2$

Channel 1 $\times_1$

Figure A.7: *Schematic of the flow cell geometry. The marked positions x_1 to x_5 indicate where the experimental steps were performed. Two beads were captured at position x_1, vimentin filaments were captured at position x_2. Position x_3 was used to bind a single filament to both beads and for performing the actual measurements. Incubation with cross-linking chemicals GA and PFA was performed in channel 4, position x_5, while position x_4 was only a way point for the automated stage drive to reach channel 4 without loosing beads and filaments. Otherwise the system would move the stage the direct way from x_3 to x_5, the traps would leave the microfluidic channel and the beads and the filament would get lost at the channel wall.*
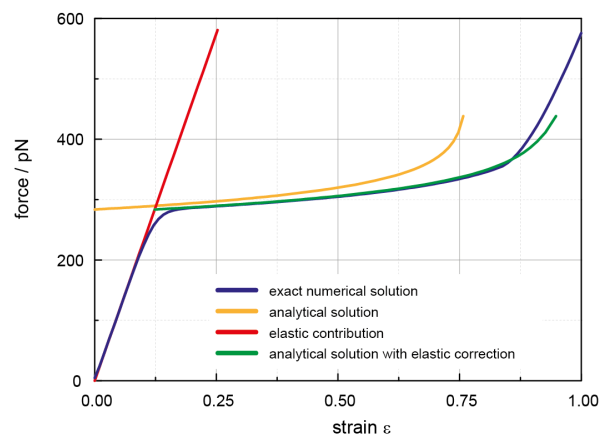
Figure A.8: *Comparison of the exact numerical solution (blue) to the analytical approximation with (green) and without (yellow) elastic correction (red). Although the stiffening at large strains is not quantitatively reproduced, the agreement in the low strain-regime that is used to predict the scaling law is good.*

Vimentin production and purification

Escherichia Coli bacteria (100 μL) were thawed on ice, mixed with 2 μL plasmid solution (concentration 10 ng/μL) per 50 μL bacteria solution and cultured on an agar plate [50]. A single bacteria colony was picked and transferred into 5 mL terrific broth medium (TB, 47.6 g/L (#T0918, Sigma-Aldirch), containing glycerol (8 mL of 99.5 % glycerol (#3873, Sigma-Aldrich) per 1 L TB medium) and ampicillin (Sigma-Aldrich, added at a concentration of 1:1000) and incubated at 37 ° C at 220 rpm for four to six hours. Afterwards, the bacteria solution was transferred to 50 mL TB medium and allowed to grow for another four to six hours. Finally the bacteria were transferred to 1 L of TB medium and cultured over night at 37 °C at 150 rpm.

Bacteria were pelleted with a Beckmann Centrifuge (Beckmann Coulter Avanti J-26 XP, rotor JS5.3) at 5000 g at 4 °C for 25 min. For purification, the pellet was transferred to a cooled Douncer and kept on ice for all subsequent steps. The pellet was dissolved in 16 mL lysis buffer (50 mM TRIS (Carl-Roth GmbH), pH 8.0, 25 % w/v saccharose, 1 mM EDTA (Carl-Roth GmbH), 1 mM Pefabloc SC® (Carl-Roth GmbH), cOmplete™ tablets (1 per 50 mL, Sigma-Aldrich)). 4 mL lysozym (Roche Diagnostics) solution (10 mg/mL in lysis buffer) were added, the mixture was homogenized and incubated on ice for 30 min. 200 μL of 1 M $MgCl_2$ (Sigma-Aldrich), 20 μL RNAseA (10 mg/mL in TRIS buffer, pH 7.5, Roche Diagnostics), 2 μL benzonase (#71206-6, Novagen) and 400 μL 10 % NP-40 (Roche Diagnostics) were added, the solution was again homogenized and incubated for 10 min. 40 mL detergent buffer (200 mM NaCl (Carl-Roth GmbH), 1 % NP40, 1 % DOC (sodium-deoxycholat, Sigma-Aldrich), 20 mM TRIS, 2 mM EDTA, 1 mM Pefabloc SC, cOmplete™ tablets (1 per 50 mL)) were added, the mixture was again homogenized, incubated for 10 min, and then centrifuged for 30 min at 10,000 g and 4 °C using a Beckmann centrifuge (J26XP, rotor JLA 16.250).

The supernatant was discarded and the pellet washed by homogenization using 4 °C cold GII-buffer (10 mM TRIS, 0.1 Vol% TritonX-100 (Carl-Roth GmbH), 5 mM EDTA, pH 8.0) complemented by 40 μL 1 M DTT (1,4 dithiothreitol, Carl-Roth GmbH) and 100 μL Pefabloc SC. The solution was incubated on ice for 10 min and then centrifuged for 30 min using the same parameters as in the step before.

The supernatant was discarded and the pellet washed by homogenization using 4 °C cold GII-KCl-buffer (1.5 M KCl (Carl Roth GmbH) in GII-buffer) complemented by 40 μL 1 M DTT and 100 μL Pefabloc SC. The solution was incubated on ice for 30 min and then centrifuged for 30 min using the same parameters as in the step before.

The supernatant was discarded and the pellet was washed by homogenization using

4 °C cold TE-buffer (10 mM TRIS, 0.1mM EDTA, pH 8.0) complemented by $40\,\mu L$ 1 M DTT and $100\,\mu L$ Pefabloc SC. The mixture was incubated on ice for 10 min and then centrifuged for 25 min using the same parameters as in the step before.

The supernatant was discarded and the pellet solubilized in hand-warm urea buffer. For the urea buffer 12.125 mL 9.5 M urea solution was complemented by $125\,\mu L$ 1 M TRIS, $125\,\mu L$ 0.5 M EDTA and $125\,\mu L$ 1 M DTT, pH 7.5, and the pellet solubilized in as less buffer as possible. After homogenization the solution was finally centrifuged at 20 °C and $100{,}000\,g$ for 60 min, using a Beckmann ultracentrifuge (Beckmann Coulter Optima L90K, rotor Ti70). The supernatant that contains the vimentin was in some cases stored at -80 °C. The final purification by anion and cation exchange chromatography was performed as described in Block et al. [50] without any changes.

Analytical solution for the two-state-model

Here we use an approximate analytical solution of the two-state-model for filament stretching. The full theory and its applicability have been described elsewhere [49, 50, 63]. In brief, every unit length filament (ULF) in the filament is assumed to be able to adopt a shorter and a longer state with a force dependent transition between them. These states do not necessarily need to be identical to defined secondary structures like the α helix or the β sheet, but can be interpreted as a two-dimensional projection of the higher dimensional energy landscape shown in Fig. 4a in the main text. This model gives us the time and force dependent contour length $L_C(t, F)$ of the filament that can be combined with elastic and entropic contributions to calculate the shape of the force-distance curve (for the sake of readability, we will state neither explicit nor implicit dependencies going forward). The approach for the analytical solution is mostly adapted from Burte and Halsey [63]. The key step for the analytical solution is to ignore elastic and entropic effects such that the filament length equals the contour length $L = L_C$. When we neglect the back-reaction to the shorter conformation, which is a good approximation for the extension curve, and do not account for the independent reaction of the separate helices in the vimentin monomer, the rate equation reads

$$\frac{\mathrm{d}N}{\mathrm{d}t} = (N_0 - N)k_0 \exp\left(Fx_u/k_BT\right), \qquad (A.1)$$

with the number of ULFs in the longer state N, time t, the total number of ULFs in the filament N_0, the zero force reaction rate between the shorter and the longer state k_0, the force F, the potential width x_u, Boltzmann's constant k_B and the temperature T. Using the length change of a ULF during the conformational change $\Delta l = \mathrm{d}L/\mathrm{d}N$

we obtain:

$$\frac{\mathrm{d}L}{\mathrm{d}t} = \Delta l(N_0 - N)k_0 \exp\left(Fx_u/k_B T\right) \tag{A.2}$$

$$= L_0(\Delta l/l - \varepsilon_{\text{approx}})k_0 \exp\left(Fx_u/k_B T\right), \tag{A.3}$$

with the length of an ULF l, the initial filament length L_0 and the strain $\varepsilon_{\text{approx}} = N\Delta l/L_0$ (excluding elastic and entropic contributions). If a filament is stretched at a constant velocity, we can set $\mathrm{d}L/\mathrm{d}t = v$. Solving for the force gives us

$$F = \frac{k_B T}{x_u} \ln\left(\frac{v}{k_0 L_0(\Delta l/l - \varepsilon_{\text{approx}})}\right). \tag{A.4}$$

Elastic contributions play a significant role in the force response of filaments and can be introduced via an elastic correction $\varepsilon_{\text{corr}} = \varepsilon_{\text{approx}} + F/k_{\text{eff}}L_0$ using the effective spring constant of the filament k_{eff}. Comparing this approximate solution to the numerical solution shows good agreement at low to intermediate strains (Supporting Fig. S8).

A simple scaling law can be derived from equation A.4 for the force F_P at the onset of the force plateau when the strain is completely caused by elastic deformation, *i.e.* $\varepsilon_{\text{approx}} = 0$. We find

$$F_P = \frac{k_B T}{x_u} \left(\ln(v/L_0) - \ln\left(k_0 \Delta l/l\right)\right). \tag{A.5}$$

This equation can now be used to independently determine x_u and k_0 by performing stretching experiments at different velocities and plotting F_P as a function of the normalized velocity v/L_0 and estimating ε_{max} based on structural data or from the length of the force plateau.

It has been shown previously that the velocity dependence of vimentin stretching could only be reproduced if independent reactions of subsections of the peptide chain were assumed. When we have multiple subunits (for example the three helices that comprise the vimentin monomer) the differential equation A.3 becomes a sum of their respective contributions L_i and we get

$$\frac{\mathrm{d}L}{\mathrm{d}t} = \sum_i^3 \frac{\mathrm{d}L_i}{\mathrm{d}t}. \tag{A.6}$$

This equation cannot be solved without further constrains. However, we can expect that the scaling in equation A.5 still holds, since due to the exponential force dependence the element with the largest x_u will dominate at the onset of the plateau. Therefore, equation A.5 was fitted to the plateau force as a function of the pulling velocity v normalized by the initial filament length L_0.

A.2   Post-Translational Modifications Soften Vimentin Intermediate Filaments

Theoretical Model and Monte-Carlo Simulation

To simulate the force-strain behavior of vimentin IFs, we calculate the spring constants of the modeled elements and the transition rates of possible reactions and run a Monte-Carlo simulation with a self-written Matlab code (MathWorks, Natick, Massachusetts, USA) as in Refs. [50, 51]. We model each monomer consisting of three α helices as one spring with a spring constant κ_α and an element, which can elongate under force to an unfolded state u. To theoretically describe an entire filament, we connect these monomers *via* springs as they are associated in an actual filament: Two monomers are laterally connected to form a dimer, two dimers form a tetramer, and eight tetramers a ULF. To form a filament, 100 ULFs are placed in series and connected *via* springs with a spring constant κ_L, which represents the longitudinal bonds between ULFs. From crystallography [153] and hydrogen exchange [154] experiments, we know that there are specific sites for dimers and tetramers to bind to each other. Therefore, in addition to the theoretical models presented previously [50, 51], we take the links between dimers and between tetramers as connecting springs into account as sketched in Fig. A.26. The spring constant κ_{bt} represents bonds between tetramers (marked in green in Fig. A.26) and the spring constant κ_{bd}

represents bonds between dimers, *i.e.* within tetramers (marked in blue in Fig. A.26). To calculate the total force acting on the filament, we first determine the spring constant of the filament. The spring constant of the ith ULF in the filament depends on the number of intact α helices A_j in this ULF with spring constant κ_α. Upon loading, the α helices open into an unfolded state u, in which the unfolded α helix has the spring constant κ_u. We assume that a ULF consists of $N_P = 32$ parallel monomers [24] and $N_P/4 = 8$ parallel tetramers. The number of tetramers with intact (*i.e.* unfolded) α helices is $\lfloor A_j/4 \rfloor$, thus the number of possible interactions between these tetramers with intact α helices is $\lfloor A_j/4 \rfloor - 1$. Here, we assume that the interaction between the tetramers consisting of (formerly) intact α helices is lost when one α helix unfolds. Intact α helices in a tetramer which contains unfolded α helices are more likely to unfold than intact α helices in a tetramer containing only intact α helices. Thus, we assume that the next unfolding α helix under force is more likely to be located in a tetramer containing already unfolded α helices. For example, if 18 α helices in a ULF are intact, $\lfloor 18/4 \rfloor - 1 = 4 - 1 = 3$ connections between four intact tetramers are left. If another α helix unfolds, we assume that the unfolding occurs in the tetramer with only two intact α helices. We describe a bond between tetramers with the spring constant κ_{bt}. Similarly, we model the dimer-dimer connection within a tetramer with the spring constant κ_{bd}. The number of intact dimer-dimer connections is the same as $\lfloor A_j/4 \rfloor$, because we assume that an unfolded α helix breaks the bonds between two dimers. Thus, the bonds between dimers and tetramers contribute $(\lfloor A_j/4 \rfloor - 1)\kappa_{bt} + \lfloor A_j/4 \rfloor \kappa_{bd}$ to the stiffness of the A_j α helices. Longitudinally, *i.e.* along the filament, we assume "linkers" that connect the individual ULFs as well as the single α helices within one monomer. κ_L represents the stiffness of these linkers, and the linkers and ULFs are connected in series. In case all α helices are unfolded, all monomers are in the unfolded state, which has a spring constant κ_u, *i.e.* the N_P monomers have a total stiffness of $N_P\kappa_u$. Note that as long as there is at least one intact α helix present in a ULF, κ_u does not contribute to the overall stiffness, as these unfolded monomers are longer and thus bear no force. For the fully coupled jth ULF including the connection to the next ULF, we obtain the spring constant κ_j:

$$\kappa_j = \begin{cases} \left(\frac{1}{\kappa_L} + \frac{1}{N_P\kappa_u}\right)^{-1} & \text{for } A_j = 0 \\ \left(\frac{1}{\kappa_L} + \dfrac{1}{A_j\kappa_\alpha + \lfloor \frac{A_j}{4} \rfloor \kappa_{bd} + \left(\lfloor \frac{A_j}{4} \rfloor - 1\right)\kappa_{bt}}\right)^{-1} & \text{for } A_j > 0 \end{cases} \tag{A.7}$$

Here, $\lfloor A_j/4 \rfloor$ is the number of links between dimers in the ULF and $\lfloor A_j/4 \rfloor - 1$ the number of links between tetramers. In case the lateral bonds between tetramers are broken, only the bonds between the dimers within a tetramer remain. Thus, N_C subunits with N_M monomers form a ULF, *e.g.* in the case of 32 monomers per ULF, if the subunits are tetramers, which are not coupled, we obtain $N_M = 4$ and $N_C = 8$. In contrast to the fully coupled ULF described with Eq. A.7, we assume that subunits with only unfolded N_M monomers contribute to the overall ULF stiffness as well, since there are no strong bonds inhibiting the subunit to slide past its original neighboring subunits. The stiffness of the jth ULF with $A_{j,m}$ as the number of intact α helices of the mth subunit in the jth ULF, the number I_j of subunits with only unfolded α helices and the number of dimers coupled *via* κ_{bd} within a subunit $N_d = \lfloor \sum_{m=1}^{N_C} A_{j,m}/N_M \rfloor$ is:

$$\kappa_j = \begin{cases} \left(\frac{1}{\kappa_L} + \frac{1}{N_P \kappa_u} \right)^{-1} & \text{for } \sum_{m=1}^{N_C} A_{j,m} = 0 \\ \left(\frac{1}{\kappa_L} + \frac{1}{N_M \kappa_u I_j + \sum_{m=1}^{N_C} A_{j,m} \kappa_\alpha + N_d \kappa_{bd}} \right)^{-1} & \text{for } \sum_{m=1}^{N_C} A_{j,m} > 0. \end{cases}$$

In the case of dimer sliding, neither dimers nor tetramers couple and $N_d = 0$:

$$\kappa_j = \begin{cases} \left(\frac{1}{\kappa_L} + \frac{1}{N_P \kappa_u} \right)^{-1} & \text{for } \sum_{m=1}^{N_C} A_{j,m} = 0 \\ \left(\frac{1}{\kappa_L} + \frac{1}{N_M \kappa_u I_j + \sum_{m=1}^{N_C} A_{j,m} \kappa_\alpha} \right)^{-1} & \text{for } \sum_{m=1}^{N_C} A_{j,m} > 0. \end{cases}$$

Since all ULFs are connected in series to form a filament, the stiffness of the filament κ_F becomes $\kappa_F = 1/(\sum_{j=1}^{N_E} 1/\kappa_j)$. To obtain the force-strain behavior as in Fig. 4c in the main text, we set the model parameters to the following values: $\kappa_\alpha = 6.5$, $\kappa_{bd} = 7$, $\kappa_{bt} = 7$, $\kappa_L = 60$, $\kappa_u = 20$, $N_E = 100$ and $N_P = 32$. In case of strong coupling in Fig. 4c in the main text, we assume that there is only one large subunit per ULF consisting of 32 monomers. For the less coupled case, we assume tetramers as subunits with $N_M = 4$ and $N_C = 8$ (light blue in Fig. 4c in the main text) and for the least coupled case, we assume dimers as subunits with $N_M = 2$ and $N_C = 16$ (blue in Fig. 4c in the main text). Further parameters are necessary to run the simulation, but they

do not influence the spring constant of a ULF: The free energy difference between the unfolded and folded state $\Delta G = 2\,k_B T$, the normalized length change upon unfolding $\Delta L = 1$ and a factor to ensure in detailed balance $\theta = 0.9$. To complete the calculation of the force-strain behavior, the extension of the jth ULF λ_j is:

$$\lambda_j = \begin{cases} 0 & \text{if for all } m: A_{j,m} > 0 \\ 1 & \text{if for any } m: A_{j,m} = 0. \end{cases}$$

For a fully coupled filament, $m = 1$. The total extension of the filament then is $\lambda_{tot} = \sum_{i=1}^{N_E} \lambda_j$. Since the optical traps pull on the filament with a constant velocity v, the end-to-end distance $x(t)$ at time t is $x(t) = vt$. The force ϕ on the filament becomes

$$\phi = \kappa_F (x - \lambda_{tot}).$$

All closing and opening reaction rates of α helices are updated with the new value of ϕ. The next reaction and time step is determined with the Gillespie algorithm. We repeat the procedure of spring constant calculation, length change, force increase and α helix reaction until we obtain a complete force-strain curve for the strain of interest.

Material and Methods

14–3–3 purification

Recombinant maltose-binding protein (MBP)-tagged protein 14–3–3γ was expressed and purified from *E. coli* strain BL21 Rosetta. For the actual measurements the MBP-tag was removed from 14–3–3. Protein expression was performed in 2 YT media (2YT mix, AppliChem GmbH, Darmstadt, Germany) and induced with 1 mM IPTG for 3 h at 30°C. Cells were harvested and lysed in MBP purification buffer (20 mM HEPES, pH 7.4, 150 mM KOAc, 5 mM Mg(OAc)$_2$, 1 mM EDTA, 1 mM DTT, 1 mM PMSF). Crude cell lysate was centrifuged at 100,000 g for 30 min at 4°C. The supernatant was incubated with 1 mL washed amylose affinity resin (New England Biolabs, Frankfurt, Germany) for 1 h at 4°C under gentle rotation. The bead slurry was transferred to gravity columns and first washed with 3 column volumes MBP purification buffer, pH 7.4, followed by one column volume 1 mM ATP (Carl Roth, Karlsruhe, Germany) dissolved in MBP purification buffer, pH 7.4 and a final wash step in MBP purification buffer, pH 7.4. Bound MBP-tagged protein was eluted with 20 mM maltose elution buffer (20 mM HEPES, pH 7.4, 150 mM KOAc, 5 mM Mg(OAc)$_2$, 1 mM EDTA, 1 mM DTT, 20 mM D-maltose).

Eluted protein was dialyzed over night in MBP purification buffer, pH 7.4. The
MBP-tag was cleaved from the purified MBP-14–3–3 protein with FactorXa enzyme
for 16 h at 25°C according to the supplier's recommendation (Merck MilliPore, Merck
KGaA, Darmstadt, Germany). The cleaved protein was separated by size exclusion
chromatography on an Äkta purifier (GE Healthcare, Freiburg, Germany) and a
Seperdex75 size exclusion column in MBP purification buffer, pH 7.4. Finally, protein
concentrations were measured with a Bradford assay and the purified proteins were
aliquoted and stored at -80°C.

Vimentin filament assembly

To prepare the protein for filament assembly, 200 μL unlabeled vimentin at a con-
centration of 1.3 mg/mL was mixed with 25 μL ATTO647N-labeled vimentin at a
concentration of 0.4 mg/mL resulting in a labeling ratio of 4 %, and dialyzed from
storage buffer (8 M urea, 5 mM Tris-HCl, 1 mM EDTA, 0.1 mM EGTA, 0.01 mM MAC
and 250 mM KCl, pH 7.5) to 6 M urea, 5 mM Tris-HCl, pH 8.4 and then in a stepwise
manner (4 M, 2 M, 1 M, 0 M urea, 30 min for each step) to 5 mM Tris-HCl, pH 8.4 with
an subsequent dialysis step in fresh 5 mM Tris-HCl buffer over night. Afterwards the
protein concentration was adjusted to about 0.2 mg/mL. To initiate filament assembly,
the protein was dialyzed into assembly buffer containing 25 mM Tris-HCl, pH 7.5
and 50 mM NaCl at 37°C over night [107].

Phosphorylation of vimentin

As phosphorylation buffer we used 25 mM Tris-HCl, pH 7.5 containing 50 mM NaCl,
2 mM MgCl$_2$ and added 100 μM ATP (Carl Roth), and protein kinase A (PKA; New
England Biolabs). The amount of PKA was dependent on the amount of vimentin
used, with 1 μL PKA solution per 1 μg vimentin. Vimentin solution and phosphory-
lation buffer were mixed at a ratio of 1:9 resulting in a final vimentin concentration
of 0.11 mg/mL. This mixture was incubated for about 1 h at 37°C and dialyzed into
8 M urea in 5 mM Tris-HCl, pH 8.4 for about 1 h at room temperature. This step was
performed to stop the phosphorylation by inactivation of the PKA. In a next step the
phosphorylated vimentin was mixed at the desired ratios with unphosphorylated
vimentin, which was diluted to the same concentration by adding 8 M urea in 5 mM
Tris-HCl, pH 8.4. This vimentin mixture was then dialyzed as described before from
8 M urea in 5 mM Tris-HCl, pH 8.4 in steps of 4 M, 2 M, 1 M and 0 M urea to 5 mM

Tris-HCl, pH 8.4 and afterwards assembled in 25 mM Tris-HCl, pH 7.5 and 50 mM NaCl at 37°C over night.

Determination of the degree of phosphorylation in tetramers and filaments

To test whether the phosphorylation of vimentin tetramers was successful, phosphorylation analysis gels (Phos-tag Acrylamide AAL-107, FUJIFILM Wako Chemicals Europe GmbH, Neuss, Germany) were used. These gels show additional bands above the actual protein band if the protein is phosphorylated. The phosphorylation analysis SDS gels were produced according to the manufacturer's instructions. Samples were prepared by mixing 13 μL protein with 7 μL sample buffer (150 μL Laemmli SDS sample buffer (Alfa Aesar, Kandel, Germany), 60 μL 1 M DTT), followed by an incubation at 95°C for 5 min. The gel was loaded with 15 μL of each sample and run at a constant current of 40 mA for about 35 min. Afterwards the gel was stained (InstantBlue, Sigma-Aldrich, Munich, Germany) for 1 h followed by several washing steps with water.

To check the incorporation of the phosphorylated monomers within the filament, ultra-centrifugation was performed. The partially phosphorylated vimentin filaments were centrifuged at 34,000 rpm for 10 min (rotor: Fiberlite F50L-25x1.5; centrifuge: Sorvall WX80+ Ultra Series centrifuge, Thermo Fisher Scientific, Kandel, Germany). The supernatant was removed and mixed with sample buffer as described above. The pellet was dissolved in 8 M urea, 5 mM Tris-HCl, pH 8.4, with subsequent dialysis (8 M, 4 M, 2 M, 1 M, 0 M urea in 5 mM Tris-HCl, pH 8.4). Afterwards the dissolved pellet was mixed with sample buffer followed by an incubation at 95°C for 5 min for all samples. The samples were then loaded on an SDS gel and it was run and stained as described above.

Binding 14–3–3 to vimentin filaments

To bind the protein 14–3–3 to vimentin it was first diluted to the same concentration determined in g/L as the vimentin solution. Then, 14–3–3 and assembled vimentin filaments were mixed at a ratio of 1:1 with respect to the concentration in g/L and incubated for 1 h at 37°C. For the optical trap measurements, 30 μL of this solution were diluted by 1 mL assembly buffer (25 mM Tris-HCl, pH 7.5 and 50 mM NaCl).

Verification of vimentin binding to 14–3–3

To test whether the binding of 14–3–3 to vimentin was successful, a streptavidin pulldown assay was performed (adapted from Ref. [109]). Unless otherwise stated, a centrifugation speed of $200 \times g$ for 30 s was used. First 200 μL biotin-labeled vimentin (labeling with biotin-maleimide (Jena BioSciences GmbH, Jena, Germany) was mixed according to the protocol described in Ref. [49]), dialyzed to tetramers and phosphorylated as described above. This biotin labeling of vimentin is necessary for the binding to the beads. The streptavidin-agarose beads (Sigma Aldrich) were washed. To do so, 70 μL beads (for 1 μg of vimentin) were pipetted into a reaction tube (1.5 mL) and washed three times with phosphorylation buffer (25 mM Tris-HCl, pH 7.5 containing 50 mM NaCl, 2 mM MgCl$_2$). In-between the washing steps the beads were centrifuged down for 30 s at 1,700 rpm (MiniSpin F-45-12-11, Eppendorf, Wesseling-Berzdorf, Germany) and the supernatant was discarded. Vimentin was diluted with phosphorylation buffer to a concentration of 0.02 mg/mL and then 50 μL of vimentin solution (total protein amount of 1 μg) was mixed with the beads in the reaction tube. The solution was incubated for 1 h at 8°C on a rotation wheel. During this time, vimentin bound to the beads due to the biotin-streptavidin binding. In order to remove the unbound vimentin, this mixture was pipetted on a column (35 μm pore size, MoBiTec GmbH, Göttingen, Germany), centrifuged down and the flow-through was kept for later analysis. The bead mixture was then again washed twice with phosphorylation buffer and the flow-through was kept. Afterwards, 14–3–3 was diluted to 0.02 mg/mL in phosphorylation buffer containing 0.01 % Triton X-100 and 50 μL were mixed with the beads to which vimentin was bound. This mixture of beads and 14–3–3 was incubated for 1 h at 8°C on a rotation wheel so the 14–3–3 bound to the vimentin on the beads. To remove the unbound 14–3–3, the mixture was centrifuged down, and the flow through was kept for later analysis. The bead mixture was then washed twice with phosphorylation buffer. To remove the bound vimentin and 14–3–3, eluation buffer was used. The eluation buffer consisted of 90 μL SDS loading buffer, 10 μL fresh DTT and 5 μL 100 mM biotin which was mixed and incubated for 10-15 min at 95°C. This eluation buffer was added to the beads, mixed well and incubated for 7 min at 70°C. In the next step the mixture was centrifuged down and the flow through was kept as it should contain the vimentin which bound to the beads and the 14–3–3 which bound to the vimentin. As a last step all the flow through samples were mixed with sample buffer and a phosphorylation analysis SDS gel was run as described above.

Data sets

In total, 43 control measurements with untreated vimentin were performed. For the filaments containing 1 % phosphorylated monomers 38 measurements were performed, for the ones with 5 % phophorylated monomers 41 measurements were performed and for the ones with 10 % phosphorylated monomers 38 measurements were performed. Measurements with the filaments containing 5 % phosphorylated monomers and incubated with 14–3–3 were performed 33 times.

For the mutant S38E, 34 measurements were performed with 1 % of the mutant, 33 measurements with 5 % of the mutant, 30 measurements with 10 % of the mutant and 24 measurements with 5 % mutant incubated with 14–3–3.

For the mutant S72E, 30 measurements were performed with 1 % of the mutant, 30 measurements with 5 % of the mutant, 32 measurements with 10 % of the mutant and 28 measurements with 5 % mutant incubated with 14–3–3.

Mass spectrometry

Cross-linking Experiments

Phosphorylated and non-phosphorylated vimentin was cross-linked in presence of 14–3–3 to determine the interaction sites of the two proteins after phosphorylation. First, the optimal cross-linker–to–protein ratio was determined by using 2.6 μg/2.4 μM aliquots of the complex and the individual proteins and a molar excess of the cross-linker ranging from 20 to 1,000-fold as well as a non-cross-linked control. The cross-linking reaction was performed with freshly prepared bis(sulfosuccinimidyl)-suberate (BS^3, 100 mM stock in DMSO, Thermo Fisher Scientific) for 30 min at room temperature. The reaction was quenched by addition of Laemmli sample buffer and samples were analyzed by sodium dodecyl sulfate polyacrylamide gel electrophoresis (SDS-PAGE) on a 4–12% gradient gel (Invitrogen, Kandel, Germany). After coomassie staining, unique shifted bands were observed for a complex of phosphorylated vimentin and 14–3–3 corresponding to a heterodimer and -tetramer as in Fig. A.24. For the main experiment, samples were cross-linked with a 500- and 1,000-fold molar excess of BS^3 and the shifted bands mentioned above were cut, in-gel digested, and peptides were extracted as described elsewhere [155].

A quantitative cross-linking approach was pursued to examine the structural changes of vimentin caused by phosphorylation. Therefore, phosphorylated, and non-phosphorylated vimentin samples were cross-linked with differentially isotope-labeled

disuccinimidyl suberate (DSS) containing either zero or four deuterium atoms. After 30 min at room temperature, the reaction was quenched with 50 mM Tris, pH 8.1, for 15 min. Phosphorylated and non-phosphorylated vimentin samples cross-linked with the opposite isotopic labels were mixed in equal ratios and the labels were swapped for a second reaction replicate. Subsequently, proteins were precipitated with chloroform and methanol [156] and resuspended in 8 M urea. After complete resuspension, samples were diluted to 4 M urea with 100 mM ammonium bicarbonate and reduced and alkylated with 10 mM dithiothreitol and 55 mM iodoacetamide in 50 mM ammonium bicarbonate, respectively. Samples were diluted to 1 M urea and digested with trypsin overnight in a 1:20 (w/w) ratio. Peptides were desalted with C18 micro spin columns (Harvard Apparatus, Holliston, Massachusetts, USA) and dried in a vacuum centrifuge (Savant SpeedVac Concentrator, Thermo Fisher Scientific).

Phosphopeptide enrichment

Phosphorylated vimentin sample was reduced and alkylated with 10 mM dithiothreitol and 55 mM iodoacetamide in 50 mM ammonium bicarbonate. The sample was digested overnight using trypsin at a trypsin-to-protein ratio of 1:20 (w/w) and then concentrated in the vacuum centrifuge. An aliquot of the sample was subjected directly to LC-MS/MS analysis. For phosphopeptide enrichment, TiO2-beads (10 μm, GL Science) were resuspended in buffer A: 80 % acetonitrile (v/v) 5 % trifluoroacetic acid (TFA, v/v/) 5 % Glycerol (v/v) in water. The bead suspension was mounted onto a plastic pipette tip with a filter paper support forming an approximately 3 mm long chromatographic column. The beads were equilibrated with buffer B (80 % acetonitrile (v/v) 5 % TFA (v/v) in water and 60 %) and buffer A sequentially. The sample was dissolved in 60 μL buffer A and applied onto the column. Next, the column was washed three times with buffer A and buffer B, followed by a wash with buffer B2 (60 % acetonitrile (v/v), 0.1 % TFA (v/v) in water). The retained phosphopeptides were eluted using 0.3 N NH4OH in water (pH 10.5). The sample was acidified using 10 % TFA (v/v) in water and dried in a vacuum centrifuge.

LC-MS analysis

Dried peptides were dissolved in 5 % (v/v) acetonitrile, 0.1 % (v/v) trifluoroacetic acid, and injected in technical duplicate (cross-linked sample) or as a single injection (unmodified and phosphorylated peptides) onto a C18 PepMap100 μ-Precolumn (0.3

x 5 mm, 5 μm, Thermo Fisher Scientific) connected to an in-house packed C18 analytical column (75 μm x 300 mm; Reprosil-Pur 120C18-AQ, 1.9 μm, Dr. Maisch GmbH, Ammerbuch, Germany). Liquid chromatography was operated on an UltiMate 3,000 RSLC nanosystem (Thermo Fisher Scientific). For the cross-linked sample, a linear gradient of 10 to 50 % buffer B (80 % (v/v) acetonitrile, 0.08 % (v/v) formic acid) was applied at 300 nL/min flow rate, and 43 min total gradient duration. Eluting peptides were sprayed into a QExactive HF-X (Thermo Fisher Scientific) mass spectrometer. MS1 scans were performed with a scan range from m/z 350 to 1,600, a resolution of 120,000 full width at half maximum (FWHM), 1×10^6 automatic gain control (AGC) target, and 50 ms maximum injection time. Each MS1 scan was followed by 20 MS2 scans of the most abundant precursors fragmented with a normalized collision energy of 30 and acquired with a resolution of 30,000 (FWHM), 1×10^5 AGC target, and 128 ms maximum injection time. Only charge states from 3+ to 8+ were considered, and a dynamic exclusion of 20 s was set. Vimentin cross-linked with isotopically labeled DSS was analyzed identically with the exception of 30 s dynamic exclusion time.

Similarly, vimentin peptides before and after the titanium dioxide enrichment step were analyzed using a 73 min long linear gradient from 10 to 42 % of the buffer B. The samples were sprayed into a QExactive (Thermo Fisher Scientific) mass spectrometer operated at 70,000 resolution, 1×10^6 AGC target, and 50 ms maximum injection time for MS1 scans; and 17,500 resolution, 1×10^5 AGC target and 54 ms maximum injection time for MS2 scans. Per MS1 scan, 20 peptide precursors with charge states 2-6 were selected for fragmentation using normalized collision energy of 30 %. An isolated precursor ion was excluded from repetitive selection for 25 s.

Data analysis for mass spectrometry

Raw files were submitted to a cross-link database search with pLink 2 (version 2.3.9) [157] against the sequences of human vimentin and 14–3–3 protein γ. The following search parameters were defined: maximum three missed cleavages, cysteine carbamidomethylation as fixed modification, methionine oxidation and phosphorylation of serine, threonine and tyrosine as variable modifications, 4 to 100 amino acids peptide length, 400 to 10,000 Da peptide mass, 10 ppm and 20 ppm precursor and fragment ion mass deviation, respectively, 10 ppm filter tolerance, 1 % false discovery rate cut-off and a cross-linker reactivity towards lysine, serine, threonine and tyrosine.

Database search results were filtered for at least 4 matched fragment ions per peptide in a pair and a minimum score of 1 (negative decadic logarithm of the initial score). Quantitative cross-linking acquisitions were analyzed with pLink1 (version 1.23) [158] after a conversion to mgf format with Proteome Discoverer version 2.1 (Thermo Fisher Scientific). Data were searched with the same parameters except the following: a 25 ppm precursor ion and 10 ppm filter tolerance window around the monoiso-topic and the first, second and third isotopic mass, no phosphorylation as variable modification, 1 % false discovery rate cut-off and no further filtering post-search. Quantification was performed with XiQ [159] by extracting areas under the curve of the first to third isotopic peak of an identification demarcated by a decrease to 10 % signal intensity. Abundance ratios were $\log_2$-transformed and median normalized. The leading sign of ratios was changed for the label-swap replicate. Quantified redundant cross-link-to-spectrum matches were then merged to unique cross-linked residues with a custom R script as described previously [160]. Briefly, median ratios were calculated for each charge state per peptide, which were then summarized to unique peptides as a weighted average. Unique peptides were finally summarized to unique linked residues as median ratios of all supporting peptides. Cross-links were visualized on proteins with xiNET [161] and quantitative values were plotted with Perseus [162].

Analysis of phosphorylated and non-phosphorylated peptides was performed in MaxQuant version 1.6.2.10 [163, 164] using reviewed human protein sequences from Uniprot (02/2019) [165] supplemented with the modified vimentin sequence. Cys-teine carbamidomethylation was set as fixed modification; methionine oxidation, protein N-term acetylation and phosphorylation of serine, threonine and tyrosine were selected as variable modifications. Maximum of two missed cleavage sites and up to five variable modification were allowed per peptide. Other settings were kept default. Peptide intensities were extracted as area under the chromatographic peak using Skyline version 19.1.0.193 [166]. Intensities of phosphorylated peptides were normalized by intensities of the respected non-phosphorylated peptides using a custom R script.

SAXS experiments

Assembly for SAXS experiments was performed in 1.5 mm diameter quartz glass capillaries, wall thickness 0.01 mm (Hilgenberg GmbH, Malsfeld, Germany) for 4 h at 37 °C in a temperature controlled water bath, because assembled protein is

too viscous to be inserted properly into the capillaries. Directly after filling of the capillaries, they were sealed with wax (Hampton Research, Aliso Viejo, CA, USA).

SAXS measurements and data treatment

SAXS measurements were performed using an in-house SAXS setup (Xeuss 2.0, Xenocs, Sassenage, France) equipped with a Genix 3D source (Xenocs), at a wavelength of 1.54 Å (Cu K$_\alpha$ radiation), 50 kV and 600 μA. The beam was focused down to 500 x 500 μm^2. At a sample to detector distance of 1225 mm the scattered signal was collected on a Pilatus3 R 1M pixel detector (981 x 1043 pixels, pixel size 172 x 172 μm^2 Dectris Ltd., Baden, Switzerland). To block the primary beam, a 3 mm-diameter beamstop was placed directly in front of the detector. In total, the signal was recorded for 12 h, divided into 15 min intervals. To obtain the background signal, which is needed for a proper background subtraction, the buffer was measured prior to the protein in the same capillary. As a first step in data analysis, the 2D detector images were azimuthaly integrated and the background was subtracted using self-written Matlab scripts (Matlab2017a, The MathWorks, Natick, MA, USA) based on the cSAXS Matlab base package, available at `https://www.psi.ch/en/sls/csaxs/software`. The data were normalized to the thickness of the capillary, the exposure time, the transmission values, the correction factor and the protein concentration. The integrated intensity $I(q)$ is plotted against the magnitude of the scattering vector q:

$$q = \frac{4\pi}{\lambda} sin(\theta), \tag{A.8}$$

where λ is the wavelength of the radiation and 2θ is the scattering angle. SAXS data are shown in a range from $0.08\,\text{nm}^{-1}$ to $2.00\,\text{nm}^{-1}$, corresponding to real space length scales from 3.14 nm to 78 nm. We analyzed the data by performing a Guinier analysis using the software package PRIMUS[167] (ATSAS, EMBL, Hamburg, Germany) as well as the open source Python library alea[168]. Performing the Guinier analysis, the radius of gyration of the cross-section R_c as well as the forward scattering $I(0)$ can be retrieved using

$$I(q) = \frac{L\pi}{q} I(0) \exp\left\{ \left(-\frac{q^2 R_c^2}{2} \right) \right\}, \tag{A.9}$$

with L as the length of the object. For analysis, the small q-values are fitted up to a limit of $qR_g \leq 1.3$. [169, 170]. R_c can be interpreted as the average distance from the

center of gravity of the particle. In a simplified picture, vimentin filaments can be described as cylinders, for which the relation $R_c = \frac{1}{\sqrt{2}}R$ is valid. However, vimentin filaments have been shown to be partially hollow cylinders[171, 172]. Taking this into account, $R_c = \sqrt{\frac{1}{2}(R_i^2 + R^2)}$ with R_i and R as the inner and outer radii of the cylinder, respectively. This brings the calculated values for the radius of gyration of the cross-section R_c closer to the real radius of the filament R. In addition, it has been reported that the tails of vimentin protrude from the filament itself[9, 173, 174], which leads to an increase of R_c. Therefore, we assume that R_c and R are very similar and thus use R_c from the Guinier analysis to calculate the Young's modulus.

A.2.1 Supplementary Figures
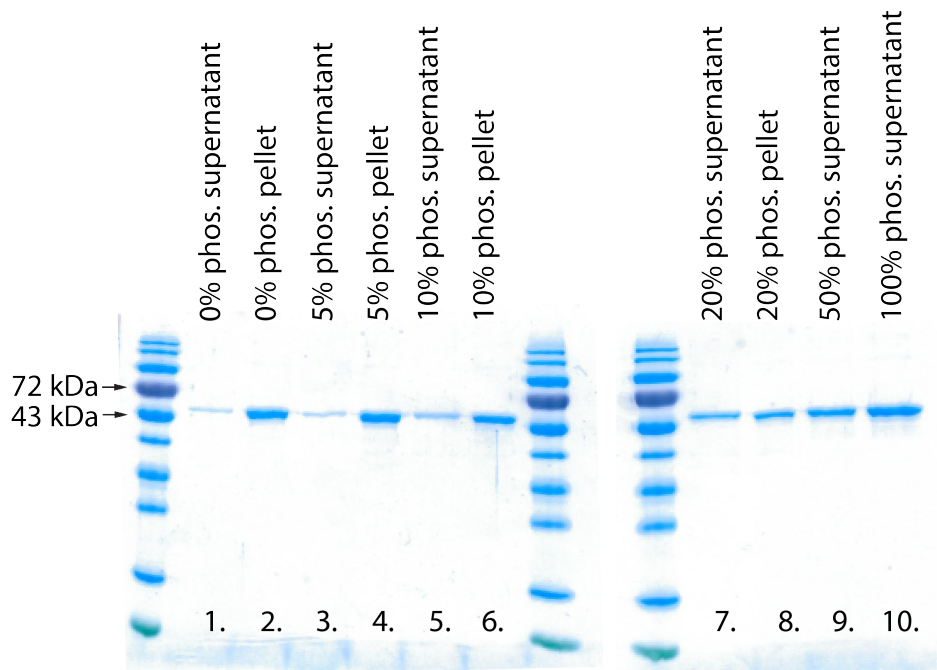
Figure A.9: *Determination of the maximum phosphorylation ratio that still allows for filament assembly. SDS gel of vimentin with different ratios of phosphorylated monomers ranging from 0 % to 100 %. Lane 1 shows the supernatant of vimentin without phosphorylation, lane 2 shows the pellet of the same protein after ultracentrifugation. Lane 3-4 show the corresponding data for vimentin mixture of 5 % phosphorylation, lane 5-6 for 10 % phosphorylation, and lane 7-8 for 20 % phosphorylation. Lane 9 and 10 show the supernatant of vimentin solutions with 50 % and 100 % phosphorylation. The data show that from 20 % phosphorylation on, the amount of protein in the supernatant strongly increases. Therefore, a maximum percentage of 10 % phorphorylated protein was chosen for the experiments described in the main text. It should be noted that the given percentage of phosphorylation refers to the amount of phosphorylated vimentin mixed with unphosphorylated vimentin and the actual percentage is lower as fully phosphorylation can not be achieved.*
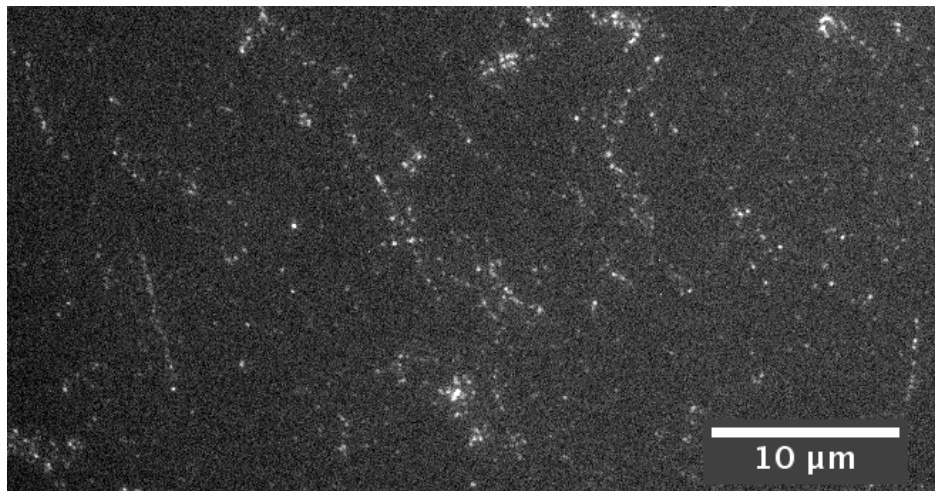
Figure A.10: *Incorporation of phosphorylated vimentin into filaments. Labeled vimentin is phosphorylated and mixed with unlabeled and unphosphorylated vimentin monomers at 5 %, and assembled into filaments. Dotted, but fairly long vimentin filaments can be seen and this ensures that phosphorylated vimentin monomers are incorporated into assembled filaments.*
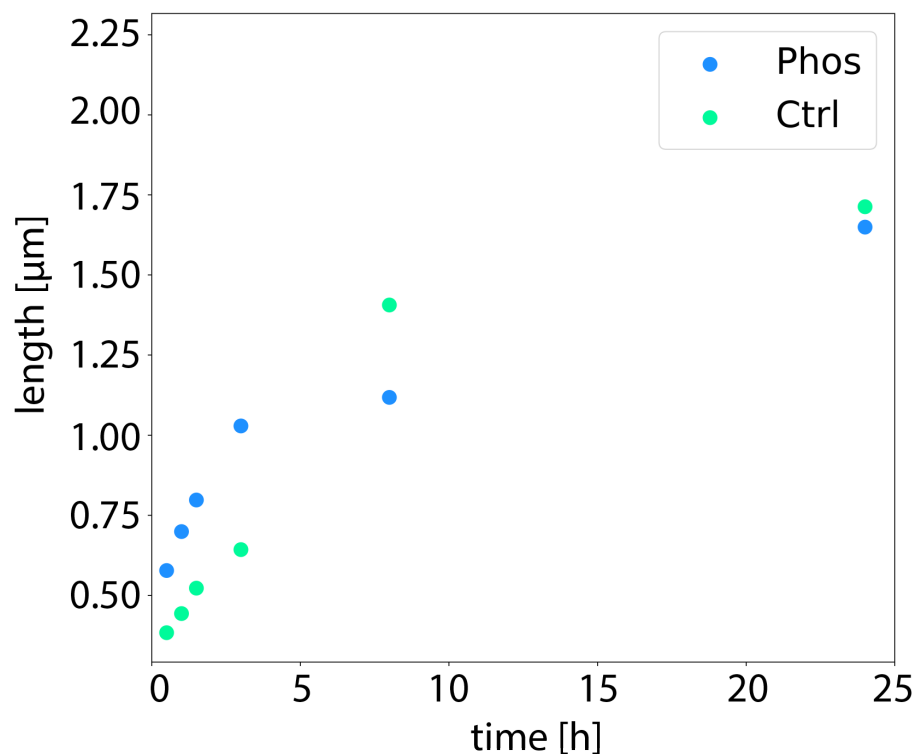
Figure A.11: *Length distribution of the filaments during the assembly. Untreated filaments are shown in green and filaments with 10% of phosphorylation are shown in blue. After the full assembly time of 24 h at room temperature, the average length obtained for both conditions is very similar.*
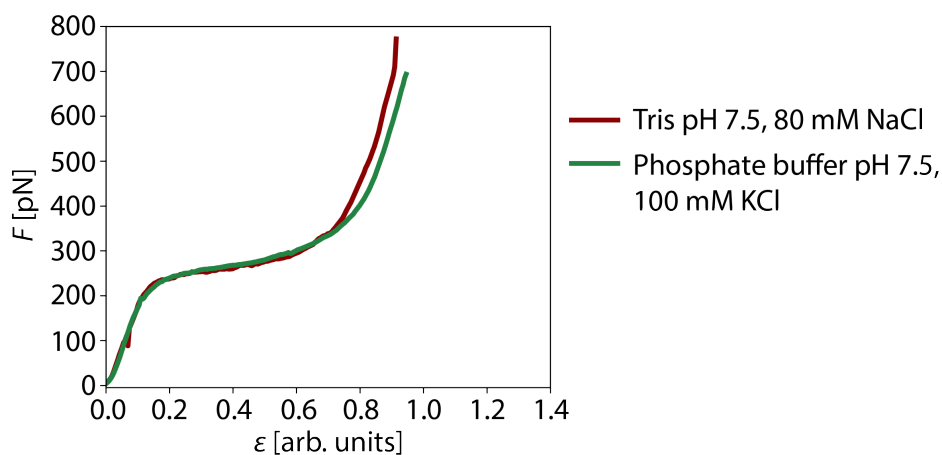
Figure A.12: *Comparison of force-strain curves for vimentin in different buffers. Mean curves for both conditions are shown. In dark red, vimentin force-strain curves in 25 mM Tris buffer containing 80 mM NaCl are shown. In green, vimentin force-strain curves in 2 mM phosphate buffer containing 100 mM KCl are shown. There is no influence of the buffers on the stretching behavior.*
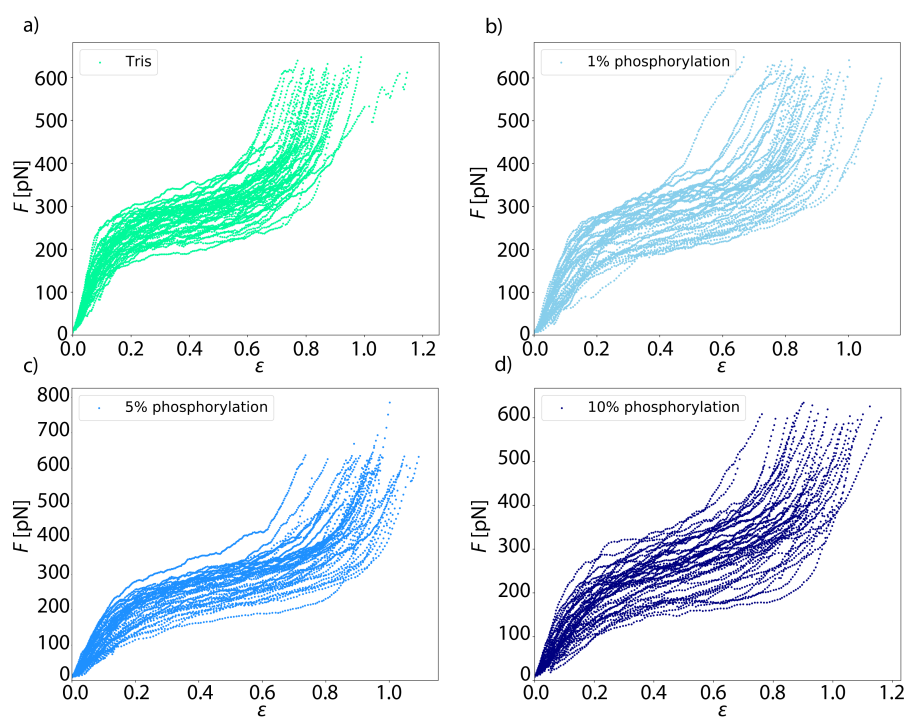
Figure A.13: *Single force-strain curves of all phosphorylation data. The control measurement is shown in green, filaments with 1 % phosphorylation are shown in light blue, filaments with 5 % phosphorylation are shown in medium blue and filaments with 10 % phosphorylation are shown in dark blue.*
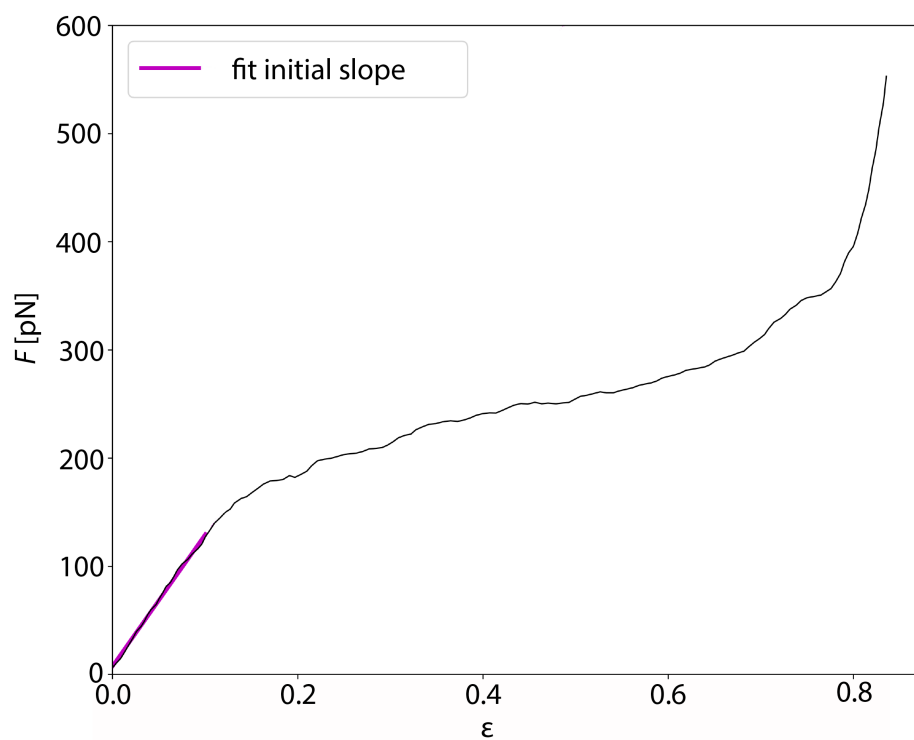
Figure A.14: *Determination of the initial slope used to calculate the Young's modulus. In black, a typical force-strain curve of vimentin is shown. In purple, the fit of the initial slope up to a force of 130 pN is shown.*
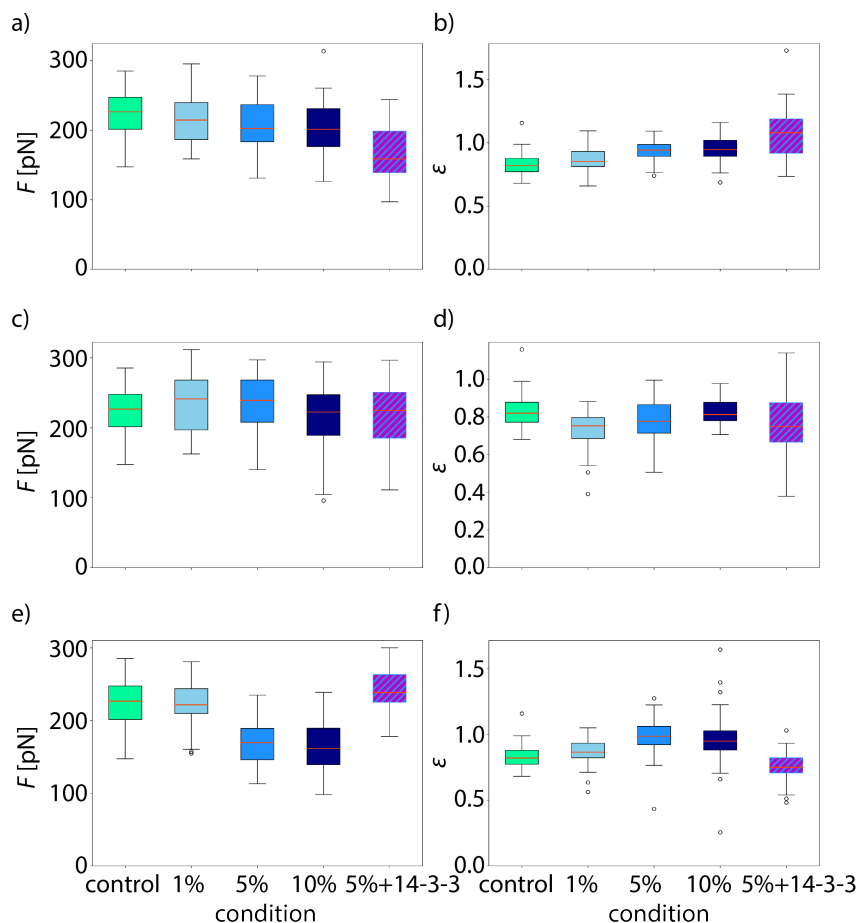
Figure A.15: *Additional analyses of the force-strain curves. a)-b) Vimentin filaments with different percentages of phosphorylation. a) The force F at the start of the plateau. With increasing phosphorylation, the plateau starts at lower forces. b) The maximum strain ε increases with increasing amount of phosphorylation. c)-d) Vimentin filaments with different percentages of mutation S38E. c) The force at the onset of the plateau stays rather constant for the different conditions. d) The maximum strain does not change for the different conditions. e)-f) Vimentin filaments with different percentages of mutation S72E. e) The force at the beginning of the plateau increases with increasing amount of the mutation S72E but increases again when filaments are incubated with 14–3–3. f) The maximum strain increases with increasing amount of the mutation S72E but decreases again when filaments are incubated with 14–3–3.*
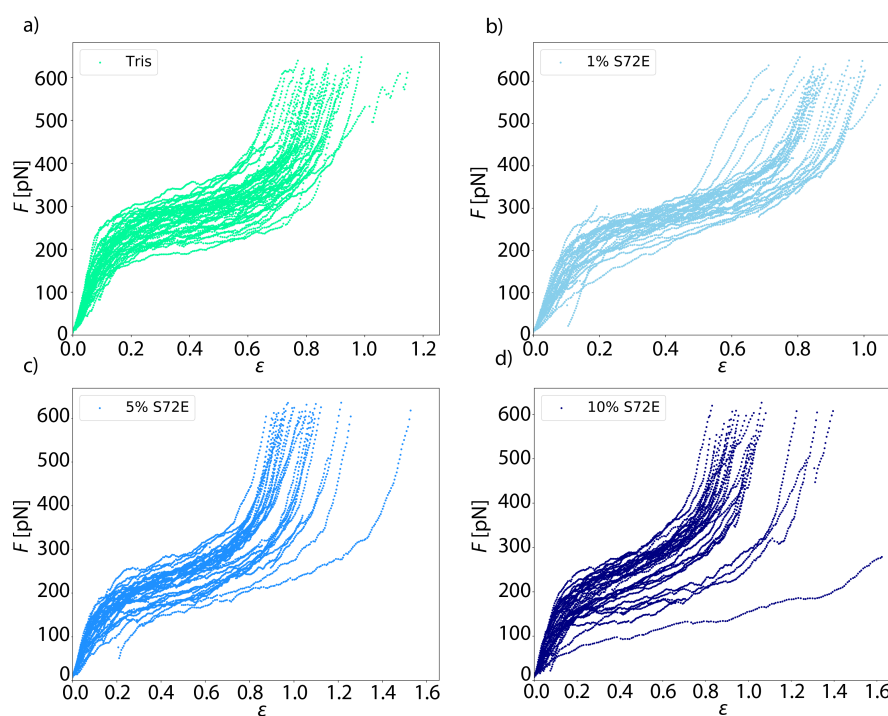
Figure A.16: *Single force-strain curves of all the S72E mutant data. The control measurement is shown in green, filaments with 1 % S72E mutation are shown in light blue, filaments with 5 % S72E mutation are shown in medium blue and filaments with 10 % S72E mutation are shown in dark blue.*
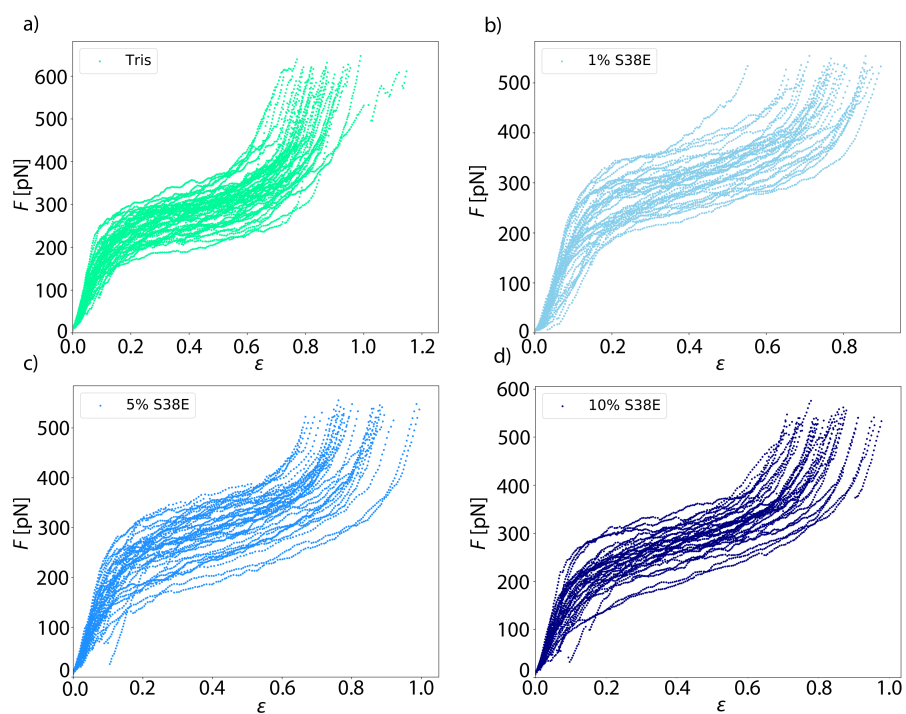
Figure A.17: *Single force-strain curves of all the S38E mutant data. The control measurement is shown in green, filaments with 1 % S38E mutation are shown in light blue, filaments with 5 % S38E mutation are shown in medium blue and filaments with 10 % S38E mutation are shown in dark blue.*
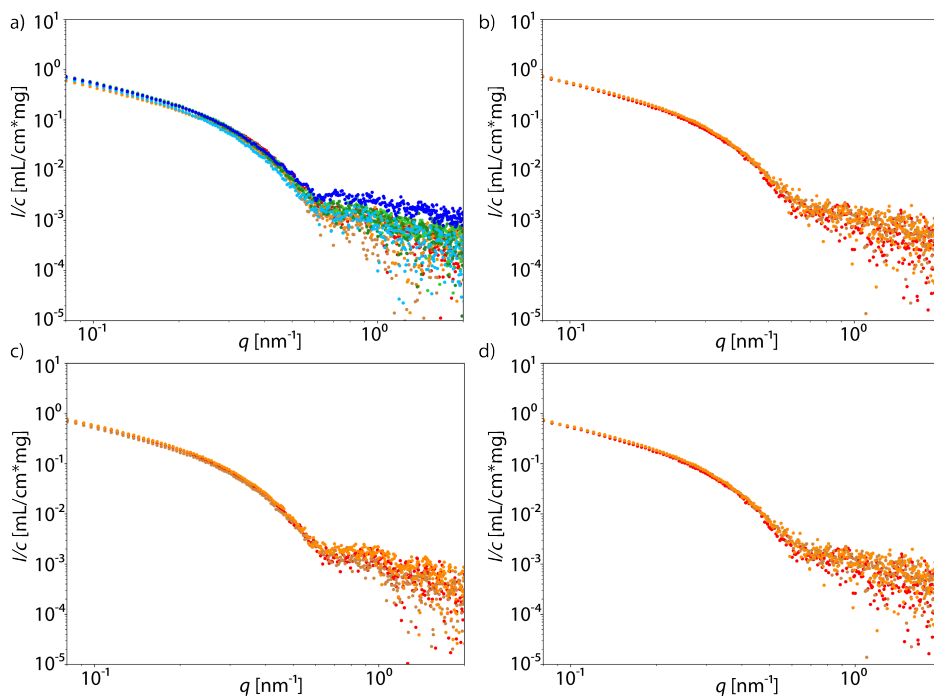
Figure A.18: *Individual SAXS curves of phosphorylated vimentin. Different colors denote individual experiments; a) control measurements with unphosphorylated vimentin; b) 1 % phosphorylated vimentin; c) 5 % phosphorylated vimentin; d) 10 % phosphorylated vimentin.*
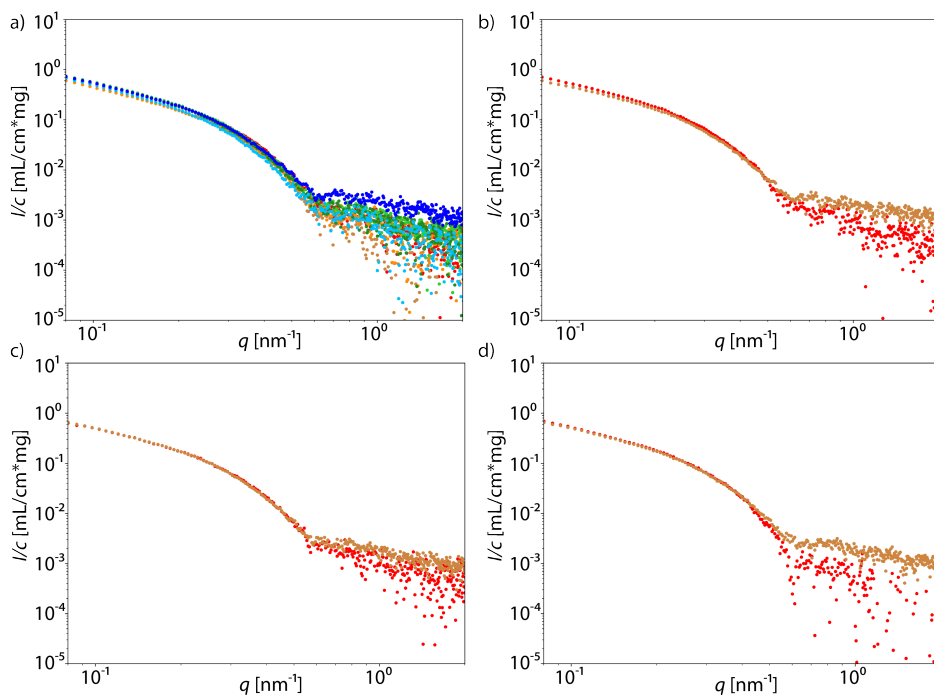
Figure A.19: *Individual SAXS curves of phophomimetic vimentin S38E. Different colors denote individual experiments; a) control measurements with wildtype vimentin; b) 1 % vimentin S38E; c) 5 % vimentin S38E; d) 10 % vimentin S38E.*
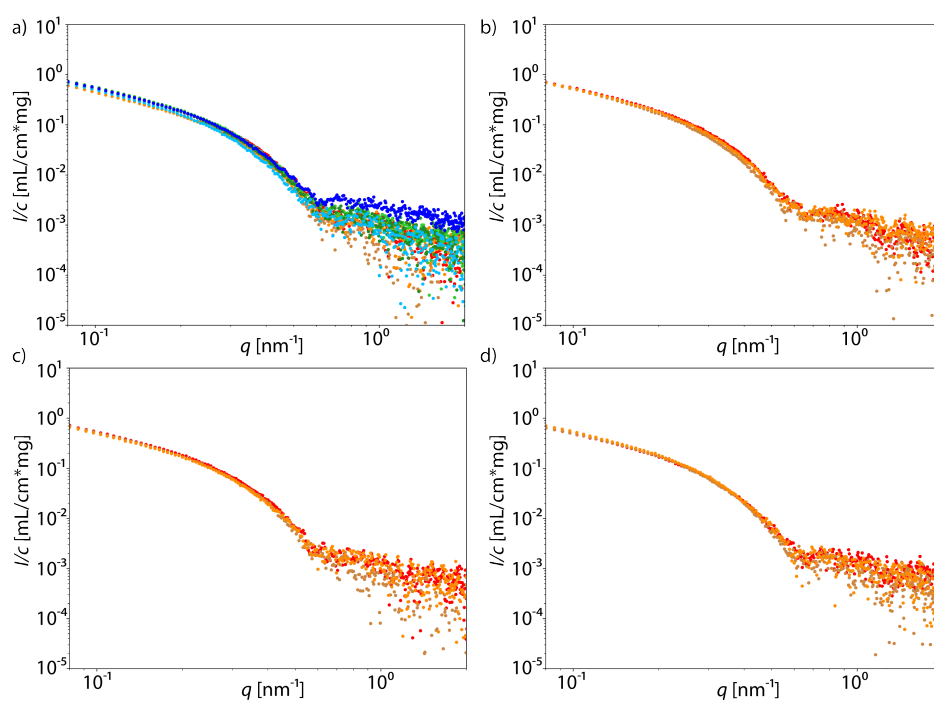
Figure A.20: *Individual SAXS curves of phophomimetic vimentin S72E. Different colors denote individual experiments; a)control measurements with wildtype vimentin; b)1 % vimentin S72E; c) 5 % vimentin S72E; d) 10 % vimentin S72E.*
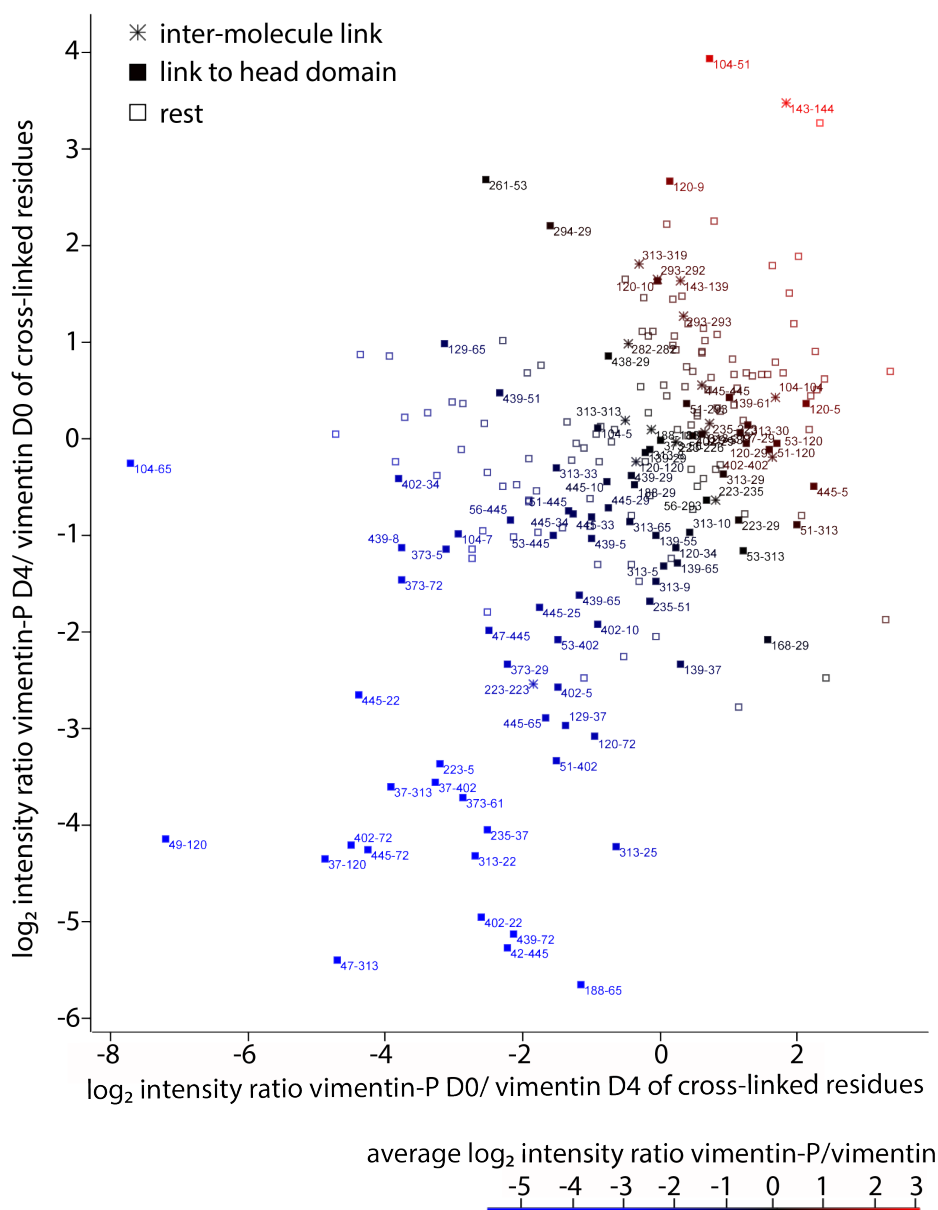
Figure A.21: *Quantified ratios (phosphorylated to non-phosphorylated) of cross-linked vimentin residues in two independent reaction replicates. Data point labels specify the cross-linked amino acid residues within vimentin. Cross-links including the N-terminal head domain (residue 1 to 94) are shown as filled squares and inter-molecular cross-links to the same amino acid residue are shown as asterisks. Data points are color-coded according to the average $\log_2$ intensity ratio ranging from a decreased (blue), unaltered (black), to increased (red) cross-link abundance upon phosphorylation. The majority of cross-linked residues does not change their abundance in response to phosphorylation. However, those cross-linked residues that change their abundance are mostly less abundant upon phosphorylation and are almost exclusively cross-links to the head domain. This indicates a conformational change of the head domain away from the rest of the vimentin protein.*
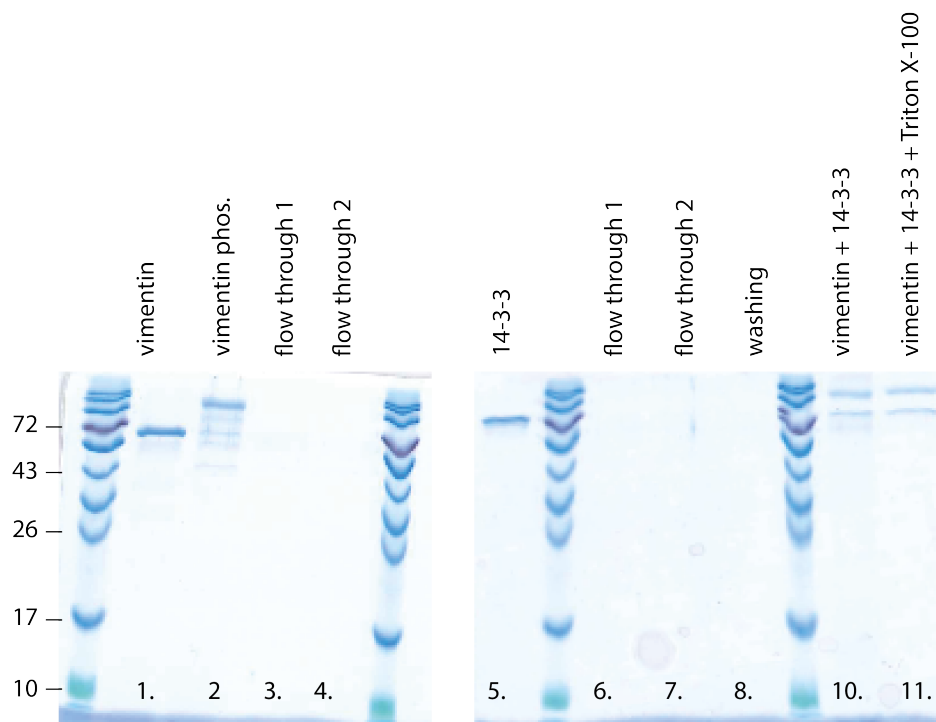
Figure A.22: *Pulldown assay shows interaction between vimentin and 14–3–3. This SDS gel shows the results of the streptavidin-biotin pull-down to investigate whether vimentin and 14–3–3 form a complex. The first lane shows vimentin and the second lane phosphorylated vimentin. Lane 3 and 4 show the flow through after incubation of the streptavidin agarose beads with vimentin. No vimentin is visible, indicating that the vimentin successfully bound to the beads. Lane 5 shows 14–3–3. Lane 6 and 7 show the flow through after the incubation of the beads bound to vimentin and 14–3–3. No band is observed, confirming the binding. Lane 8 shows a washing step in-between. Lane 10 and 11 show the protein bound to the beads with two bands at the weight of vimentin and 14–3–3. All unbound protein was washed off, vimentin bound to the beads via biotin-streptavidin binding and 14–3–3 formed a complex with the bound vimentin, therefore 2 bands are identified.*
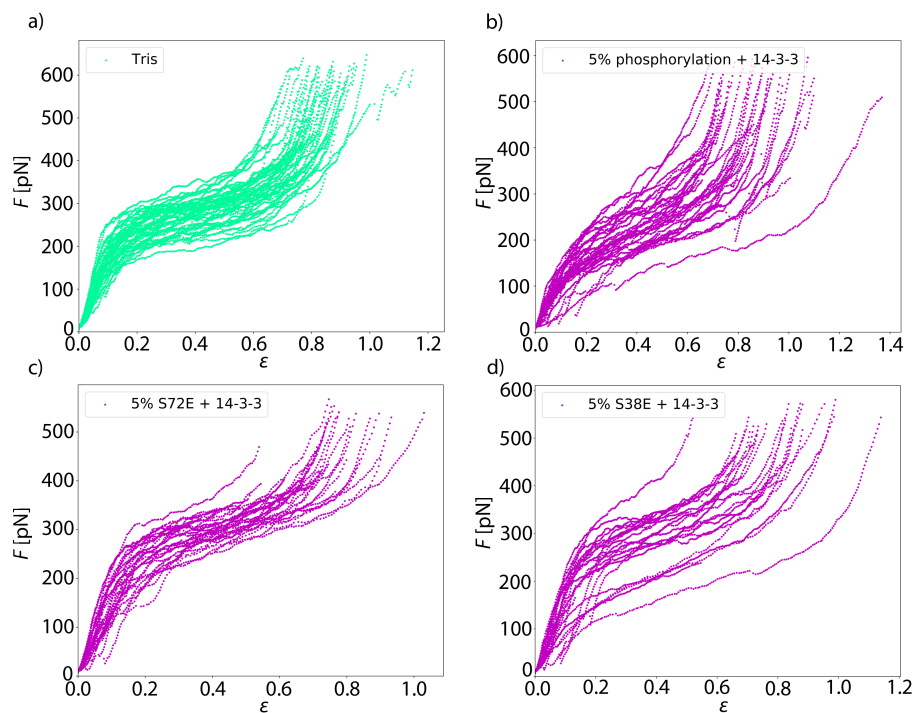
Figure A.23: *Single force-strain curves of all vimentin filaments incubated with 14–3–3. a) The control measurement without any modifications. b) Vimentin filaments with 5 % phosphorylated vimentin incubated with 14–3–3 shows softer filaments compared to the control. c) Vimentin filaments with 5 % of the S72E mutant incubated with 14–3–3 shows similar stiffness compared to the control. d) Vimentin filaments with 5 % of the mutant S38E also shows comparable stiffness to the control. The incubation of 14–3–3 with the mutations S72E and S38E does not change the force-strain behavior.*
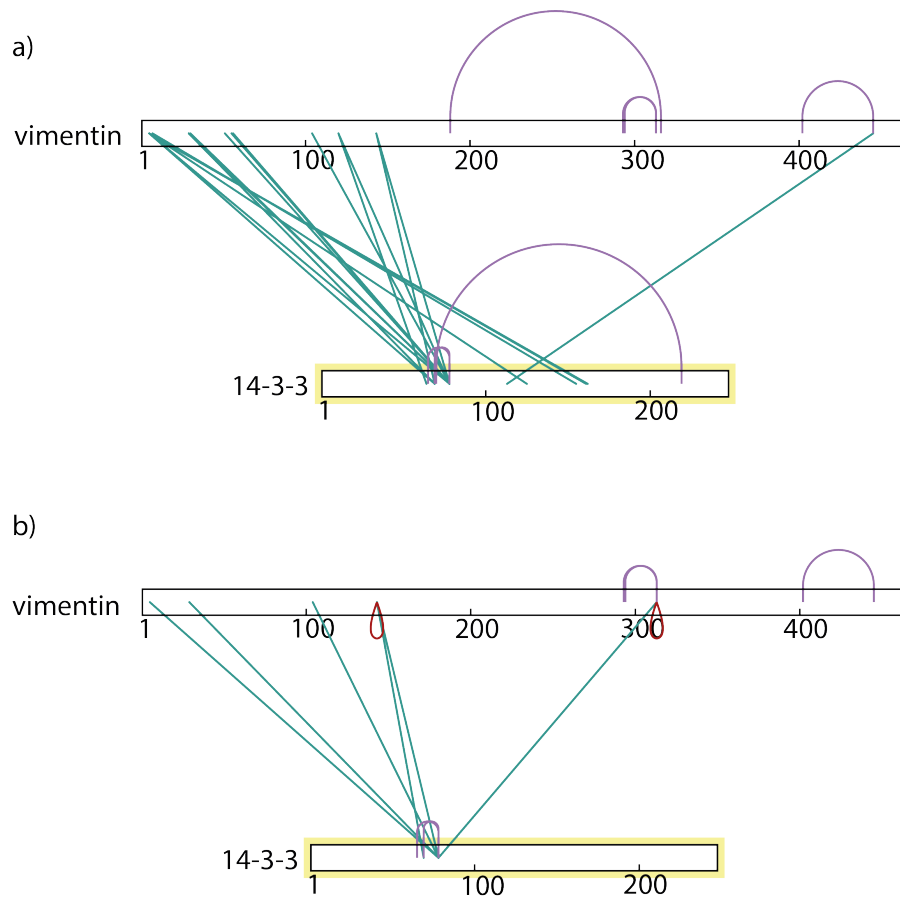
Figure A.24: *Mass spectrometry shows interaction sites of vimentin and 14–3–3. a) Vimentin monomer cross-linked with a 14–3–3 monomer. Green lines show cross-links between vimentin and 14–3–3, purple lines show cross-links within vimentin or 14–3–3 itself. The position that gets cross-linked most in the amino acid sequence of 14–3–3 is 78. It is linked to various positions in the amino acid sequence of vimentin, mostly found in the head region of vimentin. b) Vimentin dimer cross-linked with a 14–3–3 dimer. The color code of the lines is the same as above and red lines show cross-links within vimentin itself at the same position. The overall number of cross-links decreases, which is in accordance with limited sterical possibilities to form cross-links in a dimer compared to a monomer. The main cross-linking position in 14–3–3 is again 78 and two cross-linking positions (5, 29) for vimentin are located in the head domain of vimentin.*
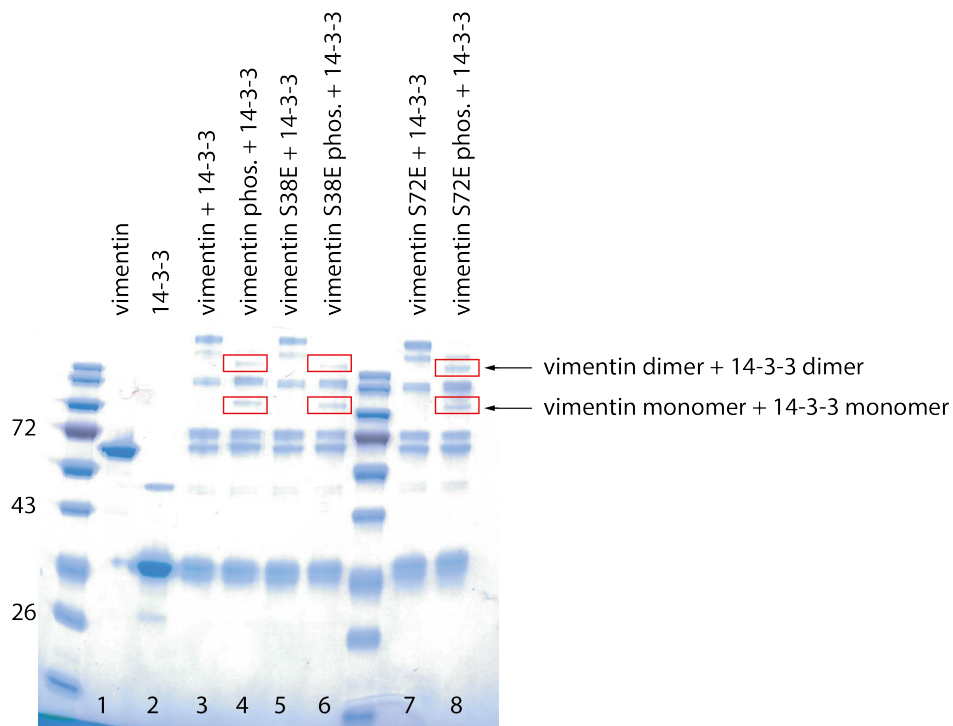
Figure A.25: *Investigation of the interaction between vimentin and 14–3–3 by cross-linking experiments. SDS gel of cross-linked probes. Cross-linking was performed with BS³. Lane 1 shows the vimentin control with no cross-linkers and lane 2 the control for 14–3–3 without cross-linkers. In lane 3, vimentin cross-linked with 14–3–3 and in lane 4 phosphorylated vimentin cross-linked with 14–3–3 are shown. In lane 5 vimentin S38E cross-linked with 14–3–3 and in lane 6 phosphorylated vimentin S38E cross-linked with 14–3–3 are shown. In lane 7 vimentin S72E cross-linked with 14–3–3 and in lane 8 phosphorylated vimentin S72E cross-linked with 14–3–3 are shown. We observe that the phosphorylated form of the different vimentin types cross-linked with 14–3–3 results in additional bands (indicated by red boxes and arrows), which show that there is a protein complex. The phosphomimetic mutants in their unphosphorylated form (lane 5 and 7) do not interact with 14–3–3. Only for the phosphorylated form of vimentin complexes with 14–3–3. Furthermore the phosphomimetic mutants complex with 14–3–3, showing that the sites S38 and S72 are not the binding sites of 14–3–3.*
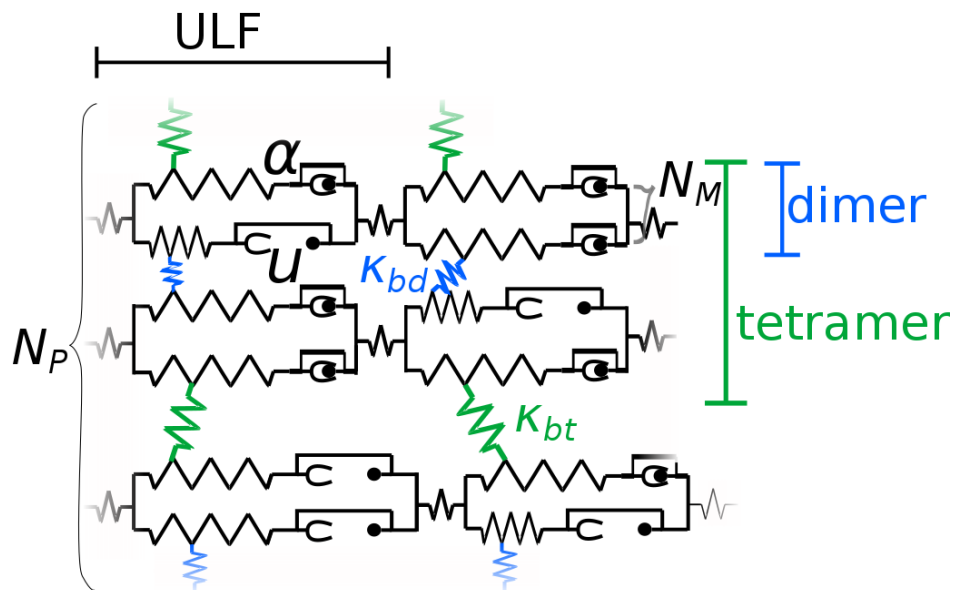
Figure A.26: *Sketch of the theoretical model for simulated force-strain curves. Each monomer is represented by a spring with a spring constant κ_α and by an element, which opens into an unfolded state u once force is applied. Two monomers are connected in parallel to form a dimer, thus the number of monomers in the dimer is $N_M = 2$. The dimers are connected by additional springs (blue) with a spring constant κ_{bd} to form tetramers. The connection between tetramers is established by another spring (green) with a spring constant κ_{bt}. Eight parallel tetramers ($N_P = 8$) form a ULF. The ULFs are connected in series via springs to a filament.*

Bibliography

1. Fletcher, D. A. & Mullins, R. D. Cell mechanics and the cytoskeleton. *Nature* **463,** 485–492 (2010).

2. Murray, M. E., Mendez, M. G. & Janmey, P. A. Substrate stiffness regulates solubility of cellular vimentin. *Molecular biology of the cell* **25,** 87–94 (2014).

3. Kidd, M. E., Shumaker, D. K. & Ridge, K. M. The Role of Vimentin Intermediate Filaments in the Progression of Lung Cancer. *Am. J. Resp. Cell Mol.* **50,** 1–6 (2014).

4. Gardel, M. L., Valentine, M. T. & Weitz, D. A. *Microrheology* 1–49 (Springer, 2005).

5. Szeverenyi, I., Cassidy, A. J., Chung, C. W., Lee, B. T. & Common, J. E. The human intermediate filament database: Comprehensive information on a gene family involved in many human diseases. *Hum, Mutat.* **29,** 351–360 (2008).

6. Herrmann, H., Strelkov, S. V., Burkhard, P., Aebi, U., *et al.* Intermediate filaments: primary determinants of cell architecture and plasticity. *J. Clin. Investig.* **119,** 1772–1783 (2009).

7. Pruss, R. M. *et al.* All classes of intermediate filaments share a common antigenic determinant defined by a monoclonal antibody. *Cell* **27,** 419–428 (1981).

8. Geisler, N. & Weber, K. Comparison of the proteins of two immunologically distinct intermediate-sized filaments by amino acid sequence analysis: desmin and vimentin. *Proc. Natl. Acad. Sci. U.S.A.* **78,** 4120–4123 (1981).

9. Herrmann, H. & Aebi, U. Intermediate Filaments: Strucutre and Assembly. *Cold Spring Harb Perspect. Biol.* **8,** a018242 (2016).

10. Crewther, W., Dowling, L., Steinert, P. & Parry, D. Structure of intermediate filaments. *International Journal of Biological Macromolecules* **5,** 267–274 (1983).

11. Steinert, P. M., Steven, A. C. & Roop, D. R. The molecular biology of intermediate filaments. *Cell* **42,** 411–419 (1985).

12. Herrmann, H. *et al.* Structure and Assembly Properties of the Intermediate Filament Protein Vimentin: The Role of its Head, Rod and Tail Domains. *J. Mol. Biol.* **264,** 933–953 (1996).

13. Chernyatina, A. A., Guzenko, D. & Strelkov, S. V. Intermediate filament structure: the bottom-up approach. *Curr. Opin. Cell Biol.* **32.** Cell architecture, 65–72 (2015).

14. Crick, F. The packing of *α*-helices: simple coiled-coils. *Acta Crystallogr.* **6,** 689–697 (1953).

15. Strelkov, S. V. *et al.* Conserved segments 1A and 2B of the intermediate filament dimer: their atomic structures and role in filament assembly. *EMBO J.* **21,** 1255–1266 (2002).

16. Herrmann, H. & Aebi, U. Intermediate Filaments: Molecular Structure, Assembly Mechanism, and Integration Into Functionally Distinct Intracellular Scaffolds. *Annu. Rev. Biochem.* **73,** 749–789 (2004).

17. Strelkov, S. V., Schumacher, J., Burkhard, P., Aebi, U. & Herrmann, H. Crystal structure of the human lamin A coil 2B dimer: implications for the head-to-tail association of nuclear lamins. *J. Mol. Biol.* **343,** 1067–1080 (2004).

18. Herrmann, H. & Aebi, U. Intermediate filaments and their associates: Multitalented structural elements specifying cytoarchitecture and cytodynamics. *Curr. Opin. Cell Biol.* **12,** 79–90 (2000).

19. Quinlan, R. A., Cohlberg, J. A., Schiller, D. L., Hatzfeld, M. & Franke, W. W. Heterotypic tetramer (A2D2) complexes of non-epidermal keratins isolated from cytoskeletons of rat hepatocytes and hepatoma cells. *J. Mol. Biol.* **178,** 365–388 (1984).

20. Steinert, P. The two-chain coiled-coil molecule of native epidermal keratin intermediate filaments is a type I-type II heterodimer. *J. Biol. Chem.* **265,** 8766–8774 (1990).

21. Fuchs, E. & Weber, K. Intermediate filaments: structure, dynamics, function and disease. *Annu. Rev. Biochem.* **63,** 345–382 (1994).

22. Conway, J. F. & Parry, D. A. Intermediate filament structure: 3. Analysis of sequence homologies. *J. Biol. Macromol.* **10,** 79–98 (1988).

23. Hatzfeld, M. & Franke, W. W. Pair formation and promiscuity of cytokeratins: formation in vitro of heterotypic complexes and intermediate-sized filaments by homologous and heterologous recombinations of purified polypeptides. *J. Cell Biol.* **101,** 1826–1841 (1985).

24. Herrmann, H., Häner, M., Brettel, M., Ku, N.-O. & Aebi, U. Characterization of distinct early assembly units of different intermediate filament proteins. *J. Mol. Biol.* **286,** 1403–1420 (1999).

25. Kirmse, R. *et al.* A quantitative kinetic model for the in vitro assembly of intermediate filaments from tetrameric vimentin. *J. Biol. Chem.* **282,** 18563–18572 (2007).

26. Portet, S. *et al.* Vimentin intermediate filament formation: in vitro measurement and mathematical modeling of the filament length distribution during assembly. *Langmuir* **25,** 8817–8823 (2009).

27. Tzivion, G., Luo, Z. J. & Avruch, J. Calyculin A-induced vimentin phosphorylation sequesters 14-3-3 and displaces other 14-3-3 partners in vivo. *J. Biol. Chem.* **275,** 29772–29778 (2000).

28. Gardino, A. K. & Yaffe, M. B. 14-3-3 proteins as signaling integration points for cell cycle control and apoptosis. *Semin. Cell Dev. Biol.* **22,** 688–695 (2011).

29. Ku, N.-O., Michie, S., Resurreccion, E. Z., Broome, R. L. & Omary, M. B. Keratin binding to 14-3-3 proteins modulates keratin filaments and hepatocyte mitotic progression. *Proc. Natl. Acad. Sci. U.S.A.* **99,** 4373–4378 (2002).

30. Miao, L., Teng, J., Lin, J., Liao, X. & Chen, J. 14-3-3 proteins interact with neurofilament protein-L and regulate dynamic assembly of neurofilaments. *J. Cell Sci.* **126,** 427–436 (2013).

31. Eriksson, J. E. *et al.* Specific in vivo phosphorylation sites determine the assembly dynamics of vimentin intermediate filaments. *J. Cell Sci.* **117,** 919–932 (2004).

32. Busch, T. *et al.* Keratin 8 phosphorylation regulates keratin reorganization and migration of epithelial tumor cells. *J. Cell Sci.* **125,** 2148–2159 (2012).

33. Shea, T. B. & Chan, W. K.-H. Regulation of neurofilament dynamics by phosphorylation. *Eur. J. Neurosci.* **27,** 1893–1901 (2008).

34. Holmgren, A., Bouhy, D. & Timmerman, V. Neurofilament phosphorylation and their proline-directed kinases in health and disease. *J. Peripher. Nerv.* **17,** 365–376 (2012).

35. Snider, N. T. & Omary, M. B. Post-translational modifications of intermediate filament proteins: mechanisms and functions. *Nat. Rev. Mol. Cell Biol.* **15,** 163–177 (2014).

36. Shorter, S. An Investigation of the Nature of the Elasticity of Fibers. *J. Text. I.* **15,** T207–T229 (1924).

37. Speakman, J. B. The intracellular structure of the wool fibre. *J. Text. I.* **18,** T431–T453 (1927).

38. Astbury, W. T. & Street, A. X-ray studies of the structure of hair, wool, and related fibres.-i. general. *Philos. Trans. R. Soc. Lond., Series A, Containing Papers of a Mathematical or Physical Character* **230,** 75–101 (1931).

39. Astbury, W. T. & Woods, H. J. X-Ray studies of the structure of hair, wool, and related fibres. II.-the molecular structure and elastic properties of hair keratin. *P Philos. trans. R. Soc. Lond., Series A, Containing Papers of a Mathematical or Physical Character* **232,** 333–394 (1933).

40. Astbury, W. T. & Sisson, W. A. X-ray studies of the structure of hair, wool, and related fibres-III—The configuration of the keratin molecule and its orientation in the biological cell. *Philos. trans. R. Soc. Lond., Series A-Mathematical and Physical Sciences* **150,** 533–551 (1935).

41. Bendit, E. A quantitative x-ray diffraction study of the alpha-beta transformation in wool keratin. *Text. Res. J.* **30,** 547–555 (1960).

42. Hearle, J. A critical review of the structural mechanics of wool and hair fibres. *J. Biol. Macromol.* **27,** 123–138 (2000).

43. Kreplak, L. & Fudge, D. Biomechanical properties of intermediate filaments: from tissues to single filaments and back. *Bioessays* **29,** 26–35 (2007).

44. Kreplak, L., Bär, H., Leterrier, J. F., Herrmann, H. & Aebi, U. Exploring the mechanical behavior of single intermediate filaments. *J. Mol. Biol.* **354,** 569–577 (2005).

45. Kreplak, L., Herrmann, H. & Aebi, U. Tensile properties of single desmin intermediate filaments. *Biophys. J.* **94,** 2790–2799 (2008).

46. Ackbarow, T. & Buehler, M. J. Superelasticity, energy dissipation and strain hardening of vimentin coiled-coil intermediate filaments: atomistic and continuum studies. *J. Mater. Sci.* **42,** 8771–8787 (2007).

47. Qin, Z., Kreplak, L. & Buehler, M. Hierarchical structure controls nanomechanical properties of vimentin intermediate filaments. *PLoS ONE* **4,** 1–14 (2009).

48. Pinto, N. *et al.* Self-Assembly Enhances the Strength of Fibers Made from Vimentin Intermediate Filament Proteins. *Biomacromolecules* **15,** 574–581 (2014).

49. Block, J. *et al.* Nonlinear Loading-Rate-Dependent Force Response of Individual Vimentin Intermediate Filaments to Applied Strain. *Phys. Rev. Lett.* **118,** 1–5 (2017).

50. Block, J. *et al.* Viscoelastic properties of vimentin originate from nonequilibrium conformational changes. *Sci. Adv.* **4,** eaat1161 (2018).

51. Lorenz, C. *et al.* Lateral Subunit Coupling Determines Intermediate Filament Mechanics. *Phys. Rev. Lett.* **123,** 188102 (2019).

52. Schepers, A. V., Lorenz, C. & Köster, S. Tuning intermediate filament mechanics by variation of pH and ion charges. *Nanoscale* **12,** 15236–15245 (2020).

53. Denz, M., Marschall, M., Herrmann, H. & Köster, S. Ion type and valency differentially drive vimentin tetramers into intermediate filaments or higher order assemblies. *Soft Matter* (2020).

54. Qin, Z., Kreplak, L. & Buehler, M. J. Nanomechanical properties of vimentin intermediate filament dimers. *Nanotechnology* **20,** 425101 (2009).

55. Forsting, J., Kraxner, J., Witt, H., Janshoff, A. & Köster, S. Vimentin Intermediate Filaments Undergo Irreversible Conformational Changes during Cyclic Loading. *Nano Lett.* **19,** 7349–7356 (2019).

56. Strobl, G. R. *The Physics of Polymers: Concepts for Understanding Their Structures and Behavior* (Springer Science & Business Media, 2007).

57. Kratky, O. & Porod, G. Röntgenuntersuchung gelöster fadenmoleküle. *Rec. Trav. Chim. Pays Bas* **68,** 1106–1122 (1949).

58. Yamakawa, H. in *Macromolecular Chemistry–11* 135–141 (Elsevier, 1977).

59. Andrews, S. S. Methods for modeling cytoskeletal and DNA filaments. *Phys. Biol.* **11,** 011001 (2014).

60. Van der Maarel, J. R. *Introduction to biopolymer physics* (World Scientific Publishing Company, 2007).

61. Kumar, S. & Li, M. S. Biomolecules under mechanical force. *Phys. Rep.* **486,** 1–74 (2010).

62. Bustamante, C., Marko, J., Siggia, E. & Smith, S. Entropic elasticity of lambda-phage DNA. *Science* **265,** 1599–1600 (1994).

63. Burte, H. & Halsey, G. A new theory of non-linear viscous elasticity. *Text. Res. J.* **17,** 465–476 (1947).

64. Rief, M., Fernandez, J. M. & Gaub, H. E. Elastically coupled two-level systems as a model for biopolymer extensibility. *Phys.Rev. Lett.* **81,** 4764 (1998).

65. Evans, E. & Ritchie, K. Dynamic strength of molecular adhesion bonds. *Biophys. J.* **72,** 1541–1555 (1997).

66. Bell, G. I. Models for the specific adhesion of cells to cells. *Science* **200,** 618–627 (1978).

67. Lakowicz, J. R. *Principles of fluorescence spectroscopy* (Springer science & business media, 2013).

68. Jabłoński, A. Über den mechanismus der Photolumineszenz von Farbstoffphosphoren. *Zeitschrift für Physik* **94,** 38–46 (1935).

69. Stokes, G. G. XXX. On the change of refrangibility of light. *Philos. Trans. R. Soc. Lon.* 463–562 (1852).

70. Ashkin, A. Acceleration and trapping of particles by radiation pressure. *Phys. Rev. Lett.* **24,** 156 (1970).

71. Killian, J. L., Ye, F. & Wang, M. D. Optical tweezers: A force to be reckoned with. *Cell* **175,** 1445–1448 (2018).

72. Ashkin, A. & Dziedzic, J. M. Optical trapping and manipulation of viruses and bacteria. *Science* **235,** 1517–1520 (1987).

73. Ashkin, A., Dziedzic, J. M. & Yamane, T. Optical trapping and manipulation of single cells using infrared laser beams. *Nature* **330,** 769–771 (1987).

74. Block, S. M., Blair, D. F. & Berg, H. C. Compliance of bacterial flagella measured with optical tweezers. *Nature* **338,** 514–518 (1989).

75. Ashkin, A., Schütze, K., Dziedzic, J., Euteneuer, U. & Schliwa, M. Force generation of organelle transport measured in vivo by an infrared laser trap. *Nature* **348,** 346–348 (1990).

76. Svoboda, K., Schmidt, C. F., Schnapp, B. J. & Block, S. M. Direct observation of kinesin stepping by optical trapping interferometry. *Nature* **365,** 721–727 (1993).

77. Smith, S. B., Cui, Y. & Bustamante, C. Overstretching B-DNA: the elastic response of individual double-stranded and single-stranded DNA molecules. *Science* **271,** 795–799 (1996).

78. Wang, M. D. *et al.* Force and velocity measured for single molecules of RNA polymerase. *Science* **282,** 902–907 (1998).

79. Forth, S., Hsia, K.-C., Shimamoto, Y. & Kapoor, T. M. Asymmetric friction of nonmotor MAPs can lead to their directional motion in active microtubule networks. *Cell* **157,** 420–432 (2014).

80. Lansky, Z. *et al.* Diffusible crosslinkers generate directed forces in microtubule networks. *Cell* **160,** 1159–1168 (2015).

81. Vivek, A., Bolognesi, G. & Elani, Y. Fusing artificial cell compartments and lipid domains using optical traps: A tool to modulate membrane composition and phase behaviour. *Micromachines* **11,** 388 (2020).

82. Koch, M. D. & Shaevitz, J. W. in *Optical Tweezers* 3–24 (Springer, 2017).

83. Svoboda, K. & Block, S. M. Biological applications of optical forces. *Annu. Rev. Bioph. Biom.* **23,** 247–285 (1994).

84. Gennerich, A. *Optical Tweezers* (Springer, 2017).

85. Rohrbach, A. Stiffness of optical traps: quantitative agreement between experiment and electromagnetic theory. *Phys. Rev. Lett.* **95,** 168102 (2005).

86. Waigh, T. A. Microrheology of complex fluids. *Rep. Prog. Phys.* **68,** 685 (2005).

87. Ziemann, F., Rädler, J. & Sackmann, E. Local measurements of viscoelastic moduli of entangled actin networks using an oscillating magnetic bead microrheometer. *Biophys. J.* **66,** 2210–2216 (1994).

88. Amblard, F., Maggs, A. C., Yurke, B., Pargellis, A. N. & Leibler, S. Subdiffusion and anomalous local viscoelasticity in actin networks. *Phys. Rev. Lett.* **77,** 4470 (1996).

89. Guo, M. *et al.* The role of vimentin intermediate filaments in cortical and cytoplasmic mechanics. *Biophys. J.* **105,** 1562–1568 (2013).

90. Rotsch, C. & Radmacher, M. Drug-induced changes of cytoskeletal structure and mechanics in fibroblasts: an atomic force microscopy study. *Biophys. J.* **78,** 520–535 (2000).

91. Mason, T. G. & Weitz, D. A. Optical measurements of frequency-dependent linear viscoelastic moduli of complex fluids. *Phys. Rev. Lett.* **74,** 1250 (1995).

92. Berg, H. C. *Random walks in biology* (Princeton University Press, 1993).

93. Reif, F. Fundamentals of thermal and statistical physics. *McGraw-Hill* **5, 7** (1965).

94. Levine, A. J. & Lubensky, T. One-and two-particle microrheology. *Phys. Rev. Lett.* **85,** 1774 (2000).

95. Crocker, J. C. & Grier, D. G. Methods of digital video microscopy for colloidal studies. *J. Colloid Interface Sci.* **179,** 298–310 (1996).

96. Janmey, P. A., Euteneuer, U., Traub, P. & Schliwa, M. Viscoelastic properties of vimentin compared with other filamentous biopolymer networks. *J. Cell Biol.* **113,** 155–160 (1991).

97. Schopferer, M. *et al.* Desmin and vimentin intermediate filament networks: their viscoelastic properties investigated by mechanical rheometry. *J. Mol. Biol.* **388,** 133–143 (2009).

98. Lin, Y.-C. *et al.* Divalent cations crosslink vimentin intermediate filament tail domains to regulate network mechanics. *J. Mol. Biol.* **399,** 637–644 (2010).

99. Lin, Y.-C. *et al.* Origins of elasticity in intermediate filament networks. *Phys. Rev. Lett.* **104,** 058101 (2010).

100. Pawelzyk, P., Herrmann, H. & Willenbacher, N. Mechanics of intermediate filament networks assembled from keratins K8 and K18. *Soft Matter* **9,** 8871–8880 (2013).

101. Köster, S., Lin, Y.-C., Herrmann, H. & Weitz, D. A. Nanomechanics of vimentin intermediate filament networks. *Soft Matter* **6,** 1910–1914 (2010).

102. Wu, H. *et al.* Effect of Divalent Cations on the Structure and Mechanics of Vimentin Intermediate Filaments. *Biophys. J.* **119,** 55–64 (July 2020).

103. Schepers, A. V. *et al.* Multiscale mechanics and temporal evolution of vimentin intermediate filament networks. *bioRxiv* (2021).

104. Kraxner, J. *et al.* Post-translational modifications soften vimentin intermediate filaments. *Nanoscale* **13,** 380–387 (2021).

105. Winheim, S. *et al.* Deconstructing the Late Phase of Vimentin Assembly by Total Internal Reflection Fluorescence Microscopy (TIRFM). *PLoS ONE* **6,** e19202 (Apr. 2011).

106. Brennich, M. E. *et al.* Impact of ion valency on the assembly of vimentin studied by quantitative small angle X-ray scattering. *Soft Matter* **10,** 2059–2068 (2014).

107. Mücke, N. *et al.* Molecular and biophysical characterization of assembly-starter units of human vimentin. *J. Mol. Biol.* **340,** 97–114 (2004).

108. Janissen, R. *et al.* Invincible DNA tethers: Covalent DNA anchoring for enhanced temporal and force stability in magnetic tweezers experiments. *Nucleic Acids Res.* **42,** e137 (2014).

109. Kilisch, M., Lytovchenko, O., Arakel, E. C., Bertinetti, D. & Schwappach, B. A dual phosphorylation switch controls 14-3-3-dependent cell surface expression of TASK-1. *J. Cell Sci.* **129,** 831–842 (2016).

110. Alberts, B. *Molecular biology of the cell* Sixth edition. ISBN: 0815345240 (Garland Science Taylor and Francis Group, New York NY, 2015).

111. Huber, F., Boire, A., López, M. P. & Koenderink, G. H. Cytoskeletal crosstalk: when three different personalities team up. *Curr. Opin. Cell Biol.* **32,** 39–47 (2015).

112. Latorre, E. *et al.* Active superelasticity in three-dimensional epithelia of controlled shape. *Nature* **563,** 203–208 (2018).

113. Fudge, D. *et al.* The intermediate filament network in cultured human keratinocytes is remarkably extensible and resilient. *PLoS ONE* **3,** e2327 (2008).

114. Mendez, M. G., Restle, D. & Janmey, P. A. Vimentin enhances cell elastic behavior and protects against compressive stress. *Biophys. J.* **107,** 314–323 (2014).

115. Freikamp, A., Mehlich, A., Klingner, C. & Grashoff, C. Investigating piconewton forces in cells by FRET-based molecular force microscopy. *J. Struct. Biol.* **197,** 37–42 (2017).

116. Style, R. W. *et al.* Traction force microscopy in physics and biology. *Soft Matter* **10,** 4047 (2014).

117. Mücke, N. *et al.* Molecular and biophysical characterization of assembly-starter units of human vimentin. *J. Mol. Biol.* **340,** 97–114 (2004).

118. Nöding, B., Herrmann, H. & Köster, S. Direct observation of subunit exchange along mature vimentin intermediate filaments. *Biophys. J.* **107,** 2923–2931 (2014).

119. Block, J., Schroeder, V., Pawelzyk, P., Willenbacher, N. & Köster, S. Physical properties of cytoplasmic intermediate filaments. *Biochim. Biophys. Acta* **1853,** 3053–3064 (2015).

120. Steinert, P. M., Marekov, L. N. & Parry, D. A. Diversity of intermediate filament structure. Evidence that the alignment of coiled-coil molecules in vimentin is different from that in keratin intermediate filaments. *J. Biol. Chem.* **268,** 24916–24925 (1993).

121. Downing, D. T. Chemical cross–linking between lysine groups in vimentin oligomers is dependent on local peptide conformations. *Proteins* **25,** 215–224 (1996).

122. Qin, Z. & Buehler, M. J. Molecular Dynamics Simulation of the \beta-Sheet Transition in Coiled Protein Filaments: Evidence for a Critical Filament Length Scale. *Phys. Rev. Lett.* **104,** 198304 (2010).

123. Seifert, U. Rupture of multiple parallel molecular bonds under dynamic loading. *Phys. Rev. Lett.* **84,** 2750–2753 (2000).

124. Erdmann, T. & Schwarz, U. S. Stability of adhesion clusters under constant force. *Phys. Rev. Lett.* **92,** 108102 (2004).

125. Erdmann, T. *Stochastic dynamics of adhesion clusters under force* PhD thesis (2005).

126. Friddle, R. W., Noy, A. & de Yoreo, J. J. Interpreting the widespread nonlinear force spectra of intermolecular bonds. *Proc. Natl. Acad. Sci. U.S.A.* **109,** 13573–13578 (2012).

127. Minin, K. A., Zhmurov, A., Marx, K. A., Purohit, P. K. & Barsegov, V. Dynamic Transition from alpha-Helices to beta-Sheets in Polypeptide Coiled-Coil Motifs. *J. Am. Chem. Soc.* **139,** 16168–16177 (2017).

128. Kumar, P. K. & Lagoudas, D. C. *Shape Memory Alloys. Modeling and engineering applications - Chapter 1: Introduction to Shape Memory Alloys* ISBN: 978-0-387-47685-8 (Springer US, Boston, MA, 2008).

129. Ngai, J., Coleman, T. R. & Lazarides, E. Localization of newly synthesized vimentin subunits reveals a novel mechanism of intermediate filament assembly. *Cell* **60,** 415–427 (1990).

130. Çolakoğlu, G. & Brown, A. Intermediate filaments exchange subunits along their length and elongate by end-to-end annealing. *J. Cell Biol.* **185,** 769–777 (2009).

131. Nöding, B., Herrmann, H. & Köster, S. Direct Observation of Subunit Exchange along Mature Vimentin Intermediate Filaments. *Biophys. J.* **107,** 2923–2931 (2014).

132. Windoffer, R., Beil, M., Magin, T. M. & Leube, R. E. Cytoskeleton in motion: The dynamics of keratin intermediate filaments in epithelia. *J. Cell Biol.* **194,** 669–678 (2011).

133. Kölsch, A., Windoffer, R., Würflinger, T., Aach, T. & Leube, R. E. The keratin-filament cycle of assembly and disassembly. *J. Cell Sci.* **123,** 2266–2272 (2010).

134. Lee, C.-H., Kim, M.-S., Chung, B. M., Leahy, D. J. & Coulombe, P. A. Structural basis for heteromeric assembly and perinuclear organization of keratin filaments. *Nat. Struct. Mol. Biol.* **19,** 707–715 (2012).

135. Sun, T. T. & Green, H. Keratin filaments of cultured human epidermal cells. Formation of intermolecular disulfide bonds during terminal differentiation. *J. Biol. Chem.* **253,** 2053–2060 (1978).

136. Clément, S. *et al.* The intermediate filament protein, vimentin, in the lens is a target for cross-linking by transglutaminase. *J. Biol. Chem.* **273,** 7604–7609 (1998).

137. Gupta, M., Greenberg, C. S., Eckman, D. M. & Sane, D. C. Arterial vimentin is a transglutaminase substrate: A link between vasomotor activity and remodeling? *J. Vasc. Res.* **44,** 339–344 (2007).

138. Efron, B. & Tibshirani, R. J. *An introduction to the bootstrap* ISBN: 0412042312 (Chapman & Hall, New York and London, 1993).

139. Ackbarow, T. & Buehler, M. J. Molecular mechanics of stutter defects in vimentin intermediate filaments. *Exp. Mech.* **49,** 79–89 (2009).

140. Qin, Z. & Buehler, M. J. Structure and dynamics of human vimentin intermediate filament dimer and tetramer in explicit and implicit solvent models. *J. Mol. Model.* **17,** 37–48 (2011).

141. Eriksson, J. E. *et al.* Introducing intermediate filaments: from discovery to disease. *J. Clin. Invest.* **119,** 1763–1771 (2009).

142. Fuchs, E. & Cleveland, D. W. A Structural Scaffolding of Intermediate Filaments in Health and Disease. *Science* **279,** 514–519 (1998).

143. Hyder, C. L., Pallari, H.-M., Kochin, V. & Eriksson, J. E. Providing cellular signposts - Post-translational modifications of intermediate filaments. *FEBS Lett.* **582,** 2140–2148 (2008).

144. Traub, P. & Vorgias, C. E. Involvement of the N-terminal polypeptide of vimentin in the formation of intermediate filaments. *J. Cell Sci.* **63,** 43–67 (1983).

145. Evans, R. M. Cyclic AMP-dependent protein kinase-induced vimentin filament disassembly involves modification of the N-terminal domain of intermediate filament subunits. *FEBS Lett.* **234,** 73–78 (1988).

146. Parry, D. A. & Steinert, P. M. *Intermediate filament structure* 183 pp. (Springer-Verlag, 1995).

147. Smith, A. J., Daut, J. & Schwappach, B. Membrane proteins as 14-3-3 clients in functional regulation and intracellular transport. *Physiology* **26,** 181–191 (2011).

148. Barberis, L. *et al.* Leukocyte transmigration is modulated by chemokine-mediated PI3Kγ-dependent phosphorylation of vimentin. *Eur. J. Immunol.* **39,** 1136–1146 (2009).

149. Lim, Y.-P., Wong, C. Y., Ooi, L. L., Druker, B. J. & Epstein, R. J. Selective Tyrosine Hyperphosphorylation of Cytoskeletal and Stress Proteins in Primary Human Breast Cancers. *Clin. Cancer Res.* **10,** 3980–3987 (2004).

150. Zhu, Q. *et al.* Vimentin is a novel AKT1 target mediating motility and invasion. *Oncogene* **30,** 457–470 (2011).

151. Ivaska, J., Pallari, H.-M., Nevo, J. & Eriksson, J. E. Novel functions of vimentin in cell adhesion, migration, and signaling. *Exp. Cell Res.* **313.** Special Issue - Intermediate Filaments, 2050–2062 (2007).

152. Wang, R. C. *et al.* Akt-Mediated Regulation of Autophagy and Tumorigenesis Through Beclin 1 Phosphorylation. *Science* **338,** 956–959 (2012).

153. Chernyatina, A. A., Nicolet, S., Aebi, U., Herrmann, H. & Strelkov, S. V. Atomic structure of the vimentin central alpha-helical domain and its implications for intermediate filament assembly. *Proc. Natl. Acad. Sci. U.S.A.* **109,** 13620–13625 (2012).

154. Premchandar, A. *et al.* Structural Dynamics of the Vimentin Coiled-coil Contact Regions Involved in Filament Assembly as Revealed by Hydrogen-Deuterium Exchange. *J. Biol. Chem.* **291,** 24931–24950 (2016).

155. Schmidt, C. & Urlaub, H. iTRAQ-Labeling of In-Gel Digested Proteins for Relative Quantification. *Methods Mol. Biol.* **564,** 207–226 (2009).

156. Wessel, D. & Flügge, U. A method for the quantitative recovery of protein in dilute solution in the presence of detergents and lipids. *Anal. Biochem.* **138,** 141–143 (1984).

157. Chen, Z. L. *et al.* A high-speed search engine pLink 2 with systematic evaluation for proteome-scale identification of cross-linked peptides. *Nat. Commun.* **10** (1 2019).

158. Yang, B. *et al.* Identification of cross-linked peptides from complex samples. *Nat. Methods* **9,** 904–906 (Sept. 2012).

159. Fischer, L., Chen, Z. A. & Rappsilber, J. Quantitative cross-linking/mass spectrometry using isotope-labelled cross-linkers. *J. Proteomics* **88,** 120–128 (2013).

160. Chen, Z. A., Fischer, L., Cox, J. & Rappsilber, J. Quantitative cross-linking/mass spectrometry using isotope-labeled cross-linkers and MaxQuant. *Mol. Cell. Proteomics* **15,** 2769–2778 (2016).

161. Combe, C. W., Fischer, L. & Rappsilber, J. xiNET: cross-link network maps with residue resolution. *Mol. Cell. Proteomics* **14,** 1137–1147 (2015).

162. Tyanova, S. *et al.* The Perseus computational platform for comprehensive analysis of (prote) omics data. *Nat. Methods* **13,** 731 (2016).

163. Cox, J. & Mann, M. MaxQuant enables high peptide identification rates, individualized ppb-range mass accuracies and proteome-wide protein quantification. *Nat. Biotechnol.* **26,** 1367–1372 (2008).

164. Tyanova, S., Temu, T. & Cox, J. The MaxQuant computational platform for mass spectrometry-based shotgun proteomics. *Nat. Protoc.* **11,** 2301 (2016).

165. Consortium, U. UniProt: a worldwide hub of protein knowledge. *Nucleic Acids Res.* **47,** D506–D515 (2019).

166. MacLean, B. *et al.* Skyline: an open source document editor for creating and analyzing targeted proteomics experiments. *Bioinformatics* **26,** 966–968 (2010).

167. Konarev, P. V., Volkov, V. V., Sokolova, A. V., Koch, M. H. J. & Svergun, D. I. PRIMUS: a Windows PC-based system for small-angle scattering data analysis. *J. Appl. Crystallogr.* **36,** 1277–1282 (2003).

168. Eigel, M., Gruhlke, R., Marschall, M., Trunschke, P. & Zander, E. `alea` - *A Python Framework for Spectral Methods and Low-Rank Approximations in Uncertainty Quantification* `https://bitbucket.org/aleadev/alea`.

169. Svergun, D. I. & Koch, M. H. J. Small-angle scattering studies of biological macromolecules in solution. *Rep. Prog. Phys.* **66,** 1735–1782 (2003).

170. Mertens, H. D. & Svergun, D. I. Structural characterization of proteins and complexes using small-angle X-ray solution scattering. *J. Struct. Biol.* **172,** 128–141 (2010).

171. Parry, D. A., Strelkov, S. V., Burkhard, P., Aebi, U. & Herrmann, H. Towards a molecular description of intermediate filament structure and assembly. *Exp. Cell Res.* **313,** 2204–2216 (2007).

172. Goldie, K. N. *et al.* Dissecting the 3-D structure of vimentin intermediate filaments by cryo-electron tomography. *J. Struct. Biol.* **158,** 378–385 (2007).

173. Strelkov, S. V., Schumacher, J., Burkhard, P., Aebi, U. & Herrmann, H. Crystal Structure of the Human Lamin A Coil 2B Dimer: Implications for the Head-to-tail Association of Nuclear Lamins. *J. Mol. Biol.* **343,** 1067–1080 (2004).

174. Kornreich, M., Avinery, R., Malka-Gibor, E., Laser-Azogui, A. & Beck, R. Order and disorder in intermediate filament proteins. *FEBS Lett.* **589,** 2464–2476 (2015).

Acknowledgements

Finally, it is time to thank a lot of people who helped me on my way.

First of all, I would like to thank my supervisor **Prof. Sarah Köster** a lot. Thank you for the opportunity to work on such a great topic in an amazing team. I also thank you for your always honest, positive and constructive feedback during meetings or practice talks, for the opportunity to present my work at national and international conferences and for pushing and encouraging me to perform at my best.

Thanks to **Prof. Andreas Janhoff** for being part of my thesis committee and the second reviewer of my thesis. For all the interesting suggestions and helpful discussions during the meetings. To **Hannes Witt** for his help with the first paper.

Thanks also to **Prof. Blanche Schwappach** for all the advises and helpful discussions when being part of my thesis committee, for suggesting additional and interesting projects and for being part of the examination board. Thanks also to **Julia Menzel** for all your help with the phosphorylation and the protein 14–3–3.

I am grateful to **Prof. Timo Betz**, **Prof. Henning Urlaub** and **Ralf Ficner** for being part of my examination board. Thanks also to **Ivan Parfentev** and **Iwan Silbern** for performing the mass spectrometry experiments and for your help with the paper.

Many thanks to **Prof. Harald Herrmann** and **Dr. Norbert Mücke** for all those helpful discussions and ideas during the IF meetings and for your endless knowledge about IFs. Moreover, for being the one introducing me to this amazing group.

In generall, I want to thank all the people from the **IRP** for all the valuable discussion during seminars or thursday cake breaks. Thanks to the IRP secretaries, **Christine Wilke-Feist**, **Kerstin Pluschke** and **Michaela Ständer** for all your help with any kind of administrative formalities. Moreover, to **Jan Goeman** for a lot of IT assistance and to **Peter Luley** for the help with solving any technical problem. Thanks to **Dr. Ulrike Rölleke**, **Susanne Hengst** and **Kamila Sabagh** for all your help in the lab and your tireless support to get the phostag-gels to work. A big thanks to **Susanne Bauch** for your enthusiastic commitment in preparing so many vimentin batches at

List of Publications

- Julia Kraxner, Charlotta Lorenz, Julia Menzel, Ivan Parfentev, Iwan Silbern, Manuela Denz, Henning Urlaub, Blanche Schwappach and Sarah Köster, "Post-translational modifications soften vimentin intermediate filaments", In: *Nanoscale* 13.1 (2021), pp. 380-387. DOI: 10.1039/D0NR07322A.

- Charlotta Lorenz, Johanna Forsting, Anna V. Schepers, Julia Kraxner, Susanne Bauch, Hannes Witt, Stefan Klumpp, and Sarah Köster, "Lateral Subunit Coupling Determines Intermediate Filament Mechanics", In: *Phys. Rev. Lett.* 123.18 (2019), pp. 188102. DOI: 10.1103/PhysRevLett.123.188102.

- Johanna Forsting, Julia Kraxner, Hannes Witt, Andreas Janshoff and Sarah Köster, "Vimentin Intermediate Filaments Undergo Irreversible Conformational Changes during Cyclic Loading", In: *Nano Lett.* 19.10 (2019), pp. 7349-7356. DOI: 10.1021/acs.nanolett.9b02972.

- Thorsten Kolb, Julia Kraxner, Kai Skodzek, Michael Haug, Dean Crawford, Kendra K. Maaß, Katerina E. Aifantis and Graeme Whyte, "Optomechanical measurement of the role of lamins in whole cell deformability", In: *J. Biophotonics* 10.12 (2017), pp. 1657-1664. DOI: 10.1002/jbio.201600198.

Scientific Curriculum Vitae

Julia Kraxner, born 23rd of September 1992 in Fürth, Germany.

- **2017-2021** PhD in Physics, at the Insitiute for X-Ray Physics, within the Göttingen Graduate School for Neurosciences, Biophysics, and Molecular Biosciences (GGNB) of the Georg-August-University School of Science (GAUSS), Göttingen, Germany.

- **2014-2017** M. Sc. in Integrated Life Sciences, Friedrich-Alexander University Erlangen-Nürnberg
  Thesis: "Functional characterization of three-dimensional cardiac microtissues generated by assisted self-assembly", supervised by Prof. Ben Fabry, at the Biophysics Group, Erlangen, Germany.

- **2015** Erasmus+ studies in Photonics, University of Eastern Finland, Joensuu, Finland.

- **2011-2014** B. Sc. in Integrated Life Sciences, Friedrich-Alexander University Erlangen-Nürnberg
  Thesis: "Investigating the Role of Lamin A/C on Cell Mechanics Using the Optical Stretcher", Supervised by Dr. Graeme Whyte, at the Biophysics Group, Erlangen, Germany.

- **2003-2011** Christoph-Jacob-Treu-Gymnasium, Lauf, Germany.